5-2016

Development of Novel Analytical Methods with the Aim of Forensic Analyte Detection using Ultra-Thin Layer Chromatography, Surface Enhanced Raman Spectroscopy, and Magneto-Elastic Wire Sensing

Nichole Ann Crane
University of Tennessee- Knoxville, ncrane@vols.utk.edu

To the Graduate Council:

I am submitting herewith a dissertation written by Nichole Ann Crane entitled "Development of Novel Analytical Methods with the Aim of Forensic Analyte Detection using Ultra-Thin Layer Chromatography, Surface Enhanced Raman Spectroscopy, and Magneto-Elastic Wire Sensing." I have examined the final electronic copy of this dissertation for form and content and recommend that it be accepted in partial fulfillment of the requirements for the degree of Doctor of Philosophy, with a major in Chemistry.

Michael J. Sepaniak, Major Professor

We have read this dissertation and recommend its acceptance:

Bhavya Sharma, Jimmy W. Mays, Dawnie W. Steadman

Accepted for the Council:
Dixie L. Thompson

Vice Provost and Dean of the Graduate School

(Original signatures are on file with official student records.)

Development of Novel Analytical Methods with the Aim of Forensic Analyte Detection using Ultra-Thin Layer Chromatography, Surface Enhanced Raman Spectroscopy, and Magneto-Elastic Wire Sensing

A Dissertation Presented for the
Doctor of Philosophy
Degree
The University of Tennessee, Knoxville

Nichole Ann Crane
May 2016

Dedication

To my Mother who has worked just as hard as I have to realize my potential. Your unconditional love, unparalleled selflessness, and undying support, built my wings feather by feather, so now I fly.

Acknowledgements

First and foremost, I would like to acknowledge God's role in the completion of this dissertation. Just when I thought I simply could not keep going God would light a path. Thank you for your continual guidance and giving me a glimmer of hope whenever I needed it.

I would like to acknowledge my advisor, Dr. Michael Sepaniak, for selecting me to be in his research group. Dr. Sepaniak, thank you for always having my best interest at heart and providing invaluable advice. You know exactly how to tell someone they made a poor research decision in the nicest way possible. Your vast knowledge never ceases to amaze me and I strive to be half of the scientist you are one day.

Next I would like to thank the Center for Nanophase Material Sciences, Oak Ridge National Laboratories for allowing the Sepaniak research group to use their facility. The research team I collaborated with at CNMS was a brilliant group of scientists and engineers. Specifically, I would like to thank Dr. Nickolay Lavrik for your assistance with my pillar array based projects. Your assistance and mentoring were much appreciated.

Additional acknowledgement is made to Dr. Vincent Lamberti and David Mee for their collaboration with the University of Tennessee on the ChIMES project. I remember first working on this project at Y-12 National Security Complex and being told I may not be able to ever publish due to the nature of the project. Four long years later we obtained two patents, won a R&D Magazine Top 100 Award, and have a manuscript in submission. Dr. Lamberti, I thank you for all the opportunities this project gave me. I learned so much working with an incredible team. David Mee, thank you for your persistence in teaching Nahla and I about electrical engineering. I feel like a well-versed scientist due to my participation in this project.

Thank you to my committee members, Dr. Bhavya Sharma, Dr. Jimmy Mays, and Dr. Dawnie Steadman. I appreciate you taking the time to evaluate me as a scientist, as well asthe feedback I have received. Your dedication to my degree has made me a stronger scientist.

I want to acknowledge the Sepaniak Group: Danielle, Ryan, Rachel, Jennifer, Tess, Nahla, Hector, Raymond, and Jim. All of you have been extremely helpful in lifting me

up when things weren't going my way and were the first to share in my successes. Thank you for all the knowledge you all have bestowed upon me.

I would like to acknowledge some family members that helped me become the person I am today. Grandpa Carl you were never a blood relative but you took me in as your own. From the age of two you have been a constant support, both emotionally and financially, as well as the best role model and father figure I could have ever wished for. It gives me great joy to make you proud. You even bought my first laptop, which started me down this journey. Uncle Craig, you were also a positive male role model. Thank you for all the math tutoring lessons. I feel very strong in math because of all the high school tutoring I received from you. I also learned how to be careful with money because of you. Thank you being there for me in school and all other aspects of life. Grandma Paulette Crane, I will always remember you singing "over the rainbow" to me as a toddler when I was sad. You have loved and supported me even through your difficult illness. Thank you for all the financial help with dance and college. I hope to make enough money to help give you the type of care you need and deserve. I love you. Lastly, thank you Grandpa Fred for all the Spanish lessons and attempting to teach me proper grammar. You were a blessing to me and my family. God has now accepted you as one of his angels. Rest in peace.

To my mother, Monica Crane, you were my mother, sister, brother, father, and best friend all in one package. All I ever needed was you to love me and you provided the strongest love imaginable. You never stopped believing in me even though I constantly doubted myself. Thank you for devoting your life to making sure I had a better one. From all the dance competitions to helping me get into college. You have done it all. I will have you live close to me soon enough. The next chapter of both of our lives starts now. I love you more than I could ever describe.

Abstract

The purpose of this dissertation is to develop analytical methods that aid in the detection of forensic analytes. Forensic analytes require methods with increased sensitivity and low limit of detection capabilities. Improvements in separation techniques, surface enhanced Raman spectroscopic techniques, and wire-less gas sensing can each assist in the detection of trace evidence.

When surface enhanced Raman is coupled with thin-layer chromatography a mixture of compounds can be separated and transferred to a metal substrate to be detected using Raman spectroscopy. Surface enhanced Raman scattering enhances the Raman signal intensity by placing a metal substrate in close proximity to an analyte. The new method gives a chemically specific intensified signal along with a chromatographic separation. A traditional separation is performed on a TLC plate, allowed to dry, wetted with a solvent, placed in contact with a metal substrate, and detected using Raman. More efficient chromatographic platforms can be implemented with this method.

New efficient chromatographic platforms are also beneficial to the detection of forensic analytes. Recently, photolithographically nanofabricated open system pillar arrays have proved to be more efficient separation platforms when compared to traditional TLC. These platforms are a form of ultra-thin layer chromatography. This dissertation describes the effects of manipulation on the inter-pillar gap distances with respect to band dispersion. The studies herein manipulate the pillar arrays in order to optimize the separation platform.

The third method developed involved gas sensing of volatile organic compounds. An amorphous ferromagnetic micro-wire was coated with a polymer, where the polymer swelled in response to the gas introduced. When the gas caused the polymer to swell a differential stress response was applied on the micro-wire. The fabricated sensor was tested on simple organic gases but has capabilities to detect low concentrations of low vapor pressure forensic analytes.

All three projects were significant advancements in analytical method development. The analytes used were either fluorescent dyes or volatile organic compounds to test feasibility of each method. More efficient chromatographic platforms were fabricated,

surface enhanced Raman was coupled to TLC, and a micro-wire gas sensor was calibrated for the studies performed in this dissertation.

Table of Contents

List of Tables

List of Figures

Abbreviations & Symbols

A	Eddy diffusion term
ALD	Atomic Layer Deposition
B	Longitudinal dispersion term
BT	Benzene Thiol
CAD	Computer Assisted Drawing
CCD	Charge Coupled Device
CE	Chemical Enhancements
ChIMES	Chemical Identification by Magneto-Elastic Sensing
C_M	Resistance to mass transfer in the mobile phase
cos θ	Cosine of the contact angle of the mobile phase
C_S	Resistance to mass transfer in the stationary phase
c_{SERS}	Concentration of the surface enhanced Raman signal
c_{RS}	Concentration of the Raman signal
d_{ME}	Thickness of magnetoelastic sensor
dA	Area
d_f	Average film thickness of the stationary phase
D_M	Diffusion coefficient for the mobile phases
d_p	Particle diameter
dp	Particle size
DPA	Deterministic Pillar Array
DRIE	Deep Reactive Ion Etching
D_S	Diffusion coefficient for the stationary phase
E	Magnitude of the electromagnetic field around an analyte
E’	Elasticity
E_0	Peak amplitude of electromagnetic field around an analyte
E_L	Electric Field at the molecule position
E_i	Incident electric field
EBL	Electron Beam Lithography
EF	Enhancement Factor
EM	Electromagnetic
EMF	Electromagnetic Field
ΔE_v	Difference in energy for the vibration
F	Force acting on a magnetic pole
Δf	Resonant frequency change
f	Frequency of a sensor
f_0	Initial resonant frequency
GLAD	Glancing Angle Deposition
h	Planck’s Constant
H	Plate Height
H	Magnetic field intensity
$\boldsymbol{H_0}$	Applied magnetic field due to electric current
HOMO	Highest Occupied Molecular Orbital
HPLC	High Performance Liquid Chromatography
HPTLC	High-performance Thin-Layer Chromatography

H_{ss}	Band Dispersion from Spot Solvation
I	Scattered Intensity
I_0	Intensity of incident light
I_{RS}	Intensity of the Raman Signal
I_{SERS}	Intensity of the SERS signal
ICP	Inductively Coupled Plasma
K	Proportionality Constant
k'	Retention Factor
K_0	Permeability Constant
K_C	Fundamental partition coefficient
k_o	Permeability constant
L	Total column/wire length
L^2	Solvent front displacement
LFIEF	Local Field Intensity Enhancement Factor
LOD	Limit of Detection
LUMO	Lowest Unoccupied Molecular Orbital
LSPR	Localized Surface Plasmon Resonance
Δm	Mass loading
m_0	mass of the magnetoelastic sensor
MP	Mobile Phase
MGITC	Malachite Green Isothiocyanate
MXT	Melt Extraction Technology
$M_L(\nu_L)$	Local field intensity enhancement factor at the Raman dipole
$M_{Rad}(\nu_R)$	Radiation enhancement factor at the Raman dipole
η	Viscosity
n	Peak Capacity
n_p	Number of Photons
N	Number of theoretical plates
NC	Nanocomposite
NP	Normal Phase
N_p	Number of Pillars
NTLC	Nano-Thin Layer Chromatography
N_{RS}	Average number of molecules in a Raman measurement
N_{SERS}	Average number of molecules in a SERS measurement
OPLC	Overpressured Layer Chromatography
OTS	Octadecyltricholorsilane
p_1	Magnetic Pole 1
p_2	Magnetic Pole 2
$p^{'}$	Polarity Index
PC	Paper Chromatography
PC’	Principle Component
PCA	Principle Component Analysis
PDMS	Polydimethylsiloxane
PEB	Post Exposure Bake
PECVD	Plasma Enhanced Chemical Vapor Deposition
PSO	Porous Silicon Oxide

r	Distance between magnetic poles
RF	Radio Frequency
R_f	Retardation factor
Rh6G	Rhodamine 6G
RIE	Reactive Ion Etching
RP	Reverse Phase
RSD	Relative Stand Deviation
SEM	Scanning Electron Microscope
SERS	Surface Enhanced Raman Scattering
S_f	Mobile phase solvent front
SP	Stationary Phase
SPA	Stochastic Pillar Array
STT	Sample Translation Technique
t	Time
t_R	Retention Time
TLC	Thin-Layer Chromatography
TRM	Target Response Material
μ_f	Solvent front displacement
μ_R	Raman Dipole
μ_0	Permeability of the vacuum
UTLC	Ultrathin-Layer Chromatography
UV	Ultraviolet
v	Average linear velocity
v_f	Velocity of the solvent front
Vc	Total volume per pillar array
V_p	Pillar Volume
VOC	Volatile Organic Compound
V_S/V_M	Volume ratio of stationary (VS) to mobile phase (VM)
v	Frequency
v_i	Frequency of the incident beam
v_L	Local field induced frequency
v_R	Local field radiated frequency
W_h	Width of the peak
α	Polarizability of the bond
β	Phase volume ratio
θ	Contact angle of the mobile phase
ρ	Density
ρ_l	Density of the surrounding medium
ρ_s	Density of the sensor
σ_{sc}	Scattering cross section
λ	Wavelength of the incident photon
γ'	Surface Tension

Chapter 1

Introduction to Planar Chromatography

1.1 Introduction

Thin-layer chromatography (TLC) is a widely-used and popular separation technique of non-volatile compounds. TLC is very simple to implement, has wide applications with a variety of samples, high sensitivity, is a quick separation process, relatively low cost, and there is wide commercial availability of TLC equipment.[1] This technique can be used to check the purity of a substance, separate and identify the components in a mixture, or obtain a quantitative analysis of the components in a mixture. Compared to most forms of chromatography, the limitations of TLC are poor reproducibility, high detection limits, higher plate heights, and inability to resolve complex mixtures.

In simple thin-layer chromatography a small mixture of analytes is applied at one end of a TLC plate. A TLC plate is normally a sheet of glass, plastic, or aluminum foil that is coated with a thin-layer of adsorbent material, such as silica gel, aluminum oxide, or cellulose. This thin-layer is considered the stationary phase.[2] The sample is allowed to dry. The TLC plate, with analyte spotted, is placed into a closed chamber with a solvent or solvent mixture. The TLC plate is dipped into this solvent (known as the mobile phase) and capillary action causes the solvent to draw up the plate (known as the development process). If the phases are chosen correctly then the components will separate due to different development rates.[3] A typical separation on a TLC plate is depicted in Figure 1.1.

Detection of the components in a mixture is simple when the separated compounds are naturally colored, fluorescent or absorb UV light.[3] Most separated compounds need the aid of a detection reagent that is sprayed or dipped onto the plate to produce a color or create fluorescence. In order to incorporate the detection of a wider variety of compounds, fluorescent indicators can be attached to the stationary phase so compounds that quench fluorescence can be evaluated (i.e. inorganic compounds).

Normally, to identify components in a mixture with TLC a retardation factor R_f is used to compare the known compounds in the mixture. Section 1.11 of this chapter describes R_f values further. If the possible sample components are not known then thin-layer chromatography must be coupled to a chemically specific detection method such as

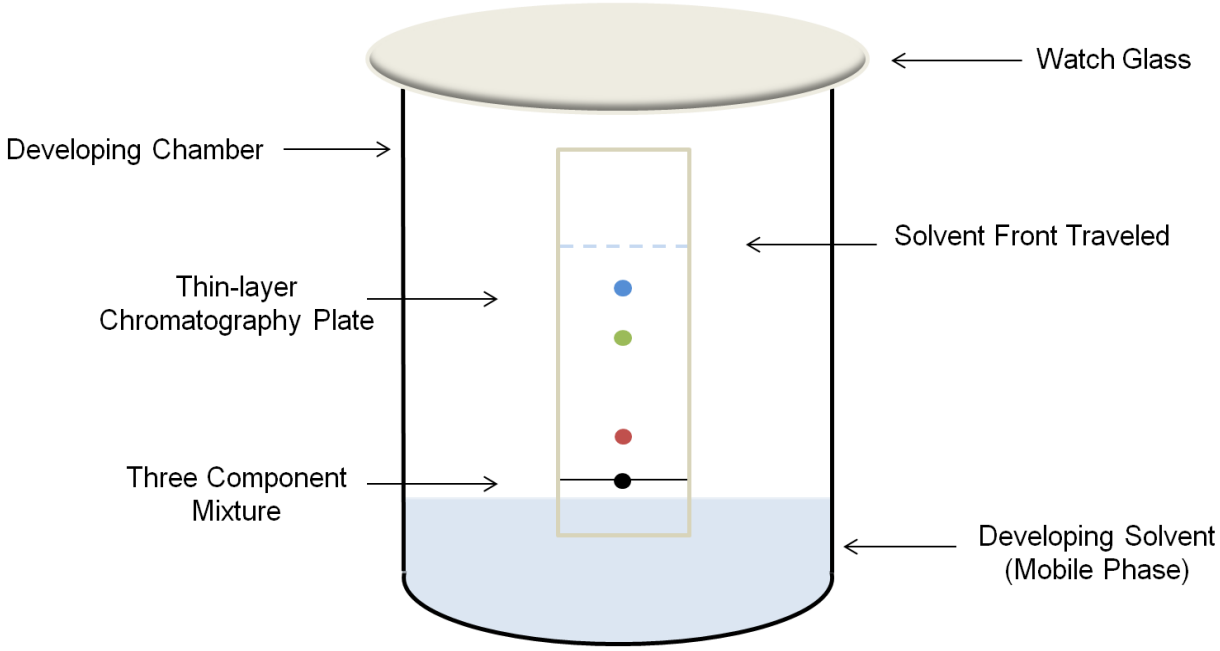

Figure 1.1: Traditional thin-layer chromatography apparatus with a three component mixture.

mass spectroscopy, infrared spectroscopy, Raman spectroscopy, or nuclear magnetic resonance. R_f values are not reproducible from trial to trial and are considered mainly as guides to development order and relative development distances of the separated compounds. In summary, thin-layer chromatography is a useful and inexpensive technique with a wide variety of applications.

1.2 Thin-layer Chromatography Basic Principles

The first reports of liquid chromatography date back to the first description of chromatography by Michael Tswett in the early 1900s, and then reviewed by Sherma. In the 1950s, Kirchner and colleagues at the U.S. Department of Agriculture performed TLC as it is performed today.[3] They used silica gel held on glass plates with the aid of a binder, and the plates were developed with the conventional procedures used in paper chromatography. Martin and Synge won the Nobel prize for their work on liquid-liquid (or partition) chromatography, which became known as plate theory.[4] Rate theory came into existence around the same time as plate theory by van Deemter, Zuiderweg, and Klinkenberg.[5] They described the chromatographic process in packed gas chromatography (GC) columns in terms of kinetics, mass transfer, and diffusion properties.

There are two phases in chromatography, a mobile phase (the developing solvent) and a stationary phase (SP) (immobile phase that adheres to the plate). Ideally, when the mobile phase passes through the stationary phase, the components of the mixture equilibrate between the two phases allowing different development rates throughout the separation.[2] The efficiency of TLC is restricted by the variable velocity of the mobile phase, which is driven by capillary forces. In capillary flow TLC, the velocity of the mobile phase through the layer is controlled by capillary and retardation forces and decreases as development distances increases.[3] Obtaining less than the optimal velocity could lead to zone broadening (band diffusion) that is largely influenced by molecular diffusion. Guiochon et al. demonstrated in their work that the packing and the slow mass transfer processes can contribute to broadened irregularly shaped zones with large particle sorbent layers.[6]

In planar chromatography, a gas phase is present in addition to the stationary and mobile phases. The separation is still driven by capillary action, and the developing solvent moves up the layer until the desired solvent front distance is reached. The plate is then removed from the mobile phase to interrupt the chromatography process. Phase equilibrium is ideally reached between the components of the developing solvent and the vapor phase, although that may not be realized in practice.[3] The interaction involved in determining chromatographic retention and selectivity includes hydrogen bonding, electron-pair donor/electron-pair acceptor, ion-ion, ion-dipole, and van der Waals interactions.

1.3 Advancements of Planar Chromatography

In laboratories worldwide, thin-layer chromatography will continue to be a general low-cost and low-technology qualitative and screening method. TLC will continue to evolve into separation platforms that are highly selective, sensitive, quantitative, rapid and have automated capabilities for analysis.[3] Advancements in the field are necessary to quickly analyze a large quantity of samples, incorporate multi-dimensional separations, and obtain more efficient separations. The development of high-performance thin-layer chromatography (HPTLC) and ultra-thin layer chromatography (UTLC) are important advancements in the field of TLC.

High-performance thin-layer chromatography contains smaller sorbent layers, slightly smaller and uniform particle sizes, and is developed for a shorter distance than traditional TLC. The advantages of HPTLC are faster separations, reduced band diffusion, enhanced separation efficiency, lower detection limits, and the ability to analyze more samples per plate. This form of chromatography can easily be automated, which allows for better control of the separation.

HPTLC is implemented with the same simple design as TLC but has capabilities to be performed under pressure to help correct for the small development distances. In the pressurized form of HPTLC, the development occurs under pressure with sequential samples analyzed in a closed on-line system and detection of the separated analytes is commonly achieved through ultra-violet (UV) absorption.[3] Having a HPTLC separation

performed under pressure gives the analytes the ability to fully resolve and to develop longer giving higher efficiency values for the separated bands.

Another innovation of planar chromatography is ultra-thin layer chromatography (UTLC). Miniaturization is of utmost importance in many analytical techniques. Creating miniaturized techniques and equipment allows for devices to become portable to on-site testing. In 2001, Hacuk et al. discovered a new pre-coated silica gel layer that was given the name ultra-thin layer chromatography.[7] The layer thickness of UTLC plates are only 10-20 µm, whereas the usual layer thickness in traditional TLC plates are 250 µm. The ultra-thin layer consists of a monolithic structure, which does not require any form of binder. The monolithic silica gel layer consists of well-defined meso- and macropores. Ultra-thin layer chromatography exhibits lower detection limits, shorter development times, and less solvent consumption. The original UTLC plates had inherent disadvantages such as lower retention values (k') due to loss of surface area, lower resolution and high plate heights due to the short separation distances. Retention value and plate height definitions/equations can be found in sections 1.9 and 1.10.

To overcome the pitfalls of UTLC, various research groups have fabricated new ultra-thin layer separation platforms. Saha et al. used microfluidic channels with integrated pillars that were fabricated using SU8 and polydimethylsiloxane (PDMS) substrates to study capillary flow.[8] The findings for the study were that the pillar size (diameter, pitch and height) and the physical properties of the fluid (surface tension and viscosity) are found to have significant influence on the capillary action. Olesik and Clark developed electrospun glassy carbon nanofibers as UTLC platforms, where SU8 photoresist was used. The electrospun glassy carbon plates developed exhibited tunable retention, high plate number and physical and chemical robustness for a variety of mobile phases.[9-10] Glancing angle deposition was used by Brett et al. in order to create high surface area columnar microstructures with aligned macro-pores for stationary phases in analytical chromatography.[11-12]

Desmet and Regnier inspired the studies done in this dissertation with their work in micromachining enclosed pillar arrays and fluid dynamics.[13-28] Desmet's research

focuses on the miniaturization of separation methods and on the investigation and the modelling of flow effects in chromatographic systems. Other work has been related to understanding of the relation between the packing structure and the performance of HPLC supports to suggest rules to optimize their shape and the external porosity. Regnier et al. fabricated pillar arrays within channels in a reproducible and controlled manner. The Regnier group has also studied geometric effects of pillar arrays on efficiency in separations. Tallarek and co-workers study the morphology-transport relationships for chromatographic media (packed and monolithic beds, confined pillar structures). Their work is the systematic study of how individual parameters, such as the particle size distribution, particle porosity, the bed porosity, and the confinement, affect the morphology of computer-generated packed beds.

The pillar array platforms described in this dissertation were reformed from the enclosed pillar array separations previously studied by the Sepaniak group.[29] However, the enclosed pillar array field crowded and because of the inherent problems the group moved to use pillar arrays as open UTLC platforms as first seen by Kirchner et al.[30] The Sepaniak group used pillar array separation platforms to create a perfectly uniform ultra-thin layer platform. The pillar array platform was the first use of pillar arrays in an open system. Kirchner describes the increase in velocity and efficiency in comparison with thin-layer chromatography. The study describes that the increase in efficiency is due to the perfectly ordered arrays and rapid flow, which leads to rapid phase exchange that occurs between the stationary and mobile phases. Other advantages of pillar arrays have been explored by the Sepaniak group where findings indicated increased surface-enhanced fluorescence occurs from nanopillar systems where there are applications with beryllium and bioaffinity samples.[31-33] Part of the research described in this document manipulates inter-pillar gaps of pillar array platforms in order to determine if smaller gaps further increase efficiency, which is described in Chapter 6.

1.4 Stationary Phases for Planar Chromatography

Stationary and mobile phases must be carefully selected in order to create a successful separation of analytes. Stationary phases can be either a liquid or a solid.

Liquid SPs can be coated directly on an inert solid support or on the inside of a column. Silica gel is the most frequently used stationary phase where separations take place primarily by hydrogen bonding or dipole interaction with surface silanol groups causing analytes to separate according to their polarity. Other adsorbent TLC stationary phases include aluminum oxide, magnesium oxide, magnesium silicate, polyamide, and kieselguhr.[3] For example, a researcher may use aluminum oxide instead of the traditional silica gel in order to separate aromatic hydrocarbons or their derivatives.

Some compounds that have the same polarity and functional group can migrate together on silica gel plates. Crystalline cellulose can be used for normal phase (NP) liquid-liquid partition TLC to separate compounds such as amino acids or water-soluble biopolymers.[3] Normal phase TLC refers to the stationary phase being polar so that the polar analytes move slowly while the nonpolar analytes develop closer to the solvent front. Other stationary layers have been impregnated with buffers, chelating agents, metal ions, or other compounds to aid in the resolution or detection of certain compounds. Depending on the specific application at hand determines which type of stationary phase is most appropriate.

The plates developed for HPTLC contain narrow pore and particle size distributions. The layer thickness of HPTLC stationary phases are approximately 100-200 µm whereas traditional TLC layer thicknesses are approximately 250 µm. Ultra-thin layer chromatography utilizes 10-20 µm layers. High-performance stationary phases contain less band diffusion, better resolution, smaller analyte consumption (0.2-1 µL of sample spotted), sensitive detection, and are more efficient. Flow resistance is higher with the thinner stationary phases but the overall development time is shorter.[3] The lower flow rate of fine-particles has led to forced-flow HPTLC.

In reversed-phase TLC, described in more detail in section 1.6, the stationary phase has a bonded layer created to be less polar than the mobile phase. The most common bonded phases are CH_3, C_2H_5, C_8H_{17}, and $C_{18}H_{37}$ functional groups. The larger the chain length of the bonded phase the more hydrophobic the separation media becomes. High proportions of water in the mobile phase cause a lack of development of analytes

up the stationary phase but can be solved by adding 3% NaCl to the mobile phase.[3] Part of the work performed in this dissertation uses a silicon oxide fabricated pillars with a carbon bonded phase in order to perform reverse phase separations.

1.5 Selection of the Mobile Phase

The most critical parameter in achieving a separation with high selectivity is the choice of a stationary and mobile phase. Mobile phases in TLC are selected based on the chemical properties of the stationary phase and mixture of analytes required for separation. The polarity of the mobile phase influences the retention factor range of analytes, while the chemical properties of the solvent components determine the selectivity and interactions of the system.[3] Solvents or solvent mixtures are classified according to elution strength compared to a particular stationary phase or bonded layer on a stationary phase. When polarity increases, a solvent in NP-TLC becomes stronger, whereas in RP-TLC less polar solvents are considered strong. Due to the many possible interactions with mobile and stationary phases, the mobile phase is most often selected by reviewing the literature of similar separations or by trial and error. Mobile phase selection and optimization have been subject to systematic and computer-assisted approaches based on solvent strength and selectivity parameters. Though this method is less popular than a literature search the most popular computer-assisted program is PRISMA.[34-35]

Mobile phase selection occurs depending on the type of chromatographic platform used. For normal phase TLC some mobile phase solvents include: hexane, toluene, chloroform, acetone, ethyl acetate, etc. Silica gel TLC uses chloroform, methyl tert-butyl ether, and diethyl ether as the most commonly used MP solvents to enhance resolution.[3] Solvent strength is normally controlled by the amount of hexane used when solvent mixtures are used. In reverse phase TLC the R_f (i.e. analyte solvent front distances) values for a series of solutes are normally reversed compared to the NP-TLC silica gel if water is a large percentage of the mobile phase. Well resolved separations can occur on RP plates of entirely organic mixtures for the mobile phase. Two-solvent mixtures of water and an organic modifier are commonly used in reversed phase TLC.

In ion exchange chromatography, the mobile phases are usually aqueous solutions with a specific pH and ionic strength.

1.6 Normal and Reverse Phase Chromatographic Platforms

Normal and reverse phase TLC separation platforms describe the interaction between the stationary and mobile phases. Normal phase chromatography is where the stationary phase is polar and the mobile phase is nonpolar. The least polar compounds elute first and the most polar elute last. Common mobile phases for NP-TLC consist of a nonpolar solvent (i.e. hexane) with a slight more polar solvent (i.e. isopropanol). Retention of the analytes increases as the amount of nonpolar solvent in the mobile phase increases. Normal phase is said to follow an adsorptive mechanism, where the separation is based mainly on differences between adsorption affinities of the analytes to the surface of an active solid.

Reverse phase (RP) chromatography is where the stationary phase is nonpolar and the mobile phase is polar. In RP chromatography, the most polar compounds elute first with the most nonpolar compounds eluting last. The mobile phase is typically a mixture of water and a polar organic solvent (i.e methanol). In the reversed phase case, retention increases as the amount of polar solvent in the mobile phase increases. Reversed phase chromatography is described as a partition mechanism, where the separation is based on differences between the solubilities of the analytes in the stationary phase, or the differences between the solubilities of the analytes in the mobile and stationary phases.

1.7 Development Chambers

Planar chromatography development chambers can be seen in a variety of formats including horizontal and vertical set-ups. Figure 1.2 shows the variety of planar chromatography development chambers. Figure 1.2a demonstrates a descending development that is used for paper chromatography. The traditional ascending development chamber where the mobile phase is located at the bottom of the chamber and travels up the plate via capillary action can be seen in Figure 1.1 and is the

chamber configuration used for the studies in this dissertation. Figure 1.2b is used in TLC and is referred to as the sandwich chamber set up. Figure 1.2c is a horizontal chamber configuration where a circular sheet of filter paper is placed over a petri dish with a wick cut out of it for solvent transfer. Kirchner et al. worked with open pillar array systems in a horizontal development chamber that was amendable to real-time detection.[30, 36] Kirchner machined the development chamber and was able to view the separation under the fluorescence microscope as the mobile phase passed through the stationary phase. That horizontal development chamber is shown in Figure 1.3. Each development performed in this dissertation is considered to be a linear development.

1.8 Techniques in Thin-Layer Chromatography

Following a set of techniques in thin-layer chromatography will help optimize the separation process to obtain an increase in efficiency. The first step in the separation process is spotting on the separation platform after the samples have been prepared. When spotting the sample onto the plate, the spot should occupy as small of an area as possible on the bed. Micropipets and microsyringes are the best tools when applying spots to the chromatographic beds. The application of the sample should not disturb the bed, therefore, the sampling device should not touch the surface of the bed. The spotted sample should be dry before the development occurs. The spot should be strategically placed so that the analyte spot does not dip into the solvent reservoir once development is commenced. In my work, the separation platform (silicon dioxide pillar arrays) is superhydrophobic facilitating very small initial spot sizes. The spot sizes range from 100 to 200 µm.

The next step in the process is inserting the plate with the sample into the development chamber. The chamber should be pre-saturated with the mobile phase vapors. Once the chromatographic plate is inserted, it is crucial to allow the chamber to re-equilibrate with either a saturation pad soaked in the mobile phase liquid or simply a small volume of mobile phase liquid at the bottom of the chamber. Depending on the size of the chamber and the volatility of the mobile phase solvent or solvent mixture, the equilibrium time can be ~5-30 minutes. The mobile phase vapors need to saturate the

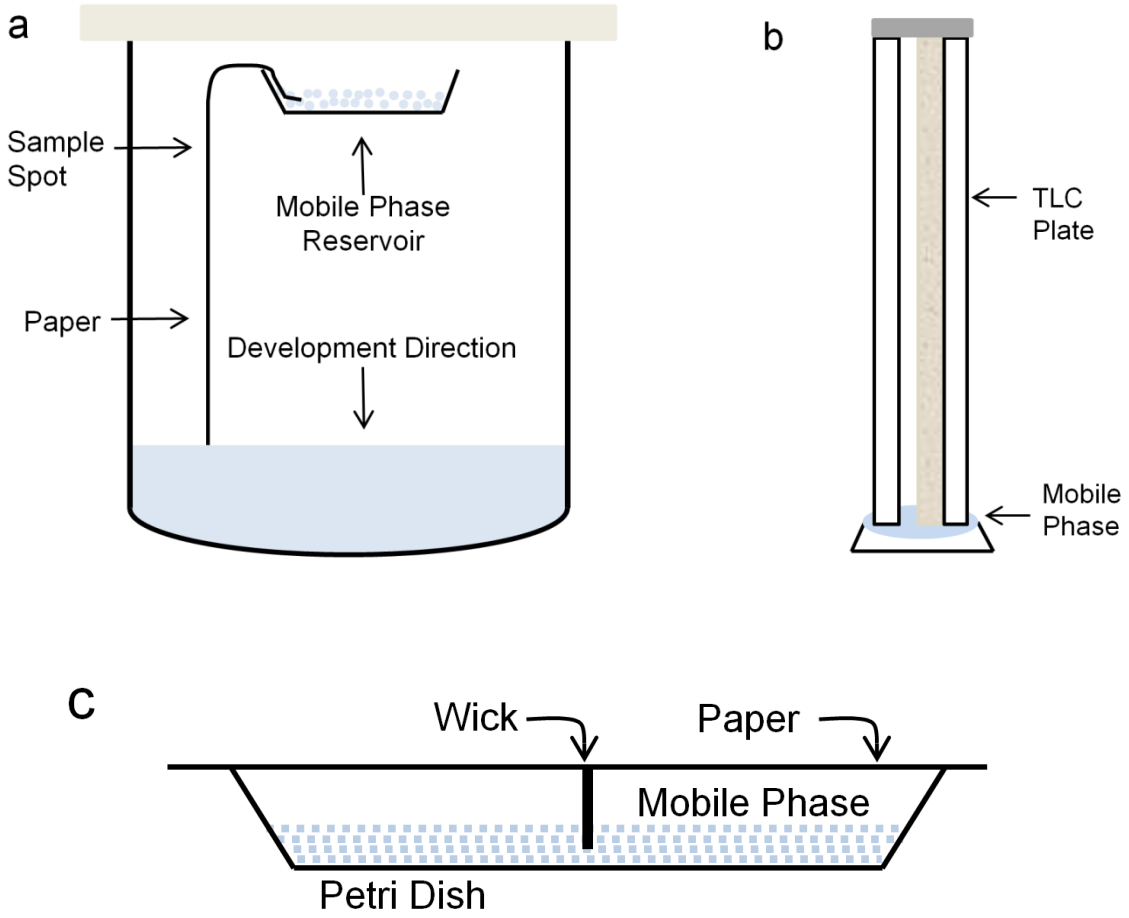

Figure 1.2: Other development chambers for planar chromatography. a) Descending development chamber (paper chromatography), b) Sandwich chamber (TLC), c) Horizontal chamber (paper & HPTLC).

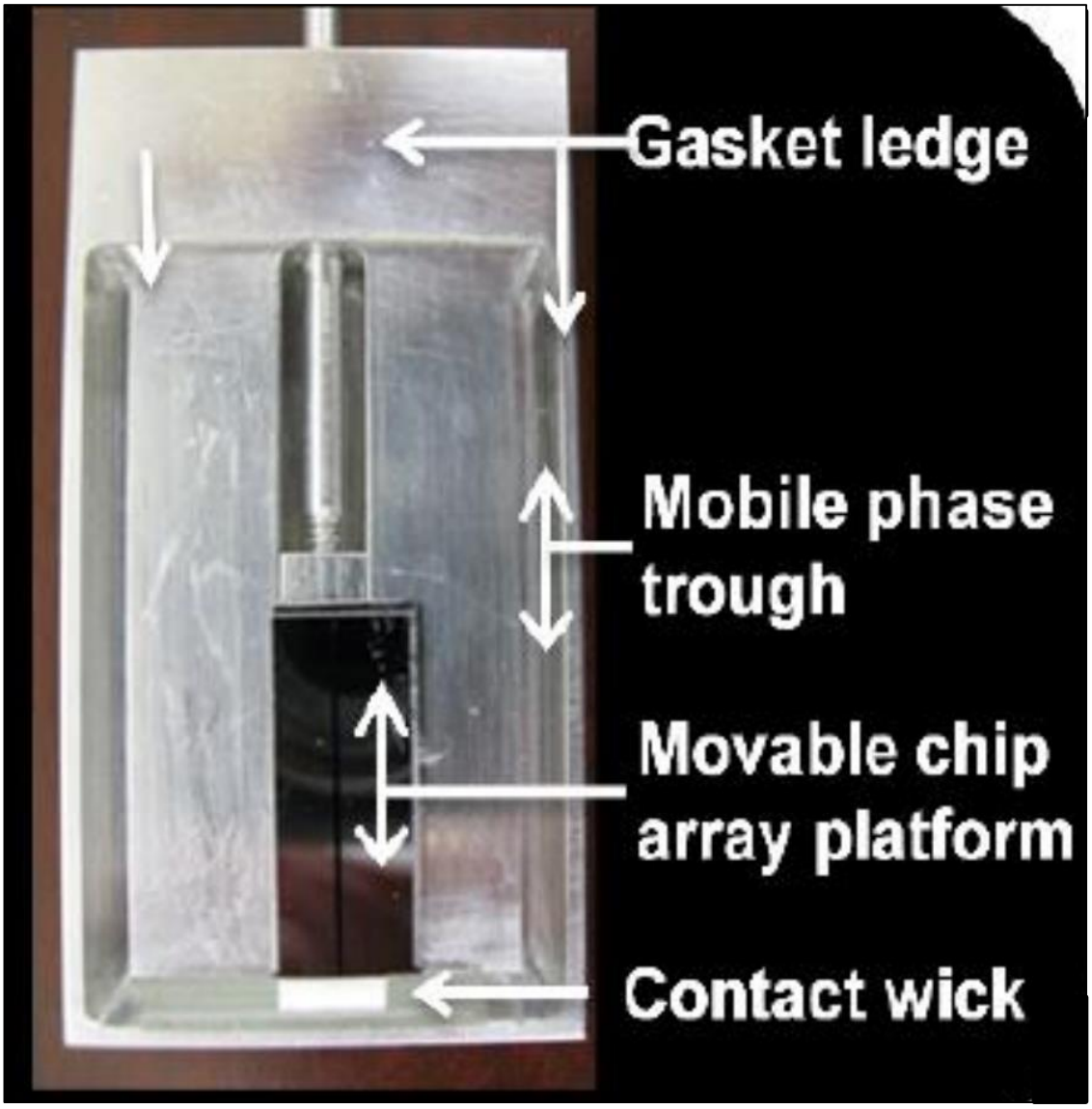

Figure 1.3: Horizontal development chamber machined for real time fluorescence detection of separating compounds. Reproduced with permission from: Kirchner, T. B. The fabrication of micro- and nano- scale deterministic and stochastic pillar arrays for planar separations. University of Tennessee, Knoxville, TN, 2015.

chromatographic plate as well as be in equilibrium in the chamber. Evaporation and condensation processes occur continuously within the chamber. Mobile-phase gradients form in normal phase TLC due to more polar components being sorbed preferentially by the hydrophilic layer, which causes solvent de-mixing (remaining solvent to be depleted in this solvent). The gradients formed are not easily controlled and are detrimental to the reproducibility of analyses. Development times, separations, reproducibilites, and retardation values can vary greatly if equilibrium is not reached, solvent de-mixing occurs, the temperature changes, or if the humidity changes.[3] As a last note, the plate should be dipped in the mobile phase solvent the same distance up the plate each run to ensure reproducibility in development distances.

After the development is complete, it is important to disrupt the bed as little as possible. For certain chromatographic platforms, the platform needs to be dried after a separation occurs. Due to the nature of the chamber being saturated in the mobile phase liquid, the bed is unlikely to dry inside the chamber without exposing to some air or flow of air. If any flow of air is introduced to the bed to assist in the drying process, it must be at a low flow rate and allow the plate to dry equally across the plate.

1.9 Original Van Deemter Theory

To understand band broadening and kinetics of chromatographic systems van Deemter and co-workers developed an equation discussing four major sources of band broadening in relation to velocity.[5] In the equation seen below, the A term is eddy diffusion, the B term is longitudinal molecular diffusion, the C_s term is resistance to mass transfer in the stationary phase, and the C_M term is the resistance to mass transfer in the mobile phase. Plate height (H) describes the total broadening contributions of all three terms as a function of average linear velocity (ν). The van Deemter equation in simple terms is:

$$H = A + \frac{B}{\nu} + (C_s + C_M)\nu \qquad [1.1]$$

In this equation, the A, B, and C terms need to be minimized in order to maximize column efficiency.

Each of the band broadening terms has specific equations to describe the nature of their dispersive effects. The eddy diffusion term (or multipath effect) describes the random path that an analyte travels through a heterogeneous packed column. To minimize the A term small, uniform particles should be used and they should be tightly packed. Molecular diffusion describes how a zone of molecules diffuses from a region of high concentration to a region of low concentration with time. Zone broadening occurs as the analyte proceeds through the column. The B term is divided by average linear velocity indicating that a large velocity or flow rate will minimize the molecular diffusion. The C term is concerned with how fast solute sorption and desorption occurs in order to keep the molecules close together and the band broadening to a minimum. To minimize this term the film thickness should be small and diffusion coefficient large. The expanded van Deemter equation is as follows:

$$H = 2\lambda d_p + \frac{2\gamma D_M}{v} + \frac{q k' d_f^2 v}{(1+k')^2 D_s} + \frac{\omega {d_p}^2 v}{D_M} \qquad [1.2]$$

Each term defined:

d_{p} = particle diameter

k' = partition coefficient

d_{f} = average film thickness of the stationary phase

D_{s} and D_{M} = diffusion coefficient for the stationary and mobile phases, respectively.

q, λ, γ and w are independent factors that are conditional to the packing or ordering of the column.

Traditional van Deemter plots are depictions of efficiency where H vs. v is graphed. The minimum in the curve is the optimum velocity, which provides the highest efficiency (smallest plate height). Figure 1.4 shows a typical van Deemter curve and the band broadening contributions separately. There is a trade-off between running a chromatographic separation at the optimum velocity and increasing the velocity to decrease analysis time.

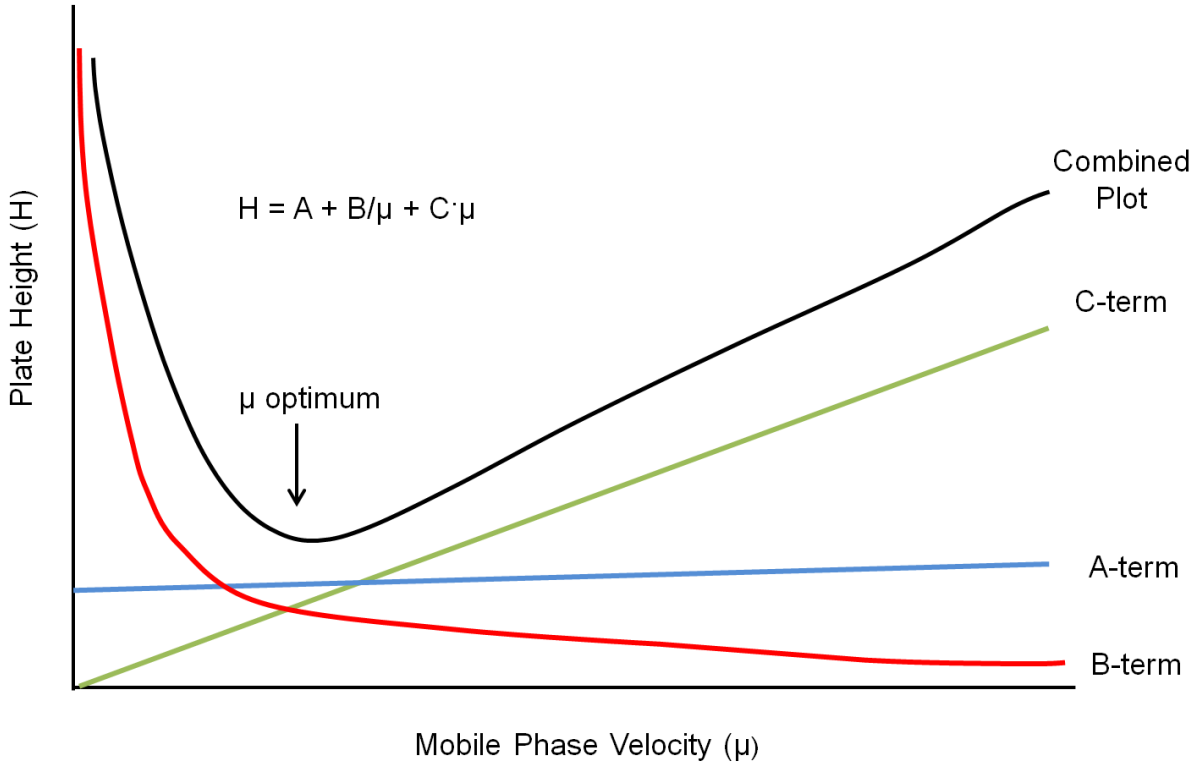

Figure 1.4: Typical van Deemter curve to measure efficiency of a chromatographic platform. The combined plot (black line) is the combination of the A, B, and C terms from the van Deemter equation referred to as the van Deemter curve.

As discussed with the van Deemter plots, it is important to note the average linear velocity term. The velocity in the equation can be increased to diminish the B term but in effect increases the C term. In order to predict relative velocity trends among different solvents the equation below is used:

$$\mu_f^2 = K_0 t d_p \left(\frac{\gamma'}{\eta}\right) \cos\theta \qquad [1.3]$$

μ_f^2 = solvent front displacement

K_0 = permeability constant

d_p = particle diameter

t = time

γ'/η = surface tension to viscosity ratio of the mobile phase

$cos\theta$ = cosine of the contact angle of the mobile phase

From the rate theory described by van Deemter, it is apparent that the band broadening terms along with average linear velocity are important to manipulate in order to increase efficiency. Part of the work described herein uses traditional van Deemter equations to evaluate a more efficient separation platform. Kirchner et al. used photolithography to create pillar array chemical separations in an open system and witnessed an increase velocity and an increase in efficiency when compared to traditional TLC plates.[30] Additionally, pillar arrays are uniform in structure (diminishing the eddy diffusion term) and are only ~20 µm tall (creating a UTLC platform). Other benefits are described in Chapter 6.

1.10 Mobile Phase Flow for Traditional Planar Chromatography

The nature of mobile-phase flow in capillary driven systems is highly dependent on the γ'/η ratio.[2] The existing model assumes the chromatographic platform to be comprised of interconnected capillaries of varying diameter. Solvents that maximize the γ'/η ratio are preferred for TLC.[37] For silica gel layers (NP), the contact angle for all

common solvents is close to zero as all solvents wet it adequately. For reversed-phase SPs the contact angle of the solvent increases rapidly with increasing water content of the mobile phase. Solvents with a high viscosity and surface tension will experience a slower development rate than that with low viscosity and surface tension. To minimize the variation in capillary flow a homogeneous chromatographic platform is preferred. Even in a perfectly ordered system, the quantity of mobile phase varies across the bed.

The mobile-phase solvent front s_f is defined as the square root of the proportionality constant k multiplied by the development time t, which is a manipulation of equation 1.3:

$$s_f = \sqrt{kt} \qquad [1.4]$$

In equation 1.4 the proportionality constant is proportional to surface tension and inversely proportional to the viscosity as seen below:

$$k = \frac{2K_0 d_p \gamma'}{\eta \cos\theta} \qquad [1.5]$$

Where the terms have been defined above:

Equation 1.5 shows that capillary flow is strongly influenced by particle size, the permeability constant (factors that define the chromatographic platform), and the surface tension to viscosity ratio of the mobile phase.

The velocity of the solvent front v_f then becomes:

$$v_f = \frac{k}{2s_f} \qquad [1.6]$$

This equation shows that the solvent velocity decreases the further the solvent has migrated.[2] In traditional TLC the velocity eventually goes to zero, which puts a limit on the mobile phase development distance. The rate of the mobile phase is determined by the choice of solvent and the nature of the bed since the flow is not constant or easily controlled.

Another inherent issue with capillary flow TLC includes the evaporation of the solvent migrating through the separation platform. The temperature of the solvent chamber is not regulated, which causes potential evaporation related artifacts. For example, if the mobile phase solvent is comprised of two or more liquids then the evaporation of the most volatile liquid will cause a change in solvent composition. Due to these inconsistencies in evaporation rates of the mobile phase, evaluation of a phase ratio is pertinent to this discussion. The relationship between retention factor and phase ratio is defined below:

$$k' = K_c \frac{V_s}{V_m} \; or \; \frac{K_c}{\beta} \qquad [1.7]$$

The terms are defined as:

k′ = retention factor, the measure of the time a compound resides in the stationary phase relative to the time it resides in the mobile phase.

K_c = fundamental partition coefficient, molar concentration of the analyte in the stationary phase to that in the mobile phase

V_S/V_M = the volume ratio of stationary (V_S) to mobile phase (V_M)

β = the phase volume ratio (V_M/V_S)

Observing equation (1.7), as the phase ratio increases the retention factor gets smaller. If the phase ratio increases, the mobile phase velocity V_{mp} for the zone experienced by the band increases. Ideally, the retention factor for an analyte is between 1 and 5 and constant during a separation.[37]

1.11 Planar Chromatography Evaluation Metrics

In order to analyze the performance of separations, common chromatographic equations are used. Besides the use of the van Deemter equation to evaluate the broadening of a chromatographic spot, plate number and theoretical plate height can be determined.

$$N = 5.54\left(\frac{t_R}{w_h}\right)^2 \quad [1.8]$$

$$H = \frac{L}{N} \quad [1.9]$$

Equation 1.8 describes plate number where t_R is the distance that the band has traveled from the original spot and, w_h, is the width of the peak. For equation 1.9, H is the plate height, L is the total column length, and N is the plate number calculated from 1.8. To receive a more efficient separation platform, a small H value and a large N value is required. Most research in the area of separations continues to focus on reducing H and maximizing N values.

Another important evaluation metric is retardation factor R_f. Retardation factor is used to express the position of solute on the developed chromatogram. The basic ratio is as follows:

$$R_f = \frac{distance\ of\ the\ chromatographic\ spot\ center\ from\ start}{distance\ of\ solvent\ from\ start} \quad [1.10]$$

Or the retardation equation with variables is commonly seen as:

$$R_f = \frac{1}{1+k'} \quad [1.11]$$

Equation 1.11 represents the relationship between retention factor (k') and retardation factor. All retardation factors are less than one. If an analyte spot is a value of 1 then then the spot developed with the solvent front. If the analyte spot is closer to the value of zero then the spot developed only a short distance.

The main goal of a chromatographic separation is to separate analytes without any overlap of bands. The evaluation metric to assess the degree of separation of analytes is called resolution (R_s). Resolution can be calculated using the following equation:

$$R_s = \frac{2d}{w_A+w_B} \quad [1.12]$$

Where d is the distance of peak maxima or distance between the centers of two separated analytes. The w_A and w_B are the widths of the bands at the base or the total width of the analyte spot.

The last measure of column efficiency considered is the peak capacity (n) which is defined as the number of peaks that can be resolved by a given chromatographic separation platform in a given time. Guiochon developed an equation that is widely accepted for TLC using the plate number (n):[6]

$$n = 1 + \frac{\sqrt{N}}{2} \qquad [1.13]$$

Because TLC has a limited development distance n values are relatively low (≤10), but can be increased if a second dimension is added.

1.12 Detection Methods

The most common detection methods for TLC are absorbance or fluorescence spectrometry. Some other detection methods are based on the difference in solubility, iodine vaporization, the addition of pH indicators, or the detection of radioactively labeled substances.[3] For detection methods performed in this dissertation, the process is performed on a dry plate after development.

In most cases, detection is non-destructive. For colored substances, the human eye is the detector. Some colorless substances can be excited to produce fluorescence or phosphorescence by longwave UV radiation. There are compounds that are colorless and non-luminescent, which can be visualized under a UV lamp (254 nm) by using TLC plates with a fluorescent indicator.

Other detection methods include photometric detection techniques. For transmission spectroscopy, densiotometry of TLC plates was originally used in the 1960s but is not a popular form of detection due to the inability to detect beyond 325 nm. Most transmission measurements are used only for gel electrophoresis currently. For reflectance measurements, both absorbance and fluorescence measurements are popular. Substances that absorb light in the UV or visible range are detected using

absorption. Substances that are irradiated at a definite wavelength and produce fluorescent light are detected using fluorescence microscopy. Fluorescence microcopy is a better detection method in comparison to fluorescence quenching and absorption measurements due to increased selectivity, sensitivity, and linearity with the signal independent from zone shape. Recent advances in detection include coupling TLC with mass spectroscopy or surface enhanced Raman spectroscopy.

1.13 Relation to Dissertation

Thin-layer chromatography and the associated evaluation metrics were used for two studies performed in this dissertation. Chromatographic theory describes how to obtain a more efficient separation by reducing plate height. Van Deemter explains different variables to manipulate in order to reduce the band dispersion terms: eddy diffusion, molecular diffusion, and resistance to mass transfer. Part of this dissertation takes a previous study from Kirchner et al. to attempt further improvements in efficiency.[30] Kirchner creates the first open separation platform using photolithography to fabricate pillar arrays. The pillar arrays in her work eliminate the eddy diffusion term and the mass transfer term in the stationary phase. The arrays are perfectly ordered and sorption and desorption occur at a rapid enough rate to ignore these terms. The study in this dissertation describes using pillar arrays and further decreasing the gaps between the perfectly order system to see the effect on plate height. Particle diameter is an important variable in chromatographic equations and the effects of reducing interstitial space between pillars is a notable study to conduct. The other study that uses TLC is seen in Chapter 5. A method was developed to couple TLC with surface enhanced Raman spectroscopy to enhance the chemically specificity of the detection methods typically used with TLC.

1.14 References

1. Touchstone, J. C., 3rd ed.; John Wiley & Sons: New York, 1992.
2. Miller, J. M., John Wiley & Sons, Inc.: Hoboken, NJ, 2005.
3. Sherma, J.; Fried, B., 3rd ed.; Marcel Dekker, Inc.: 2003; p 1016.
4. Martin, A. J. P.; Synge, R. L. M., *Biochemical Journal* **1941,** *35* (12), 1358-1368.
5. van Deemter, J. J.; Zuiderweg, F. J.; Klinkenberg, A., *Chem. Eng. Sci.* **1956,** *5*, 271.
6. Guiochon, G.; Siouffi, A., *Journal of Chromatographic Science* **1978,** *16* (10), 470-481.
7. Hauck, H. E.; Bund, O.; Fischer, W.; Schulz, M., *J. Planar Chromatogr.* **2001,** *14* (234).
8. Saha, A.; Mitra, S.; Tweedie, M.; Roy, S.; McLaughlin, J., *Microfluid Nanofluid* **2009,** *7* (4), 451-465.
9. Clark, J. E.; Olesik, S. V., *Journal of Chromatography A* **2010,** *1217* (27), 4655-4662.
10. Beilke, M. C.; Zewe, J. W.; Clark, J. E.; Olesik, S. V., *Analytica Chimica Acta* **2013,** *761*, 201-208.
11. Jim, S. R.; Oko, A. J.; Taschuk, M. T.; Brett, M. J., *Journal of Chromatography A* **2011,** *1218*, 7203-7210.
12. Jim, S. R.; Foroughi-Abari, A.; Krause, K. M.; Li, P.; Kupsta, M.; Taschuk, M. T.; Cadien, K. C.; Brett, M. J., *Journal of Chromatography A* **2013,** *1299*, 118-125.
13. Clicq, D.; Tjerkstra, R. W.; Gardeniers, J. G. E.; van den Berg, A.; Baron, G. V.; Desmet, G., *Journal of Chromatography A* **2004,** *1032* (1–2), 185-191.
14. Desmet, G.; Clicq, D.; Gzil, P., *Analytical Chemistry* **2005,** *77* (13), 4058-4070.
15. De Malsche, W.; Clicq, D.; Verdoold, V.; Gzil, P.; Desmet, G.; Gardeniers, H., *Lab on a Chip* **2007,** *7* (12), 1705-1711.
16. De Malsche, W.; Eghbali, H.; Clicq, D.; Vangelooven, J.; Gardeniers, H.; Desmet, G., *Anal. Chem.* **2007,** *79*, 5915.
17. Malsche, W. D.; Gardeniers, H.; Desmet, G., *Analytical Chemistry* **2008,** *80* (14), 5391-5400.
18. Desmet, G.; Broeckhoven, K., *Analytical Chemistry* **2008,** *80* (21), 8076-8088.
19. Tiggelaar, R. M.; Verdoold, V.; Eghbali, H.; Desmet, G.; Gardeniers, J. G. E., *Lab on a Chip* **2009,** *9* (3), 456-463.
20. Detobel, F.; De Bruyne, S.; Vangelooven, J.; De Malsche, W.; Aerts, T.; Terryn, H.; Gardeniers, H.; Eeltink, S.; Desmet, G., *Analytical Chemistry* **2010,** *82* (17), 7208-7217.
21. Desmet, G.; Eeltink, S., *Analytical Chemistry* **2012,** *85* (2), 543-556.
22. Leinweber, F. C.; Lubda, D.; Cabrera, K.; Tallarek, U., *Anal. Chem.* **2002,** *74*, 2470.
23. Leinweber, F. C.; Tallarek, U., *J. Chromatogr., A* **2003,** *1006*, 207.
24. Bruns, S.; Grinias, J. P.; Blue, L. E.; Jorgenson, J. W.; Tallarek, U., *Analytical Chemistry* **2012,** *84* (10), 4496-4503.
25. Daneyko, A.; Hlushkou, D.; Khirevich, S.; Tallarek, U., *J. Chromatogr., A* **2012,** *1257*, 98.
26. He, B.; Regnier, F., *J. Pharm. Biomed. Anal.* **1998,** *17*, 925.
27. He, B.; Tait, N.; Regnier, F., *Anal. Chem.* **1998,** *70*, 3790.
28. Regnier, F. E., *HRC-J. High Resolut. Chromatogr.* **2000,** *23*, 19.
29. Taylor, L. C.; Lavrik, N. V.; Sepaniak, M. J., *Analytical Chemistry* **2010,** *82* (22), 9549-9556.

30. Kirchner, T. B.; Hatab, N. A.; Lavrik, N. V.; Sepaniak, M. J., *Analytical Chemistry* **2013,** *85* (24), 11802-11808.
31. Charlton, J. J.; Jones, N. C.; Wallace, R. A.; Smithwick, R.; Bradshaw, J. A.; Kravchenko, I. I.; Lavrik, N. V.; Sepaniak, M. J., *Analytical Chemistry* **2015,** *87*, 6814-6821.
32. Kandziolka, M.; Charlton, J. J.; Kravchenko, I. I.; Bradshaw, J. A.; Merkulov, I. A.; Sepaniak, M. J.; Lavrik, N. V., *Analytical Chemistry* **2013,** *85* (19), 9031-9038.
33. Wells, S. M.; Merkulov, I. A.; Kravchenko, I. I.; Lavrik, N. V.; Sepaniak, M. J., *ACS Nano* **2012,** *6* (4), 2948-2959.
34. Pelander, A.; Backstrom, D.; Ojanpera, I., *J. Chromatogr., B* **2007,** *857*, 337.
35. Cimpoiu, C.; Hosu, A.; Briciu, R.; Miciaus, V., *J. Planar Chromatogr.−Mod. TLC* **2007,** *20*, 407.
36. Kirchner, T. B.; Strickhouser, R. B.; Hatab, N. A.; Charlton, J. J.; Kravchenko, I. I.; Lavrik, N. V.; Sepaniak, M. J., *Analyst* **2015,** *140* (10), 3347-3351.
37. Srivastava, M., 1 ed.; Springer-Verlag Berlin Heidelbery 2011; p 397.

Chapter 2

Nano and Micro Fabricated UTLC

2.1 Introduction

The lithographically fabricated separation platforms created in this research are considered a form of ultra-thin layer chromatography (UTLC) as discussed in Chapter 1. Briefly, the most significant advantages of UTLC, over that of TLC and HPTLC, are the absence of any binders, reduced migration times and distances, and reduction of solvent consumption.[1] Table 2.1 displays the common parameters of all three separation techniques for easy comparison. Pore structures of the monolithic silica gel layer in UTLC are 3-4 nm (meso) up to 1-2 µm (macro) with a pore volume of ~0.3 mL g^{-1} and a specific surface area of ~350 m^2 g^{-1}. Sample application volumes are usually in the range of 5-200 nL, solvent front distances of 1-3 cm, development times of 1-6 min, with only 1-4 mL of mobile phase consumed.[2]

These advancements to traditional chromatography are the basis for some of the work done in this dissertation. In this research, pillar arrays fabricated using photolithography on a silicon wafer serve as a separation platform. UTLC suffers from lower resolution because of short development distances, smaller overall specific adsorption surface area, and issues with incorporating traditional TLC/HPTLC equipment on ultra-thin layers. Automatic samplers typically cannot handle sample volumes less than 100 nL.[2] The purpose of the separation studies done in Chapter 6, was to determine if manipulating the inter pillar distances would increase development flow velocity and reduce band dispersion.

Kirchner et al. was the first to explore open channel pillar array systems as a separation medium.[3] The studies from Kirchner's work explored the impact on mass transport and chromatographic efficiency with a perfectly ordered separation platform. The focus was on the fabrication of the pillar arrays, studies of solvent transport, methods to create compatible sample spots, and initial evaluation of band dispersion. Kirchner observed that the mobile phase velocity of the pillar array systems increased compared to TLC plates. Another experiment concluded that the velocity also increased when the inter-pillar gap decreased (pillar diameter held constant). Perfectly ordered pillar arrays were determined to have a significant increase in efficiency with little to no

Table 2.1: Comparison of TLC and UTLC Pillar Array Chromatographic Platforms

Type	**Thickness**	**Particle Size**	**Sample Size**
Traditional TLC	250 µm	10-12 µm	≥ 1 µL
HPTLC	± 150 µm	5-6 µm	50-500 nL
µ-Pillar Array	~ 20 µm	1-3 µm	pL-nL
n-Pillar Array	~2 µm	150-300 nm	pL-nL

C_M term present. The work presented in this dissertation is an expansion of Kirchner's first study performed on pillar array open chromatographic platforms. The experimental procedure to fabricate pillar arrays is well documented in Kirchner's first publication as well as described in the proceeding sections of this chapter.

2.2 Photolithography

Photolithography (or Optical lithography) is a photon-based technique comprised of projecting an image into a photosensitive emulsion (photoresist) coated onto a substrate.[4] It is the most widely used lithography process for the manufacturing of nanoelectronics in the semiconductor industry (~$200 billion worldwide). The vast use of photolithography is due to its ability to transfer complex patterns very quickly and the ability to implement different wavelength and optical configurations. Wavelength possibilities include traditional visible to UV ranges, extreme UV range, and even soft x-ray. Optical configurations include direct shadow casting to complex multi-element refractive and/or reflective imaging.[4]

The entire photolithography procedure is a lengthy and meticulous process. Figure 2.1 is an illustration of the photolithographic process step by step. The first step in the procedure is silicon wafer cleaning. Contaminants must be removed prior to photoresist coating (i.e. dust from scribing or cleaving, abrasive particles, lint), which usually involves a soak and rinse or ultrasonic agitation. It is important to note that creating a photolithographic substrate requires a clean room to ensure minimization of impurities (biggest contributor to defects). To ensure proper adhesion of the photoresist to the silicon wafer, the wafer must be primed. Ideally, the wafer should have no water on the surface and is therefore subject to a dehydration bake by spending ~15 minutes in convection oven at 80-90°C. Primers used for silicon wafers form bonds with the surface and produce a polar surface usually based on siloxane linkages (Si-O-Si).

After the wafer is cleaned and primed the photoresist is ready to be spin coated onto the surface. Resist thicknesses are controlled by spin-coating with a pre-determined rate based on the specific resist. The photoresist used for the work done in this

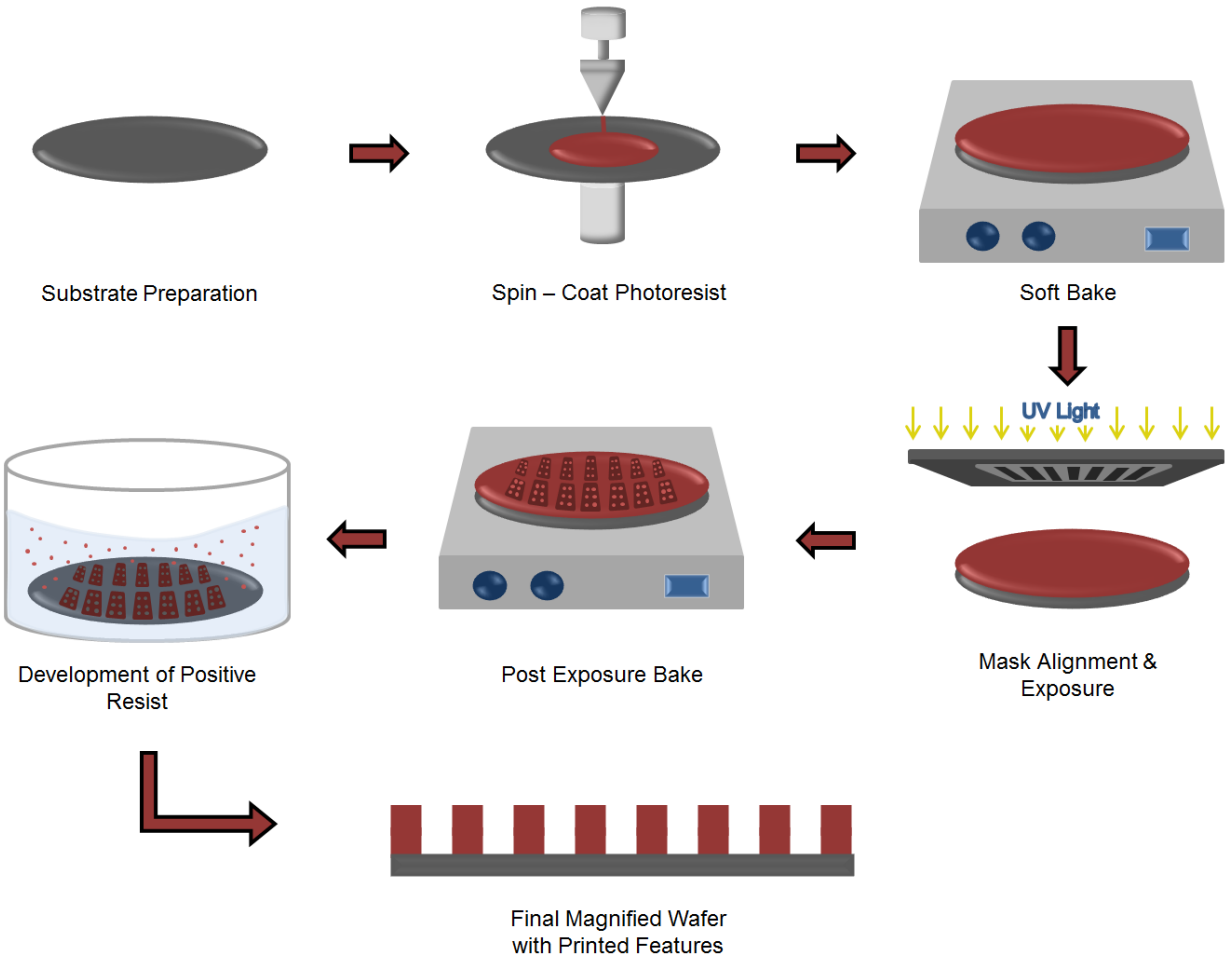

Figure 2.1: Typical photolithographic process with emphasis on the patterns used in this dissertation.

dissertation is LOR-1A with spin rates between 2500-4500 rpm to achieve 100-150 nm thick resist. Figure 2.2 exhibits the stages of resist coating where the ideal situation is stage 1 (equilibrium). Spinning artifacts (i.e. striations, edges, streaks) can cause non-uniformity or defects in the final photolithographic substrate. Then, a prebake (soft bake) of the wafer is performed on a hot plate to evaporate the coating solvent and densify the resist.

Now, the wafer is ready for light exposure. A quartz plate mask, which has a laser written pattern with desired features, is aligned with the substrate in order to print the features onto the wafer. Exposure time depends on the photoresist used and the strength of the light source. Three different methods can be performed when exposing the wafer to light to imprint a pattern. For this dissertation work, the contact method was used, allowing for excellent resolution, with a UV light source. If the wafer and substrate are not in direct contact (projection or proximity exposure) the resolution suffers.[5-6] However, a disadvantage to this technique is that the contact between the mask and substrate can cause damage resulting in feature imperfections.

The next step consists of a post exposure bake (PEB or hard bake) in order to stabilize and harden the developed photoresist prior to the processing step that the resist will mask. This step removes any remaining traces of the coating solvent or developer. The PEB also helps reduce the standing wave effect, which occurs when monochromatic light has been projected onto a lithographic surface at multiple angles. This effect causes a reduction in feature quality by creating a ridge formation on the sidewalls from high and low intensity waves.[6-7] Photoresist removal comes directly after the PEB by using the appropriate solvent (for positive photoresist normally acetone, trichloroethylene, or phenol-based strippers) or by plasma etching with O_2.

To further enhance the resolution of our photolithographic substrates (pillar arrays in Chapter 6) we modified the typical lithographic method described above to include a double layer of photoresist and a chromium metal deposition to create a hard mask prior to etching the silicon wafer (See Figure 2.3). The chromium is deposited using a dual electron beam physical vapor deposition method. After the chromium is finished

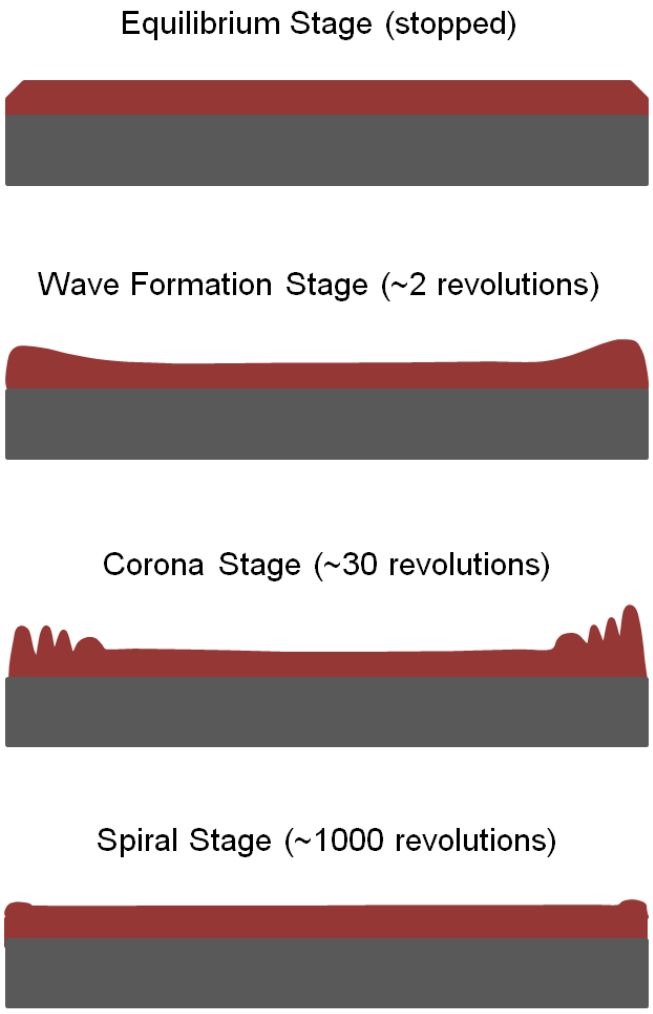

Figure 2.2: Stages of resist coating onto a silicon wafer. The goal is to reach an equilibrium stage after spinning is finished but spinning artifacts can cause a less ideal coating scenario.

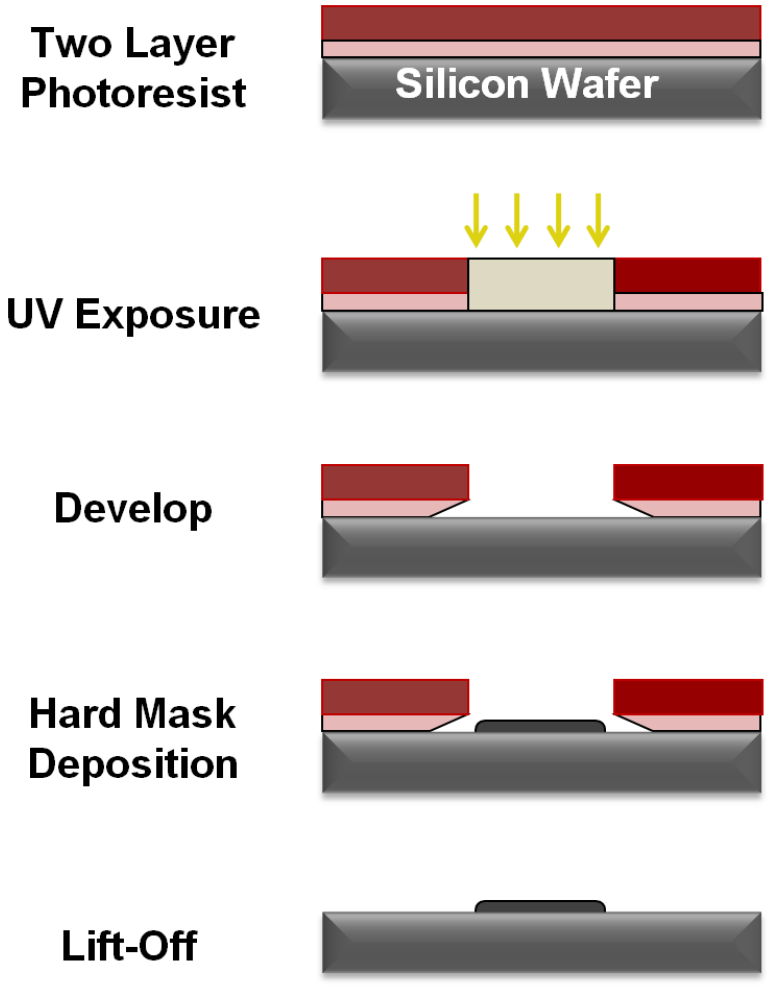

Figure 2.3: Double layer lift-off photoresist for improved lithographic resolution.

depositing a lift-off process is implemented to remove any remaining photoresist and excess chromium. The photolithography portion of the separation platforms created in this dissertation has been fully described in this section. The next step for our wafers includes an etching step for the patterned features (See Section 2.3).

2.3 Reactive Ion Etching

Reactive ion etching is an important next step in processing our wafer to create a separation platform. Patterned resist (as discussed above) transfers a pattern into other layers by either dry etching in a reactive plasma, wet chemical etching, ion implantation for electrical doping, or deposition of thin film layers.[8] The most widely used method for high resolution pattern transfer is dry etching. Dry etching encompasses a number of different and related techniques but the focus of this dissertation is on reactive ion etching (RIE) (also sometimes called reactive sputter etching). Dry etching, in contrast to wet etching, utilizes an ionized gas instead of a liquid etchant and is an anisotropic etching method leading to sharp controlled features (See Figure 2.4). Wet etching is not frequently used for nanofabrication due to the slow procedure, possessing little control over position and direction, and creating undercutting beneath the mask thereby decreasing the stability of very small features (isotropic etch).

Reactive ion etching introduces a reactive gas into an evacuated process chamber and RF induced plasma to create reactive ion species. The electric field accelerates the ions toward the wafer. The RIE process is a combination of a chemical and physical etching process. The physical process occurs from high energy ions that knock atoms out of the substrate surface through a transfer of kinetic energy. The chemical process is the formation of gaseous material at the surface of the substrate. The etch profile and depth can be controlled by the type and amount of gases used and gas flow rate.[9]

For the fabricated photolithographic pillar arrays created for this dissertation, deep reactive ion etching was used utilizing a Bosch recipe to enhance surface area (scalloped pillar sidewalls) and improve pillar stability. The Bosch process involves a high etch rate and silicon selectivity from the recipe which creates vertical sidewalls and high-aspect ratio features in silicon wafers. The first step involves the etch step which is

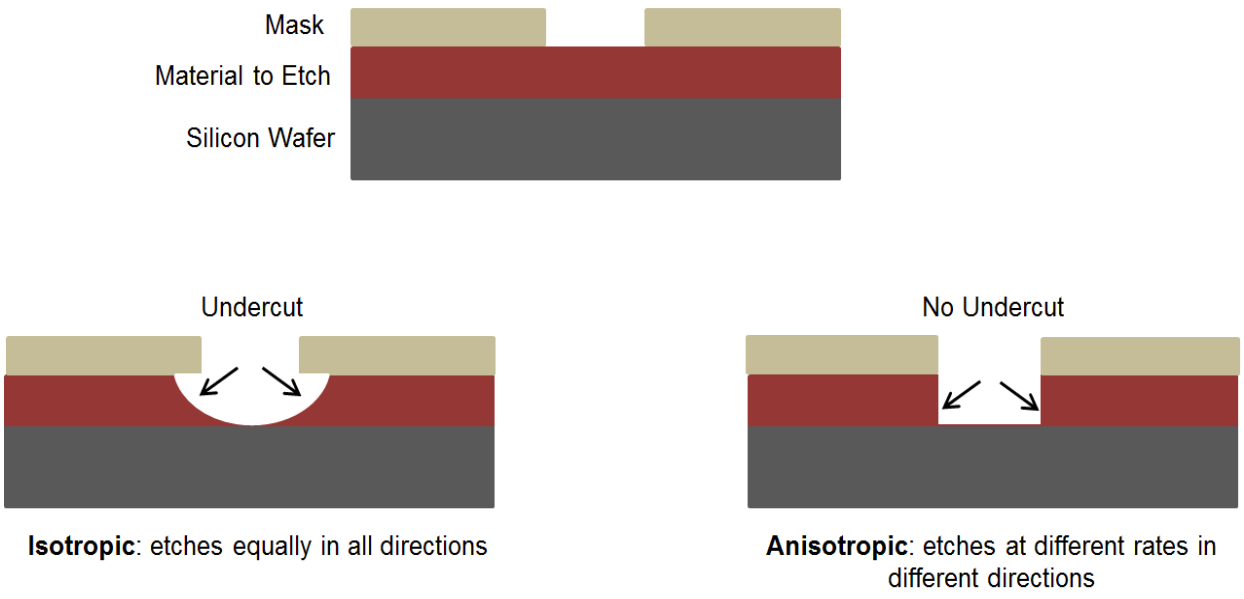

Figure 2.4: Comparison between Isotropic and Anisotropic etching

performed on exposed silicon using isotropic SF_6 gas. The next step is the passivation step which is performed by a deposition of C_4F_8 polymer onto the entire wafer surface. This cycle repeats resulting in a physical etch process that rapidly removes the fluoropolymer it directly contacts (i.e. the unmasked portions of the wafer). After the physical etch, the chemical etch (RIE) occurs where the fluoropolymer is not as rapidly etched which results in the accumulation of fluoropolymer on the pillar sidewalls. The continuous cycle of etch and passivation steps cause scalloped pillar sidewalls whereas the remainder of the chip contains smooth surfaces. The excess fluoropolymer protects the pillars during the anisotropic etching process. To optimize each substrate the exposure time of SF_6 and C_4F_8 is manipulated and the cycle repeats to obtain desired feature heights. The pillar arrays in this research were etched to a height of ~20 µm (See Figure 2.5).

2.4 Electron Beam Lithography

Electron beam lithography allows for two-dimensional patterns down to the nanometer scale. The technique involves the exposure of a highly focused electron beam to modify the solubility of a resist material allowing a pattern to surface after a development step. The major difference between normal photolithography and EBL is that in order to investigate deterministic arrays with features less than 1 micron it is necessary to utilize electron beam lithography. Another difference is that EBL does not require a mask to create a pattern as a normal photolithography substrates require.[10] However, this serial writing process is slow. Both photolithography and EBL generate chromatographic platforms that are highly ordered and reproducible. Important disadvantages of EBL include the cost and time constraints of fabrication but the advantages of good resolution (±10 nm) and re-usability outweigh the inherent limitations. In order to increase throughput of EBL substrates advancements in techniques have been pursued such as electron projection lithography, variable-shaped beam lithography and low-energy electron beam proximity projection lithography but at the cost of poorer resolution.[11-13]

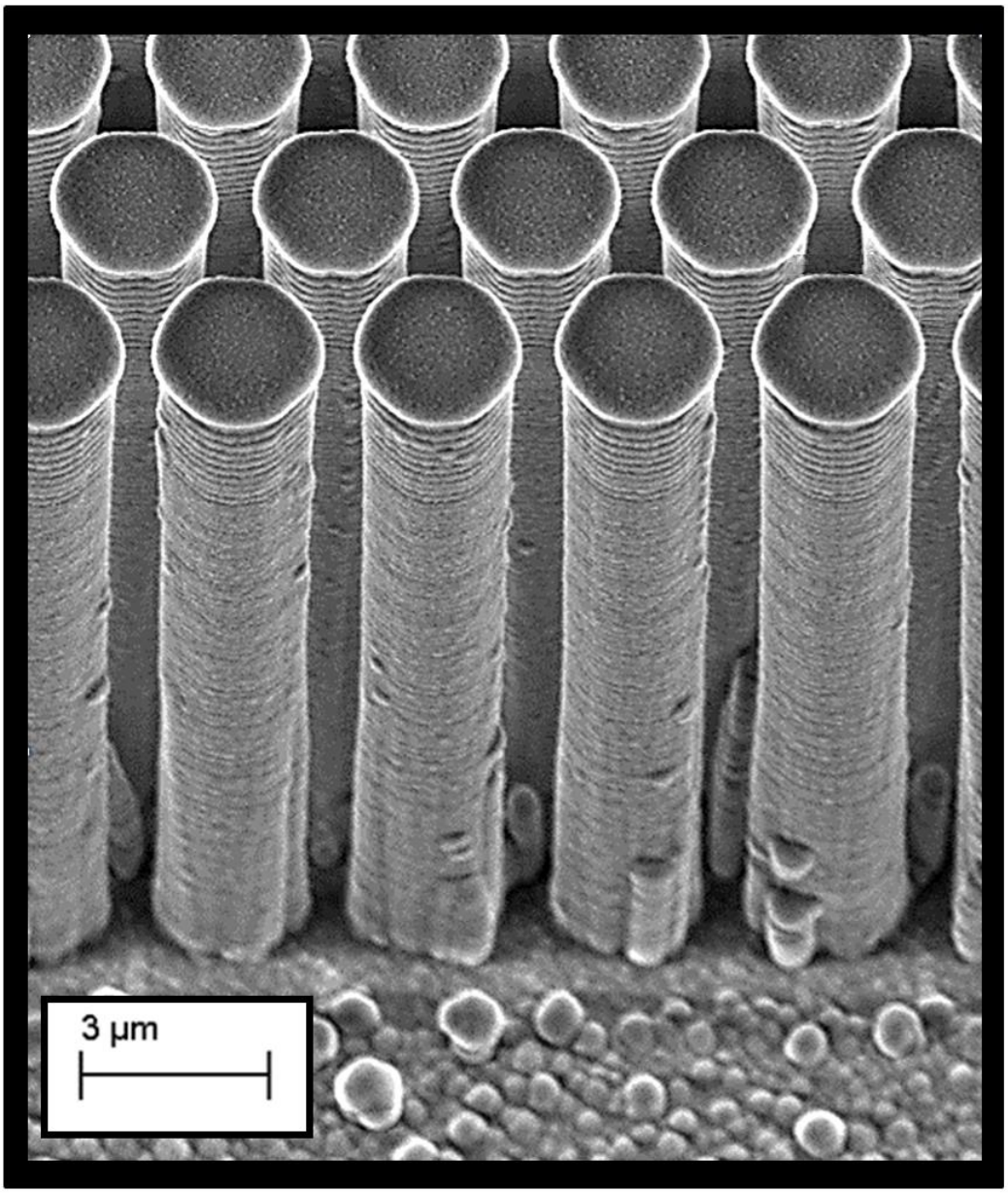

Figure 2.5: Typical pillar arrays used in the research conducted in this dissertation with a height of ~20 µm. The pillar array depicted here have 50 nm of porous silicon oxide (PSO) deposited for enhanced surface area.

A typical EBL system can be seen in Figure 2.6 where the three main components are an electron gun, a vacuum system or column to focus the electron beam, and a computer system to control the various parts.[14] The first step includes producing the electrons by cathodes or electron emitters with the electron gun which controls the creation of the electron beam. With the formation of the electron beam, the electrons are accelerated by electrostatic fields producing greater energy. The electrons are focusing into a beam and the manipulation of the beam occurs under a high vacuum. A series of electric and magnetic lenses focuses and deflects the beam to specific spots on the substrate. A computer assisted design (CAD) is loaded to control the pattern writing process.[15] The CAD design allows the control system to intermittently turn the beam on and off so only the intended locations have the desired pattern.

The work presented in this dissertation concerns only traditional photolithography with manipulating inter pillar gap dimensions (Chapter 6) but EBL is important to mention as a future application for ultra-thin layer chromatography platforms. Kirchner et al. performed some preliminary work on EBL separation platforms concluding that high efficiency could be obtained.[16] These chromatographic platforms contain features (1-2 µm pillar heights) smaller than what is used in ultra-thin layer chromatography. Future work with EBL substrates as chromatographic platforms is possible in order to optimize the separation process.

2.5 Applications of Lithographically Fabricated Separation Platforms

Photolithography fabrication processes were traditionally designed for the semiconductor industry but have recent applications in the development of on-chip separation techniques. In 1998, Regnier and coworkers were the first to demonstrate that the fabrication used in the semiconductor industry could be applied towards chromatographic columns in order to achieve highly ordered, reproducible monolith structures.[17-18] The Regnier group predicted that microfabrication techniques would increase speed, resolution, and throughput in analytical liquid chromatography by designing highly ordered micro-features. Desmet et al. expanded on Regnier's work with theoretical calculations proving that the perfectly ordered system in

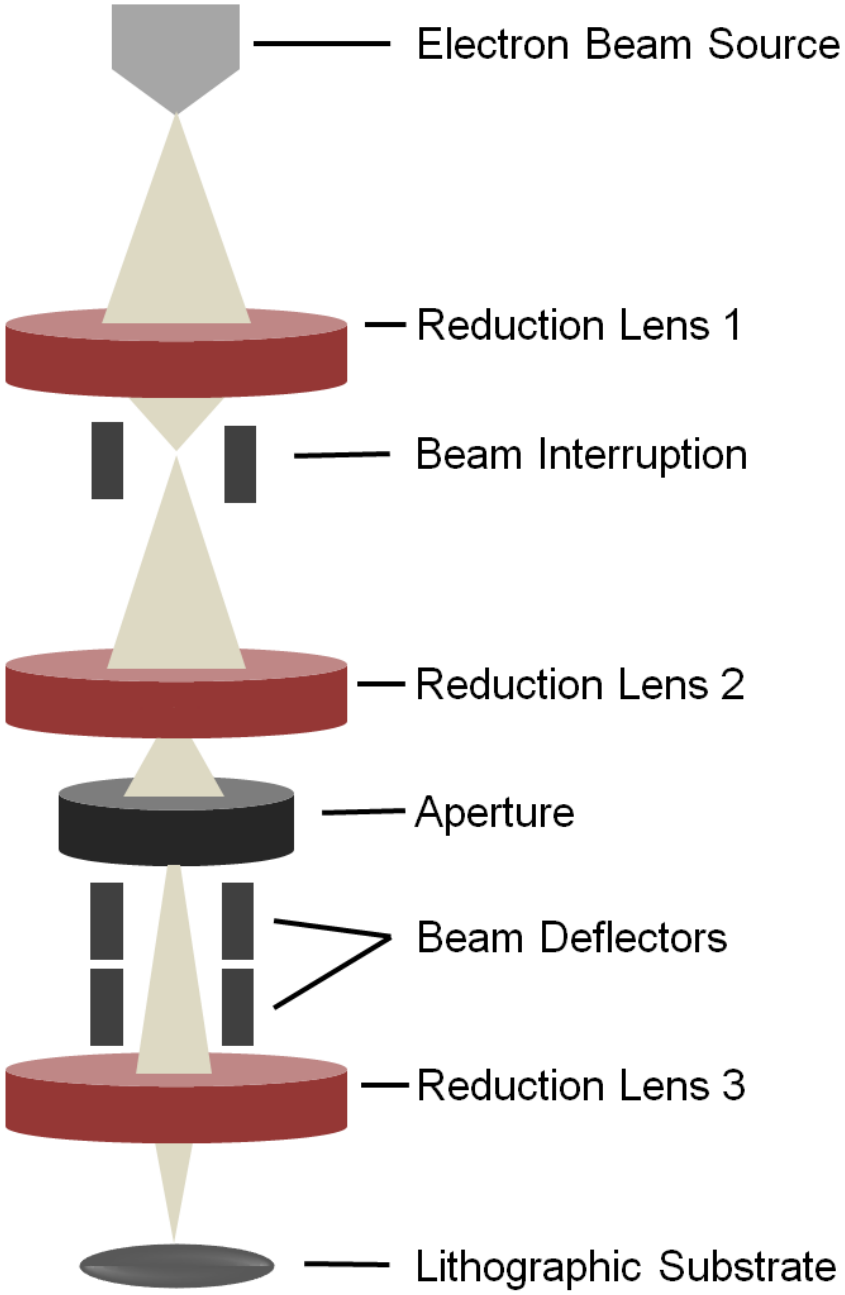

Figure 2.6: A typical EBL system with three main components of an electron gun, vacuum column, and a computer system for automated control.

chromatography would reduce plate height.[19] The Desmet group also worked on enclosed, pressure driven liquid chromatography systems yielding successful separations giving plate heights around 4 µm.[20-23] Separation efficiency with lithographically-fabricated pillars can be much higher when compared to polydisperse and heterogeneous packing particles of traditional chromatographic columns. Mass transfer efficiency improves when smaller particles are implemented in monolithic columns. In traditional columns, implementing smaller particles usually increases the non-uniformity of the packing and the pressure demands, whereas, scaling down pillar array separation platforms is highly uniform and has shown less flow resistance.

After the first implementation of pillar arrays as chromatographic platforms optimization techniques became increasingly important to improve efficiency, resolution, band dispersion, etc. In order to replicate a similar packed bed as conventional liquid chromatography uses, where a mobile phase-stationary phase partitioning separation is controlled by the retentive nature of the solute within the system, Desmet and colleagues implemented C8 and C18 liquid phases onto both porous and non-porous pillar array separation mediums.[21, 24-26] Increasing the surface area of pillar arrays is another area of study to consider in order to obtain a similar mass loadability, mechanical stability, and stationary phase as conventional HPLC columns. Several methods have been used in order to achieve a larger surface area on the lithographically fabricated substrate. Electrochemical anodization[20, 27] and sol-gel[28] chemistry have both been successful treatments to increase the surface area of pillar arrays for separations. The most recent surface area studies on pillar array separation mediums have been performed by the Sepaniak group. Both Charlton and Kirchner use a room temperature procedure on a plasma enhanced chemical vapor deposition (PECVD) instrument that creates a PSO layer containing pore sizes of 5 to 10 nm.[16, 29] This PSO layer was implemented in the studies involving pillar arrays seen in Chapter 6 of this dissertation.

Recent advancements in the pillar arrays for separations field includes separations of various analytes and fabrication of pillars using various forms of lithography. Deep-UV lithography has become a popular lithography technique to fabricate pillar arrays.[30-

[31] Desmet and coworkers used deep-UV lithography combined with deep reactive ion etching (DRIE) technology to fabricate pillar array and test for efficiency in a pressurized system. The group experimented with a range of pillar diameters (~ 5 to 0.5 µm) and determined that etching resolution suffers with inter-pillar distances smaller than a micrometer in deep UV-lithography substrates. Elution behavior of short dsDNA strands has been evaluated with silicon micropillar arrays columns using ion pair reversed-phase chromatography.[32] Desmet et al. has also implemented a pillar array chip out of cyclo-olefin polymer sheets in a closed system that was an inexpensive alternative to silicon based separation platforms.[33] As stated above, Kirchner was the first to explore pillar arrays in open systems with simple capillary action as the driving force for the mobile phase solvent.[3] Charlton et al. developed a metal dewetting procedure for pillar arrays as a cost reduction technique.[29, 34] The dissertation herein describes attempts at improving efficiency in pillar array separation platforms by reducing the inter pillar gap in open, capillary driven systems. After the lithography process is complete, a simple way to reduce inter pillar gap is to use atomic layer deposition (ALD) and PECVD in order to increase the surface area instead of fabricating different inter pillar gap distances using lithography each time. ALD is a conformal deposition allowing for great reproducibility between subsequent substrates. An in depth discussion on the performance of these pillar arrays can be seen in Chapter 6.

2.6 Relation to Dissertation

Photolithographically fabricated pillar arrays were studied as a separation platform in this dissertation. The main focus was taking the open system, capillary driven platform from Kirchner et al.[3] and manipulating the inter pillar gap with the goal to further increase efficiency. A basic understanding of how these unique platforms are fabricated is important in order to study retention characteristics, band dispersion, and, therefore, efficiency. Surface modifications, such as a C8 or C18 phase, are required to create a reversed phase separation medium. Increasing surface area using a PSO deposition was utilized based on a successful reduction in plate heights and band dispersion from the Sepaniak group. Understanding the basic principles of micro- and nano- fabrication helps aid in the optimization of current pillar array separation platforms.

2.8 References

1. Mennickent, S.; De Diego, M.; Vega, M., *Chromatographia* **2013,** *76* (19-20), 1233-1238.
2. Hauck, H. E.; Schulz, M., *Chromatographia* **2003,** *57* (1), S313-S315.
3. Kirchner, T. B.; Hatab, N. A.; Lavrik, N. V.; Sepaniak, M. J., *Analytical Chemistry* **2013,** *85* (24), 11802-11808.
4. Naulleau, P., CRC Press Taylor & Francis Group Boca Raton, FL, 2012.
5. Rothschild, M.; Bloomstein, T. M.; Fedynyshyn, T. H.; R. R. Kimz, V. L.; Switkes, M.; Jr., N. N. E.; Palmacci, S. T.; Sedladek, J. H. C.; Hardy, D. E.; Greenville, A., *Lincoln Laboratory Journal* **2003**.
6. Taylor, L. The fabrication and integration of pillar array channels for chip based separations and analysis. University of Tennessee, Knoxville, TN, 2012.
7. Mack, C. A., Wiley: Hoboken, NJ, 2007.
8. Tennant, D. M., *journal of Vacuum Science Technology* **2013,** *31* (5).
9. Tennant, D. M., Springer New York: New York, 1999.
10. Kirchner, T. B. The fabrication of micro- and nano- scale deterministic and stochastic pillar arrays for planar separations. University of Tennessee, Knoxville, TN, 2015.
11. Wells, S. M. Improving analytical utility of Surface Enhanced Raman Spectroscopy through unique lithographic substrate development. Dissertation, University of Tennessee, Knoxville, TN, 2012.
12. Berger, S. D.; Gibson, J. M.; Camarda, R. M.; Farrow, R. C.; Huggins, H. A.; Kraus, J. S.; Liddle, J. A., *Journal of Vacuum Science & Technology B* **1991,** *9*, 2996-2999.
13. Pfeiffer, H. C., *Journal of Vacuum Science & Technology B* **1978,** *15*, 887-890.
14. Saitou, N., *International Journal of the Japan Society for Precision Engineering* **1996,** *30* (2), 107-111.
15. Yamazake, K., World Scientific Hackensack, NJ, 2008.
16. Kirchner, T. B.; Strickhouser, R. B.; Hatab, N. A.; Charlton, J. J.; Kravchenko, I. I.; Lavrik, N. V.; Sepaniak, M. J., *Analyst* **2015,** *140* (10), 3347-3351.
17. He, B.; Regnier, F., *J. Pharm. Biomed. Anal.* **1998,** *17*, 925.
18. Regnier, F. E., *J. High Resolut. Chromatogr.* **2000,** *23* (1), 19.
19. Gzil, P.; Vervoort, N.; Baron, G. V.; Desmet, G., *Analytical Chemistry* **2003,** *75* (22), 6244-6250.
20. De Malsche, W.; Clicq, D.; Verdoold, V.; Gzil, P.; Desmet, G.; Gardeniers, H., *Lab on a Chip* **2007,** *7* (12), 1705-1711.
21. De Malsche, W.; Eghbali, H.; Clicq, D.; Vangelooven, J.; Gardeniers, H.; Desmet, G., *Anal. Chem.* **2007,** *79*, 5915.
22. De Smet, J.; Gzil, P.; Vervoort, N.; Verelst, H.; Baron, G. V.; Desmet, G., *Anal. Chem.* **2004,** *76*, 3716.
23. Op De Beeck, J.; Callewaert, M.; Ottevaere, H.; Gardeniers, H.; Desmet, G.; De Malsche, W., *Analytical Chemistry* **2013,** *85* (10), 5207-5212.
24. Eghbali, H.; De Malsche, W.; Clicq, D.; Gardeniers, H.; Desmet, G., *LC–GC Eur.* **2007,** *20*.
25. Malsche, W. D.; Gardeniers, H.; Desmet, G., *Analytical Chemistry* **2008,** *80* (14), 5391-5400.

26. Eghbali, H.; Matthijs, S.; Verdoold, V.; Gardeniers, H.; Cornelis, P.; Desmet, G., *J. Chromatogr. A* **2009,** *1216*, 8603.
27. Tiggelaar, R. M.; Verdoold, V.; Eghbali, H.; Desmet, G.; Gardeniers, J. G. E., *Lab on a Chip* **2008,** *9*, 456-463.
28. De Malsche, W.; De Bruyne, S.; De Beeck, J. O.; Eeltink, S.; Detobel, F.; Gardeniers, H., *J. Sep. Sci.* **2012,** *35*, 2010.
29. Charlton, J. J.; Lavrik, N.; Bradshaw, J. A.; Sepaniak, M. J., *ACS Applied Materials & Interfaces* **2014,** *6* (20), 17894-17901.
30. Op de Beeck, J.; De Malsche, W.; Tezcan, D. S.; De Moor, P.; Desmet, G., *Journal of Chromatography A* **2012,** *1239*, 35-48.
31. Op de Beeck, J.; De Malsche, W.; De Moor, P.; Desmet, G., *Journal of Separation Science* **2012,** *35* (15), 1877-1883.
32. Zhang, L.; Majeed, B.; Lynen, F.; Van Hoof, C.; De Malsche, W., *ELECTROPHORESIS* **2012,** *33* (21), 3205-3212.
33. Illa, X.; De Malsche, W.; Bomer, J.; Gardeniers, H.; Eijkel, J.; Morante, J. R.; Romano-Rodriguez, A.; Desmet, G., *Lab on a Chip* **2009,** *9* (11), 1511-1516.
34. Charlton, J. J.; Lavrik, N. V.; Bradshaw, J. A.; Sepaniak, M. J., *J. Appl. Materials and Interfaces* **2014,** *6*, 17894-17901.

Chapter 3

Introduction to Surface Enhanced Raman Spectroscopy (SERS)

3.1 Fundamentals of Raman Spectroscopy

In 1928, the Raman effect or Raman scattering was discovered by the Indian physicist C.V. Raman. Raman spectroscopy detects molecular vibrations that occur from the interaction of a photon and the molecule under analysis. The interaction of molecules with photons can demonstrate absorption or scattering. For energy to be absorbed, it must be resonant with the molecule's vibrational frequencies. In the case of scattering, a dipole is induced due to a change in polarizability in the molecule's electron cloud (see Equation 3.2). The scattered light can either have the same frequency (Rayleigh scattering) or a different frequency (Raman) as the incident radiation.[1-2] Raman scattered photons (inelastic scattering) of lower frequency than the incident radiation are known as Stokes bands, and the scattered photons with greater frequency are referred to as anti-Stokes. Figure 3.1 shows a schematic diagram of the principle of Raman scattering.[3] The advantage with Raman scattering is that each molecule has its own unique spectra. In addition, Raman scattering is non-destructive, requires simple to no sample preparation, and provides versatile analysis of different states of matter.

The inelastic collisions that occur in Raman scattering induce an energy-transfer between the incident photons and the molecules of the analyte when exposed to an electromagnetic field (EMF).[4] Energy of the photons after the inelastic scattering occurs (E_s) can be expressed as:

$$E_s = h\nu \pm \Delta E_v \qquad [3.1]$$

Where:

h = Planck's Constant

ν = frequency

ΔE_v = difference in energy for the vibration

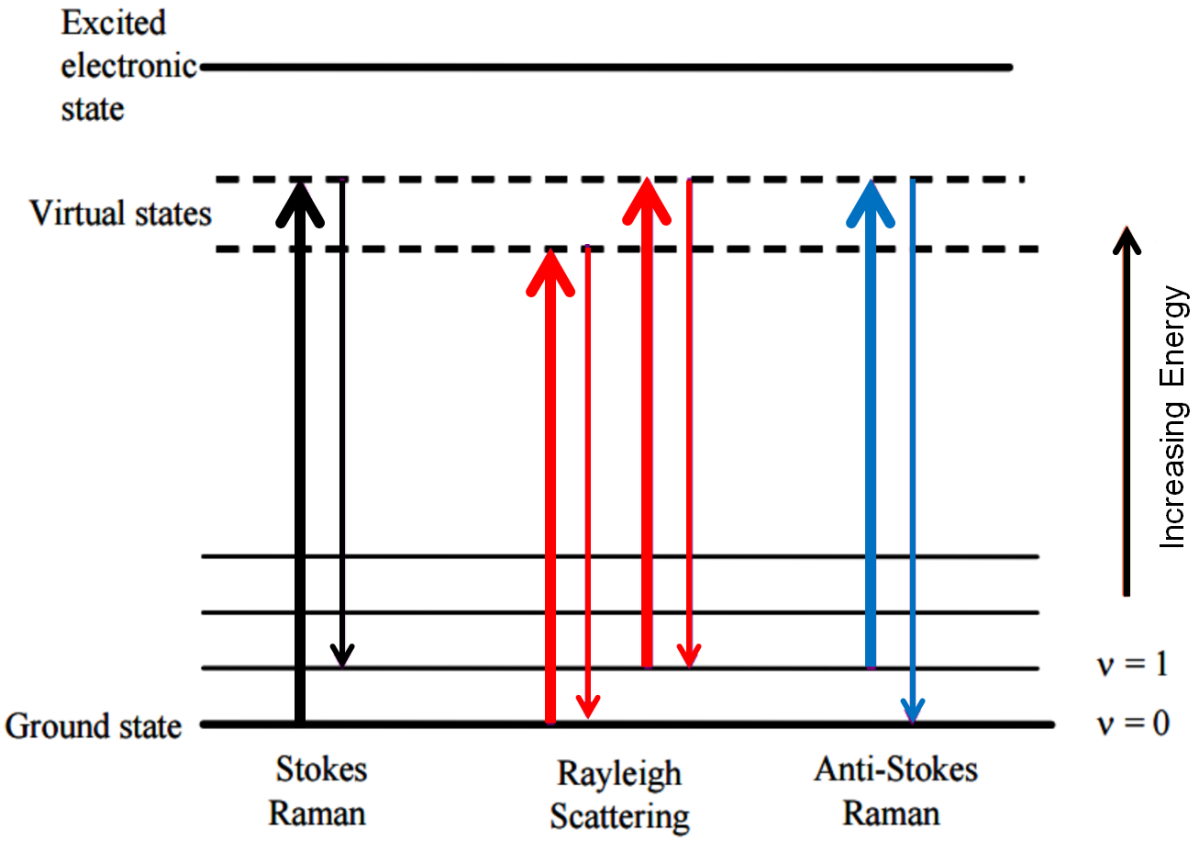

Figure 3.1: Schematic diagram of Rayleigh and Raman scattering.

The interaction between the oscillating field and the electron distribution of the analyte generates a dipole moment (μ), where the frequency is directly proportional to the incident electromagnetic field[5] as seen in the Equation 3.2 below:

$$\mu = \alpha E = \alpha E_0 \cos(2\pi v_i t) \quad [3.2]$$

Defined as:

E = magnitude of the electromagnetic field that surrounds the analyte

E_0 = peak amiplitude of the electromagnetic wave

v_i = frequency of the incident beam

t = time

α = polarizability of the bond

One disadvantage to Raman spectroscopy is that only a very small fraction (~1 in 10^8) of the photons are inelastically scattered causing the technique to be inherently insensitive.[5] The efficiency of a Raman scattering event can be determined by the Raman cross section (σ_{sc}):

$$\sigma_{sc} = \frac{2\pi I}{h v_i n_p} dA \quad [3.3]$$

Where:

h = planck's constant

σ_{sc} = scattering cross section

I = scattered intensity

n_p = number of photons

dA = area

The cross section estimates the rate at which energy is removed from the incident beam.[1]

$$\sigma_{sc} \propto \frac{1}{\lambda^4} \quad [3.4]$$

Where:

λ = wavelength of the incident photon

$$P_s \propto \frac{I_o}{\lambda^4} \quad [3.5]$$

In equation [3.5] the correlation of intensity of the incident light and power of the scattered light can be seen. In conventional Raman spectroscopy, the scattering cross section is on the order of 10^{-31} to 10^{-29} cm^2/molecule, which are 12-14 orders of magnitude smaller than a typical fluorescence cross section.[6] In order to enhance sensitivity surface enhanced Raman scattering was discovered, where Raman cross sections can be increased to be more comparable with fluorescence cross sections.

The Raman spectrometer used in this work is comprised of many components briefly described here. The confocal Raman microscope can be seen in Figure 3.2. Common laser sources for these microscopes are the argon ion (514.5 nm), krypton ion (530.9, 647.0 nm), diode lasers (782 and 830 nm), Nd/Yag (1064 nm), and the He/Ne (632.8 nm) lasers with typical power ≤ 25 mW.[7] A laser line filter can be used in order to isolate the desired laser line. Neutral density filters are used to adjust the power of the laser beam. After filtration of the laser line, the incoming radiation passes through a pinhole that rejects most of the specular reflections of the laser. The pinhole allows spatial homogeneity of the laser beam. Then the beam reaches the holographic notch filter which redirects it to the microscope objective. The purpose of the microscope objective is to increase the power density of the beam by focusing onto a small area of the sample. The Rayleigh and Raman scattering signals are then recollected by the objective in a 180° backscattering geometry. The holographic notch filter then filters the Rayleigh scattering from being detected by only transmitting the Raman scattered photons. A confocal hole filters the residual laser radiation and other interferences such

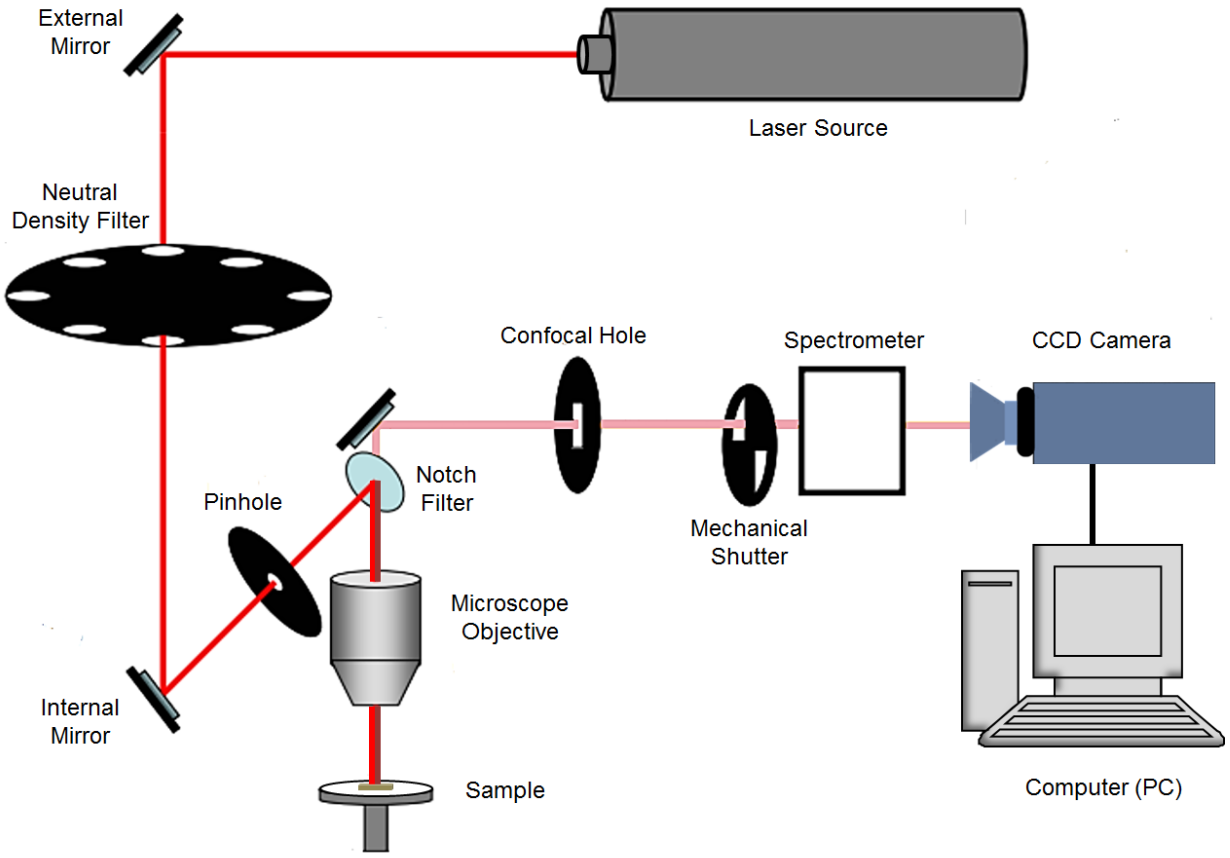

Figure 3.2: Schematic diagram of the confocal Raman instrument used for the studies conducted in this research.

as room light or fluorescence. A single stage spectrograph disperses the Raman photons which redirects the Raman signal to a charge coupled device (CCD) chip.[7] Finally, the digitized data is processed by a computer connected to the instrument with the appropriate software to decipher the Raman spectrum.

3.2 History & Introduction to SERS

The first observation of the Surface Enhanced Raman Scattering (SERS) effect was interpreted as an increase in surface area.[8-9] Jeanmarie and Van Duyne and independently Albrecht and Creighton explored other aspects of the enhancement of SERS.[10] Van Duyne and Creighton explained that of the effective Raman cross-section was exceptionally in excess of the increased number of molecules that adhered to the substrate due to the surface's roughness. In 1978, Moskovits proposed that the huge increase in Raman cross-section was in relation to the excitation of surface plasmons. This led to the discovery that SERS requires a substrate that is a good conductor.[10] Many other parameters such as excitation wavelength, polarization of the exciting and scattered radiation, and exact structural features of the SERS system were then explored and optimized.[5, 10]

The SERS effect is simply amplifying the Raman signal by several orders of magnitude.[5] The signal amplification comes mainly from the electromagnetic interaction of light with metals that produces strong electro-magnetic fields localized around nanoparticles through plasmon resonances. Normally, to gain an increase in signal intensity the molecules must be absorbed on to the metal surface or within a few nanometers of the surface. A whole field of study has been dedicated to developing SERS substrates in order to enhance the Raman signal. Common substrates contain metallic nano-structures, such as metallic colloids in solution or substrates fabricated by nano-lithography. More details on substrates are explained in Section 3.5.

3.3 Enhancement Mechanisms

As stated before, the limitation of conventional Raman scattering is one of very low cross section. Conversely, SERS can provide an increase in intensity of many orders of

magnitude depending on the metal, the molecules under analysis, and the incident laser wavelength.[5] SERS is becoming more widely used because it takes advantage of the information rich Raman spectrum and enhances the inherently weak signal. SERS signals are different from corresponding Raman signals with respect to their polarization properties of the metal. The SERS intensity for a given vibrational mode of a given analyte is proportional to the laser intensity and to the normal cross-section, as seen with conventional Raman, but affected by an enhancement factor (EF). The mechanisms responsible for SERS are roughly divided in three main categories: electromagnetic (EM), chemical enhancements (CE), and resonance effects. The EM enhancement focuses on the influence of the nanostructure´s shapes, and sizes to the enhancement of the induced electromagnetic field while the CE factor points toward the metal-ligand interactions that can occur upon adsorption of the analyte onto the surface of the metal.[5]

3.3.1 The Electromagnetic Theory

Three multiplicative theories contribute to SERS enhancements. The theory believed to contribute the most to enhancement is the electromagnetic theory. The electromagnetic EF is due to the coupling of the incident and Raman electromagnetic fields with the SERS substrate, which leads to an EF for the incident field and one for the re-emitted (Raman) field. The electromagnetic theory arises from the excitation of surface plasmons, known as localized surface plasmon resonance (LSPR). The electromagnetic fields surrounding a small illuminated metal particle creates the enhancement in the Raman spectrum. A small metal sphere will maintain oscillating surface plasmon multipoles induced by the time-varying electric-field vector of light.[5, 10] Surface plasmons are collective oscillations of the conduction electrons from the background of ionic metal cores.[10-11] Systems with delocalized electrons will undergo the excitations, and as a result the free electrons experience a more intense dipolar plasmon resonance (see Figure 3.3). An overall enhancement of $|E|^4$ is observed, which combines the square of the electrical field at the incident frequency and the square of the electrical field at the Raman scattered frequency (See Equation 3.10 and

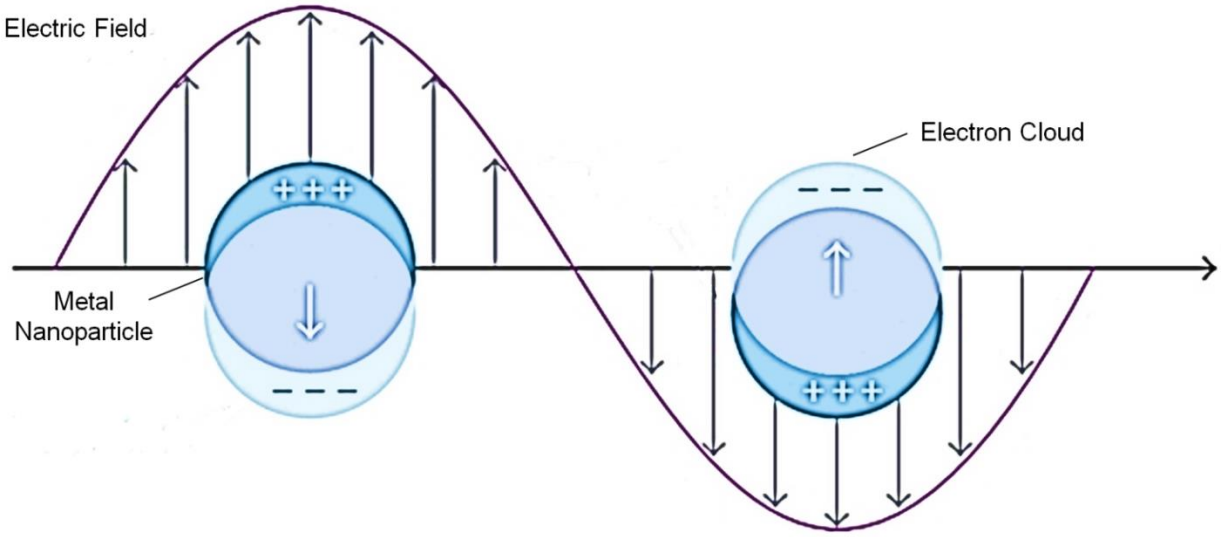

Figure 3.3: Example of a dipolar plasmon resonance that occurs when a metal nanoparticle is irradiated by a light source.

3.11). The metal particle's size, shape, dielectric properties, and proximity to other metal particles are critical to the magnitude of LSPR.[5]

SERS gains enhancement from an electromagnetic field that is in the vicinity of metallic objects and is best when the excitation wavelength is close to the electromagnetic resonances of the system.[5] It is possible to have an electric field at the molecule position (E_L) different from the incident field (E_i) with respect to both magnitude and orientation. Usually, the magnitude of $|E_L|$ is much larger than |E|. The local field induces a Raman dipole μ_R with the frequency ν_L as seen below:

$$\mu_R = \alpha_R E_L(\nu_L) \quad [3.6]$$

From this equation, it is deduced that the Raman dipole is enhanced by a factor of $|E_L(\nu_L)|/|E|$. If the Raman dipole radiates in free-space (i.e., in absence of metallic environment), the radiated energy (proportional to $|\mu R|^2$) would enhance by a factor of:

$$M_L(\nu_L) = \frac{|E_L(\nu_L)|^2}{|E|^2} \quad [3.7]$$

where $M_L(\nu_L)$ is the local field intensity enhancement factor (LFIEF) which is associated with the excitation of the Raman dipole. The LFIEF characterizes the enhancement of the electric field intensity, but ignores any changes in the electric field polarization.

3.3.2 Chemical Enhancement & Resonance Effects

Other effects that enhance in SERS include the chemical enhancement and resonance effects. When the molecule is adsorbed on the metal particle's surface contributions from the metal may greatly alter the magnitude, symmetry and resonant properties of the Raman polarizability of the molecule. Chemical enhancements are dependent on the strength of the interaction between the electronic structure of the molecule and that of the metal.[12]

In more detail, the chemical effect describes the adsorption of the analyte to the metal which results in the formation of stable metal-adsorbate complexes at the surface of the substrate. The complexes can stimulate a charge transfer interaction from the

Fermi-level of the metal to the lowest unoccupied molecular orbital of the analyte (LUMO).[5, 13] The transference of an electron from the highest occupied molecular orbital (HOMO) of the analyte to the Fermi level of the metal (retro-donation) is another process that can occur. In special cases, the adsorption of the analyte can also promote the resonant excitation of the electronic states of the analyte upon its interaction with the metal. Another process that can contribute to the CE of the Raman signal is called "dynamic charge transfer effect", where the incident photons promote the excitation of an electron of the analyte from its HOMO to its LUMO. Even though the CE enhancement factor is in the range of 10-10^3 cm^2 /molecule, the process always operates in conjunction with the electromagnetic enhancement of the Raman signal. Chemical effects are minor, but since the effects are multiplicative they can be important.

3.3.3 Parameters Influencing SERS EFs

Enhancement factors for SERS can be influenced by a multitude of parameters. Characteristics of the laser excitation, detection setup, the SERS substrate, intrinsic properties of the analyte, and the analyte's adsorption properties are all factors the affect the enhancement of the SERS signal.[5] The nature of the substrate environment also affects the SERS signal. This requires us to pay careful attention to the calculations associated with EFs (seen in Section 3.4).

3.4 Calculations of Enhancements

An intuitive approach to calculating an enhancement factor is to directly relate the Raman signal to the SERS signal using by the equation below:

$$EF = \frac{I_{SERS}/c_{SERS}}{I_{RS}/c_{RS}} \quad [3.8]$$

Where I is the intensity of either the SERS signal or the Raman signal (RS) and c is the concentration of each signal. All experimental conditions must be the same (i.e. laser wavelength, laser power, microscope lenses, spectrometer, etc.).[14] This definition falls short in describing the whole SERS EF because it strongly depends on the

adsorption properties (efficiency) of the probe, the analyte concentration (surface coverage), and type of SERS substrate. The concentration (c_{SERS}) does not define the number of adsorbed molecules, whereas the definition in Equation 3.9 accounts for Equation 3.8's shortcomings:

$$SERS\ Substrate\ EF = \frac{I_{SERS}/N_{SERS}}{I_{RS}/N_{RS}} \quad [3.9]$$

Where $N_{RS} = c_{RS} \cdot V$ is the average number of molecules in the scattering volume for the Raman measurement, and N_{SERS} is the number of adsorbed molecules in the same scattering volume for the SERS measurements. Equation 3.9 is considered as the best estimate of the average SERS EF for a monolayer on a SERS substrate. In many cases benzenethiol is used to determine the average SERS EF of the silver substrate used because it creates a well-defined monolayer with a surface coverage of 6.8×10^{14} molecules cm^{-2}.[15]

The $|E|^4$ approximation is derived from the more complicated equation of multiplying the local field enhancement (excitation) by the radiation enhancement (re-emission) to solve for single molecule EFs. Solving for the radiation enhancement (M_{Rad}) is a daunting task requiring an estimation to be formulated for simplicity. Generally, it is safe to assume that the radiation enhancement is roughly equal to the local field enhancement (M_L) at a specified frequency.[5] The single molecule EF can then be expressed as:

$$EF \approx M_L(\nu_L) M_{Rad}(\nu_R) \approx \frac{|E_L(\nu_L)|^2}{|E|^2} \frac{E_L(\nu_R)^2}{|E|^2} \quad [3.10]$$

In many cases the Raman shift is so small that an additional approximation is valid ($\nu_L \approx \nu_R$):

$$EF \approx \frac{|E_L(\nu_L)|^4}{|E|^4} \quad [3.11]$$

In many instances this approximation leads to the correct order of magnitude of the single molecule EF. The Average SERS EF can also be derived with this approximation

by surface averaging. It is important to note that average EFs are typically several orders of magnitude less that the single molecule EFs.

3.5 Surface Enhanced Substrates

The work performed in this dissertation includes planar metallic substrates. A SERS substrate generally refers to any metallic structure that generates a SERS enhancement. A SERS substrate should maximize the Raman enhancement, have little sample preparation, and be inexpensive, homongeneous, robust, reproducible and stable. Commonly used metals used for SERS are noble metals, such as copper, silver, and gold, because their surface plasmon resonances reside within the UV-NIR region.[16-18] Over the years, many different techniques have been developed to create a variety of SERS substrates which can be divided into two general classes, random and engineered.[19]

Traditional random morphology substrates include metal colloidal films[20-21] metal-island films on glass[22-24], electrochemically roughened silver electrodes[5, 25-26], and polymer nanoparticles surfaces (i.e. nanocomposites).[27-28] Metallic colloids have been used extensively in the literature; however, now dry colloids and other 2D planar substrates are used just as frequently.[10] Planar substrates are very easy to produce in the laboratory and are linked to the first possible observation of single-molecule SERS detection.[10] Colliods in solution (mostly in water for SERS) are stabilized by Coulombic repulsion from each particle. Colliods contain random aggregations that can lead to large enhancements (hot spots) but the enhancements do not represent the entire solution. The uniformity of colloids is poor due to random large enhancements of particular aggregations. Planar substrates, in comparison to metallic colloids, have a fixed geometry which affects the intensity of the analyte's spectrum and can reproducibly contain morphological uniformity.

Previously, the Sepaniak group has studied the SERS applications of polymer nanocomposites prepared by physical deposition of silver metal onto a pliable poly (dimethylsiloxane) (PDMS) polymer.[29-30] These nanocomposites offer unique

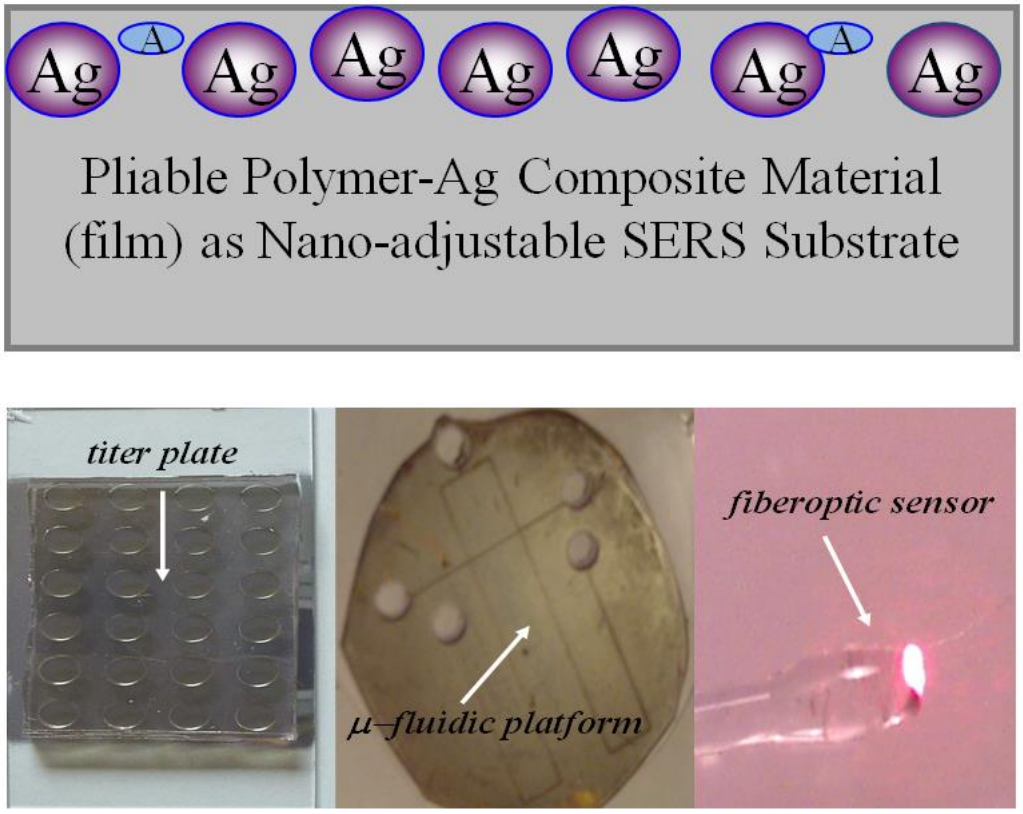

Figure 3.4: Metal-polymer nanocomposites with examples of PDMS molded into functional devices.

characteristics relative to other SERS substrates, including partial protection of the noble metal from oxidation (the metal is slightly submerged in the PDMS) and utilization of the PDMS material as an efficient solid phase extractor of analyte.[30] Silver substrates normally display the strongest SERS signals. One inherent issue with silver is that the silver particles are prone to oxidation upon contact to air, water, and other oxidizing agents. The oxidation property of silver limits the applications of silver SERS substrates for direct analysis of real samples. Moreover, the composites can be molded, manipulated, and conformally sealed to surfaces. Different examples of moldable PDMS substrates can be found in Figure 3.4. Despite the advantages of using nanocomposites, there are drawbacks to this substrate, most notably inhomogeneity in enhancement sites across the substrate and a limited effective surface area.

Besides random morphology produced SERS substrates, recent interest has been in engineered substrates. Using lithographic techniques, nanofabricated arrays have been produced and implemented as SERS substrates.[19, 30-34] Novel approaches to nano-sphere lithography or patterning through nano-lithography is currently being investigated.[5] Uniformity concerns arise from when two metal nano-particles, within close proximity, produce what is known to be a “hot spot”. A molecule in between two metallic nano-particles is subjected to high fields from localized surface plasmon resonance. The geometrical structure of a SERS substrate and the poly-dispersity of the particles play a role in how the plasmon resonances react, and how the EM enhancements increase the intensity by multiple orders of magnitude.[5, 10] Aggregates forming among metallic nano-particles are one of the uniformity issues that SERS faces. Much research has been dedicated to increasing homogeneity of the surface of the substrate and maximizing the strength of the induced electromagnetic field.

3.6 Relation to Dissertation

The purpose of the studies conducted in Chapter 5 was to develop a method in order to couple a chromatographic separation with surface enhanced Raman spectroscopy for detection. A pressurized device was fabricated to apply a constant pressure between a TLC plate and a silver-PDMS SERS substrate. After an optimized

pressure and time were found between the contact of the TLC plate and the SERS substrate, the silver SERS substrate (called silver nanocomposite) is interrogated with a Raman spectrometer. A separation is successfully transferred onto the silver nanocomposite and detected using surface enhanced Raman spectroscopy. This allowed for chemically specific detection, lower detection limits, and capabilities to couple nanocomposites with other highly efficient separation mediums.

3.7 References

1. Long, D. A., Classical Theory of Rayleigh and Raman Scattering. In *The Raman Effect*, John Wiley & Sons, Ltd: 2002; pp 31-48.
2. Smith, E.; Dent, G., The Raman Experiment – Raman Instrumentation, Sample Presentation, Data Handling and Practical Aspects of Interpretation. In *Modern Raman Spectroscopy – A Practical Approach*, John Wiley & Sons, Ltd: 2005; pp 23-70.
3. Lewis, I. R.; Edwards, H. G. M., Marcel Dekker, Inc. : New York, N.Y., 2001.
4. Skoog, D. A.; West, D. M.; Holler, F. J.; Crouch, S. R., 8th ed.; Brooks/Cole: India, 2004.
5. Le Ru, E. C.; Etchegoin, P. G., Chapter 2 - Raman spectroscopy and related optical techniques. In *Principles of Surface-Enhanced Raman Spectroscopy*, Ru, E. C. L.; Etchegoin, P. G., Eds. Elsevier: Amsterdam, 2009; pp 29-120.
6. Katrin, K.; Harald, K.; Irving, I.; Ramachandra, R. D.; Michael, S. F., *Journal of Physics: Condensed Matter* **2002,** *14* (18), R597.
7. LaPlant, F.; Ben-Amotz, D., *Review of Scientific Instruments* **1995,** *66* (6), 3537-3544.
8. Le Ru, E. C.; Etchegoin, P. G., Chapter 1 - A quick overview of surface-enhanced Raman spectroscopy. In *Principles of Surface-Enhanced Raman Spectroscopy*, Ru, E. C. L.; Etchegoin, P. G., Eds. Elsevier: Amsterdam, 2009; pp 1-27.
9. Fleischman, M.; Hendra, P. J.; McQuillan, A. J., *Chem. Phys. Lett.* **1974,** *26* (123).
10. Kneipp, K.; Moskovits, M.; Kneipp, H., 1 ed.; Springer-Verlag Berlin Heidelberg: 2006; Vol. 103, p 466.
11. Moskovits, M., *Rev. Mod. Phys.* **1985,** *57*, 783.
12. Schlücker, S., *Angewandte Chemie International Edition* **2014,** *53* (19), 4756-4795.
13. Visible Ruled Reflective Diffraction gratings https://www.thorlabs.de/newgrouppage9.cfm?objectgroup_id=8626.
14. Le Ru, E. C.; Blackie, E.; Meyer, M.; Etchegoin, P. G., *The Journal of Physical Chemistry C* **2007,** *111* (37), 13794-13803.
15. Whelan, C. M.; Smyth, M. R.; Barnes, C. J., *Langmuir* **1999,** *15*, 116-126.
16. De Jesus, M. A. Development of Novel Substrates and Sampling Techniques for the Analysis of Drugs and Model Environmental Pollutants via Surface Enhanced Raman Spectroscopy (SERS). Ph.D. Dissertation, University of Tennessee-Knoxville, Knoxville, TN, 2004.
17. Weitz, D. A.; Oliveria, M., *Phys. Rev. Letters* **1984,** *52* (16), 1433-1436.
18. Yamaguchi, Y.; Weldon, M. K.; Morris, M. D., *App. Spec.* **1999,** *53* (2), 127-132.
19. Wells, S. M.; Polemi, A.; Lavrik, N. V.; Shuford, K. L.; Sepaniak, M. J., *Chem. Commun.* **2011,** *47*, 3814.
20. Musick, M. D.; Keating, C. D.; Lyon, L. A.; Botsko, S. L.; Pena, D. J.; Hollay, W. D.; McEvoy, T. M.; Richardson, J. N.; Natan, M. J., *Chem. Mater.* **2000,** *12*, 2869.
21. Park, S. H.; Im, J. H.; Im, J. W.; Chun, B. H.; Kim, J. H., *Microchem. J.* **1999,** *63*, 71.
22. Lacy, W. B.; Olson, L. G.; Harris, J. M., *Anal. Chem.* **1999,** *71*, 2564.
23. Mulvaney, S. P.; He, L.; Natan, M. J.; Keating, C. D., *J. Raman Spectrosc.* **2003,** *34*, 163.
24. Reilly, T. H.; Corbman, J. D.; Rowlen, K. L., *Anal. Chem.* **2007,** *79*, 5078.
25. Li, J.; Fang, Y., *Spectrochim. Acta, Part A* **2007,** *66A*, 994.

26. Murgida, D.; Hildebrandt, P., *Top. Appl. Phys.* **2006,** *103*, 313.
27. Pristinski, D.; Tan, S.; Erol, M.; Du, H.; Sukhishvili, S., *J. Raman Spectrosc.* **2006,** *37*, 762.
28. Qian, X. M.; Ansari, D.; Nie, S., *Proc. SPIE* **2007,** *6448*, 1.
29. De Jesus, M. A.; Giesfeldt, K. S.; Sepaniak, M. J., *J. Raman Spectrosc.* **2004,** *35* (10), 895.
30. Oran, J. M.; Hinde, R. J.; Abu Hatab, N.; Sepaniak, M. J., *J. Raman Spectrosc.* **2008,** *39*, 1811.
31. Bhandari, D.; Kravchenko, I. I.; Lavrik, N. V.; Sepaniak, M. J., *J. Am. Chem. Soc.* **2011,** *133*, 7722.
32. Green, M.; Liu, F. M., *J. Phys. Chem. B* **2003,** *107*, 13015.
33. Yan, B.; Thubagere, A.; Premasiri, W. R.; Ziegler, L. D.; Dal Negro, L.; Reinhard, B. M., *ACS Nano* **2009,** *3*, 1190.
34. Haynes, L. C.; Van Duyne, R. P., *J. Phys. Chem. B* **2003,** *107*, 7426.

Chapter 4

Introduction to Magneto-Elastic Wire

4.1 Introduction to Magnetization

Traditionally magnetism has been viewed as an interaction between magnetic poles (p_1 and p_2) that are separated by a given distance (r) and can be viewed as analogous to the Coulomb interaction between electrically charged particles[1]:

$$F = \frac{p_1 p_2}{4\pi\mu_0 r^2} \quad [4.1]$$

where F is the force acting on a magnetic pole and μ_0 is the permeability of the vacuum. From an electrical standpoint, it can also be stated that a magnetic field producing an electric current or another magnetic pole, exerts a force on the initial magnetic pole strength.

$$F\ (or\ \boldsymbol{H}) = p\boldsymbol{H}_0 \quad [4.2]$$

where H_0 is the applied magnetic field due to the electric current and p is the magnetic pole strength. Equation 4.2 implies that if a magnetic material is brought near a magnet a magnetic field of the magnet ultimately magnetizes the material. The F (commonly denoted as **H** for electronic applications) in this equation is regarded as the magnetizing force or magnetic field intensity.[1]

There are four main types of magnetic ordering which can be seen schematically in Figure 4.1. Paramagnets contain individual atoms or ions that have magnetic moments, but the moments are disordered, so no net magnetization is observed. Antiferromagnets have magnetic moments on the individual atoms or ions that align in an antiparallel fashion, which also leads to a net zero-field magnetization. With ferromagnets the moments align parallel to each other, yielding a large net magnetization. Ferrimagnets are microscopically similar to antiferromagnets in regards to consisting of two sublattices within which the moments are aligned parallel, with the two sublattices aligned antiparallel to each other. The main difference between these two orderings is that the magnitudes of the magnetic moments in the two sublattices are different, so a net magnetization does occur.[2] The sensor used in Chapter 7 is uses a ferromagnetic wire due to a large magnetization properties allowing for easy detection.

When ferromagnetic materials are magnetized in one direction, they do not relax back to zero magnetization when the imposed magnetizing field is removed. The ferromagnetic materials must be driven back to zero by a field in the opposite direction. In the case of an alternating magnetic field that is applied to the material, the magnetization will trace out a loop called a hysteresis loop. Hysteresis is a property of ferromagnetic materials defined as a lack of re-traceability of the magnetization curve and it is related to the existence of magnetic domains in the material.[1-2] When magnetic domains are reoriented, it takes some energy to turn them back to their original state. A common hysteresis curve can be seen in Figure 4.1 in a common magnetic flux versus magnetic field intensity graph.

A useful property of ferromagnets is that they have a magnetic memory based on their specific hysteresis loops. When ferromagnetic materials retain their magnetism even after the removal of the applied magnetic field they are defined as hard magnetic materials or more commonly as permanent magnets. On the other hand, soft magnetic materials are easy to magnetize and demagnetize and are homogenous in nature.[2] Soft magnetic materials were absolutely necessary for the sensor developed in Chapter 7 in order to obtain a low limit of detection. A minute change in magnetization of the ferromagnetic wire was necessary in order to detect low concentrations of the gas analytes tested.

4.2 Introduction to Ferromagnetic Amorphous Wire

Recent advances in magnetic sensors have stimulated development of magnetic materials to exhibit outstanding magnetic characteristics with reduced dimensions.[3] Ferromagnetic amorphous alloys are one of the softest magnetic materials used for applications in technology.[4] The most common form of ferromagnetic amorphous alloys is a ribbon shape fabricated by melt-spinning techniques. Within the last few years, interest in ferromagnetic amorphous thin wires with dimensions on the order of 1-30 μm in diameter have become a popular area of study.[5-8] Progress has been achieved in the fabrication of magnetic nano-materials but normally at a high cost with sophisticated

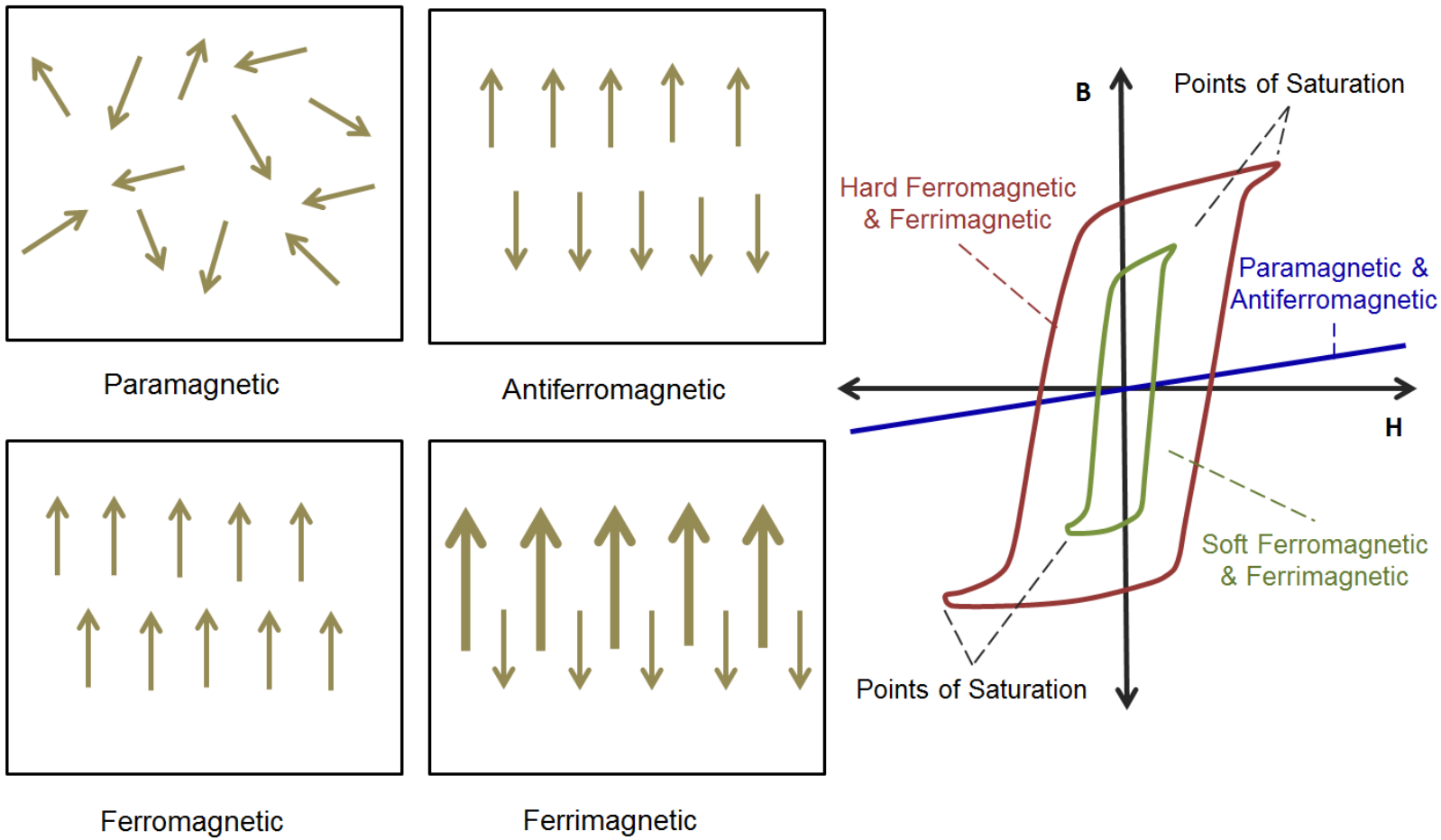

Figure 4.1: Ordering of magnetic dipole moments in the four main types of magnetic materials, and the resulting magnetization versus magnetic field intensity curves.

technology, and poorer quality than the bulk material (i.e. amorphous ribbons).[5-6] The attractive features of these wires include the soft magnetic properties, magneto-transport properties, and an unusal re-magnetization process giving a magnetically bistable material.[6-10] Further details and definitions of these properties can be found in Section 4.3.

The first amorphous metallic material produced was metallic glass by rapid quenching from a liquid state by Miroshnitchenko and Salli and later by Duwez et al.[11-12] Since that material discovery, new research was conducted fabricating novel amorphous materials such as metastable crystalline phases and structures and extended solid solubilites of solutes with improved mechanical and physical properties.[11-12] In the 1960s and 1970s further development in field included advancements in fabrication techniques, structural characterization, studies of thermodynamics and physical properties.[13-14] In 1988, Yoshizawa et al. introduced an annealing procedure that induced nanocrystallinity (ultrafine grain structure) in an amorphous alloy, which improves the magnetically soft behavior of the alloy.[15] This discovery leads to a boom of research and technological interest in nanocrystalline alloys that were Fe-rich due to the extremely soft magnetic properties and high saturation magnetization. Nanocrystalline structures of amorphous materials are observed in Fe-Si-B with small additions of Cu and Nb to decrease the grain (crystal) growth rate.[16-17] The 1990s started era of the amorphous magnetic wire.[18-19] The first generation of this wire contains typical diameters of 125 μm obtained by the in-rotating-water quenching technique described in Section 4.4. One of the last improvements to the nanocrystalline amorphous wire included miniaturization. An alternative technology of rapid quenching was produced by Taylor and Ulitovski that produced thinner metallic wires from 1 to 30 μm in diameter.[6-9] The small diameter wire is then covered by an insulating glass coating that has been widely used for fabrication of ferromagnetic materials.

4.3 Ferromagnetic Amorphous Wire Properties

Amorphous magnetic materials exhibit extremely soft magnetic behavior due to the absence of magnetocrystalline anisotropy, grain boundaries, and crystalline structure defects. Soft magnetic behavior refers to materials that have a low coercivity or, in other words, their magnetization is easy to change.[3] Magnetocrystalline anisotropy refers to a ferromagnetic material that takes more energy to magnetize it in a certain direction than in others. The magnetic moment of magnetically anisotropic materials will tend to align in the direction of the axis that is energetically favorable of spontaneous magnetization.[20] The direction of the axis is usually related to the principal axis of the crystal lattice. Grain boundaries occur in crystalline solids where millions of grains (single crystals) are separated from one another; each separation is considered a boundary. Each individual crystal has a systematic packing of atoms and, therefore, a different orientation from a neighboring crystal. Within a crystalline material there can be millions of disorientations between grains.[20] Amorphous magnetic materials have a large advantage over other magnetic materials due to their lack of the above mentioned properties.

The ferromagnetic amorphous wire used in this dissertation is considered a form of the magnetoelastic anisotropy type. Magnetoelastic anisotropy is the change of magnetic susceptibility of a material when subjected to a mechanical stress. More precisely, magnetoelastic anisotropy refers to the observation that magneto-elastic effects (i.e. magnetostriction) are anisotropic in some materials. The work in Chapter 7 is performed based on the magnetoelastic behavior of the ferromagnetic wire we chose for the ChIMES (Chemical Identification through Magneto-Elastic Sensing) sensor. Briefly, the wire is coated with a target response material that swells when introduced to a volatile organic compound which applies stress on the wire. The stress is measured by the change in magnetization of the wire. Magnetostriction is another related property of ferromagnetic materials that describes the change in shape or dimensions during the process of magnetization. There is a variation of a materials magnetization due to an applied magnetic field that causes the magnetostrictive strain until it reaches a maximum value (saturation value).[20] Low values of the saturation magnetostriction are

essential to avoid magnetoelastic anisotropies arising from internal or external mechanical stresses.[3] In essence, the magnetostrictive strain due to an applied magnetic field must not surpass a maximum value or physical axial stresses are measured rather than strain due to the change in magnetization.

The most attractive magnetic property of the amorphous wire to explain in detail is the peculiar magnetization process that leads to a single and large Barkhausen jump between two stable remanent states giving macroscopic squared hysteresis loops.[18] Traditionally, the Barkhausen effect is the succession of abrupt changes in magnetization occurring when the magnetizing force acting on a ferromagnet is varied. Heinrich Barkhausen discovered that a slow, smooth increase of a magnetic field applied to a ferromagnetic material causes it to become magnetized in minute steps instead of continuously.[19, 21] Figure 4.2 shows a simple plot of magnetization vs magnetic field intensity and an example of the Barkhausen jumps. From a chemical perspective, ferromagnetic materials are characterized by the presence of microscopic domains (10^{12} to 10^{15} atoms) where the magnetic moments of the spinning electrons are all parallel. When unmagnetized, there is random orientation of domains but when a magnetic field is applied the domains turn into an orientation parallel to the field or increase in size. During the steep part of the magnetization curve, whole domains suddenly change in size or orientation causing the discontinuous increase in the magnetization.[21]

As a result of a large Barkhausen jump, a rectangular hysteresis loop can be seen when there is a low magnetic field. Amorphous alloys show rectangular hysteresis loops due to the magnetoelastic anisotropy contribution that results from the stress induced during the rapid quenching process described in Section 4.4. It is important to note that the rectangular hysteresis loop disappears when the magnetic field is below some critical value. The overall shape of hysteresis loops of amorphous microwires depends on the composition of the metallic nucleus as well as on the thickness of glass coating if the wire has been coated. The metallic nucleus composition (Fe, Co, Co-Fe) effect on magnetic properties and hysteresis loop shape can be seen in Figure 4.3. The microwire used in the sensor developed in Chapter 7 is similar to graph c in Figure 4.3

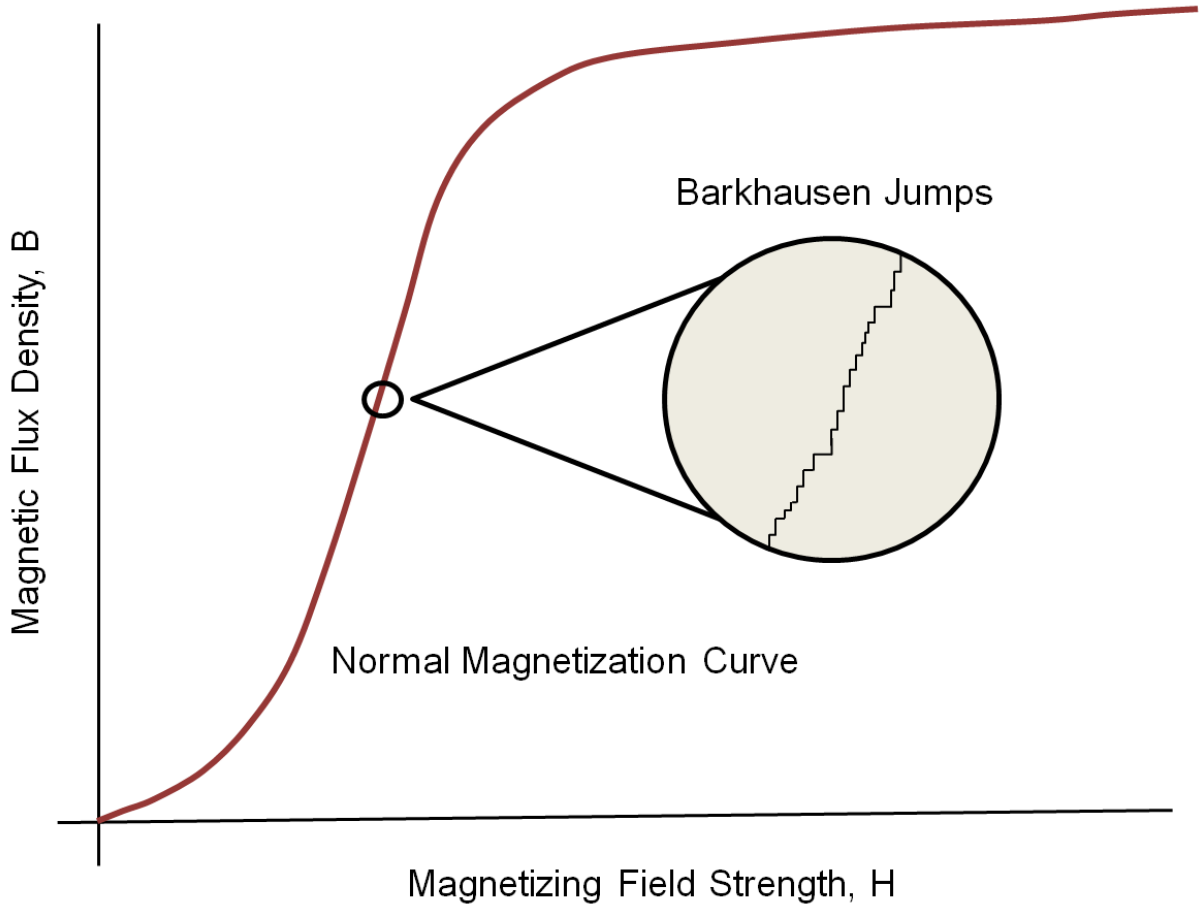

Figure 4.2: Magnetizing field strength versus magnetic flux density of a ferromagnetic material illustrating the Barkhausen effect in the magnified section of the plot.

due to the composition of the metallic nucleus of the SENCY wire fabricated by Unitika, Ltd., of Japan. The SENCY wire has a near zero magnetostriction yielding a less rectangular hysteresis loop as commonly seen with the typical magnetostriction ferromagnetic amorphous wires.

4.4 Fabrication of Wire

Specifically, the wire used in the ChIMES sensor is considered free-flight melt-spinning in a liquid environment. Engelke reported the first method of metallic filaments being prepared by ejecting molten metal through a fine orifice into a compatible liquid medium that flows with the molten metal stream.[22] The containment liquid is pumped through a tube surrounding the ejection nozzle with stable, laminar liquid flow. By manipulating the size of the orifice and the rate of flow surrounding the liquid, the diameter of the filament produced is between ~25 µm to 3 mm.

Kavesh developed a related technique where molten material is ejected through an orifice into a liquid medium which flows with the molten stream.[22] The molten metal or alloy is contained in a fused silica or zirconia crucible that comprises one or more orifices that are 20 to 600 µm in diameter. The molten material is ejected by using gas pressure across a small air gap into a circulating quenching medium. At this point, the molten material solidifies to produce filament that obtains a circular cross-section. The quenching medium is typically water or an aqueous chloride solution. Filaments can have diameters down to ~20 µm.

The ChIMES sensor used a ferromagnetic amorphous microwire that was fabricated using a melt-spinning technique developed by Ohnaka et al.[23] The melt-spinning technique is where a molten alloy is ejected though a fine nozzle into a water layer held, by centrifugal force, on the inner surface of a rotating drum. The technique is illustrated in Figure 4.4. The diameter of the wire acquired is mostly a function of the diameter of the ejection orifice. The angle of incidence of the jet stream to the water surface determines the shape of the wire cross-section. A small incidence angle yields a circular cross-section whereas larger angles yield elliptical fibers. This method has successfully produced microcrystalline and amorphous wires with diameters down to ~80 µm. The

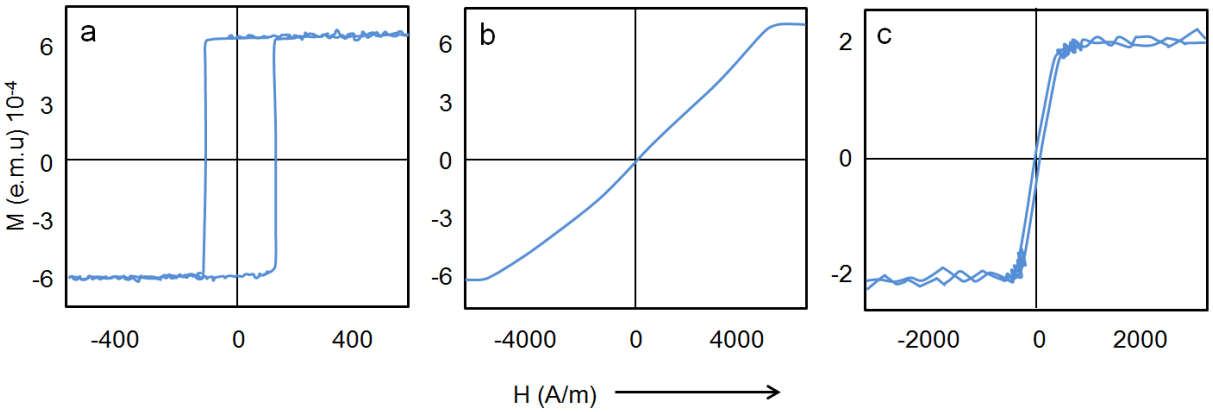

Figure 4.3: Hysteresis loops of (a) Fe-rich, (b) Co-rich, (c) Co-Fe-rich microwires. Graph c represents the type of hysteresis loop corresponding to the microwire used in Chapter 7.

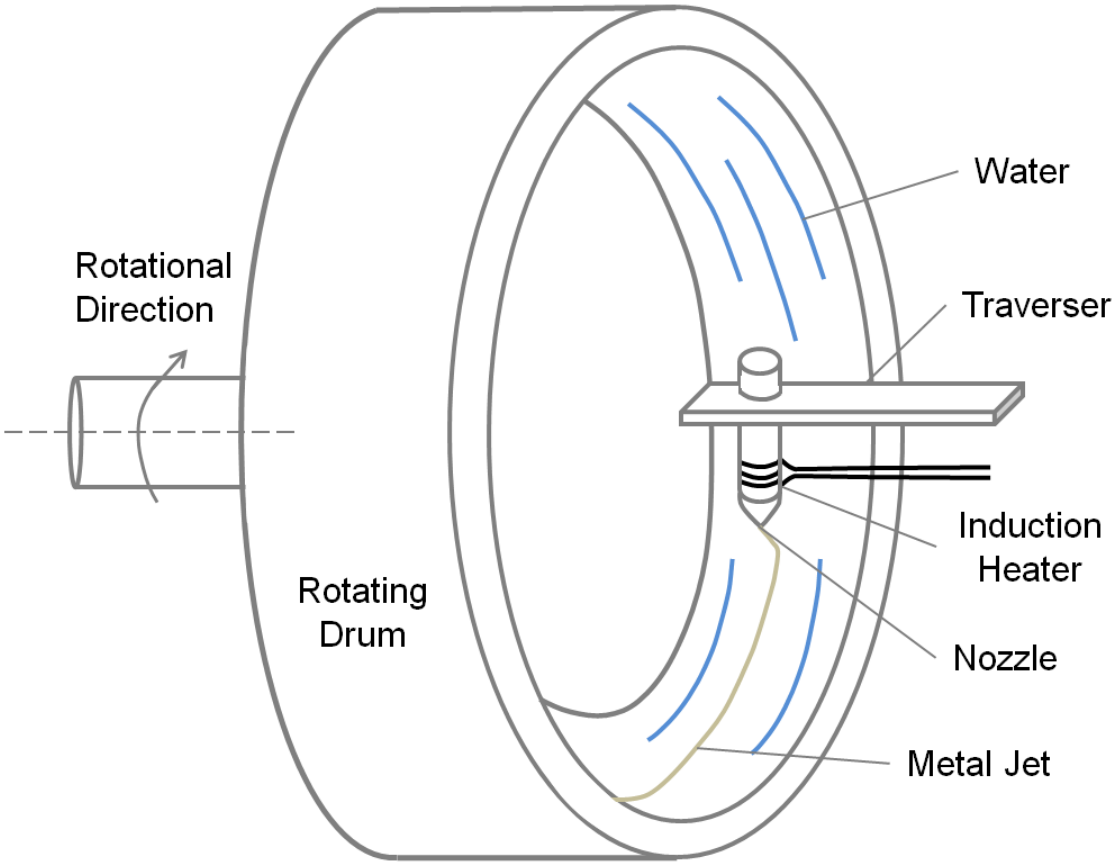

Figure 4.4: Illustration of the melt-spinning technique used to fabricate the ferromagnetic amorphous microwires used in the ChIMES sensors developed by Ohnaka.

wires used for the ChIMES sensor were 80 to 110 µm with the 100 µm diameter being the most common.

4.5 Sensing Mechanism of Amorphous Ferromagnetic Foils

The first amorphous ferromagnetic magnetoelastic sensors were developed from ribbon-like thick-film strip alloys. They are the size of 4 cm long x 6 mm wide x 25 µm thick and commonly used as anti-theft markers.[24] Longitudinal vibrations are produced within these sensors when exposed to a time-varying magnetic field, which generates elastic waves.[25] The elastic waves in a magneoelastic material create a magnetic flux that is detected remotely. The sensor response can be detected by magnetic, acoustic or optical techniques.

The frequency and amplitude of the longitudinal vibrations of a sensor can be described by the equation below,[26]

$$f = \frac{1}{2L}\sqrt{\frac{E'}{\rho}} \qquad [4.5]$$

where the sensor response depends on length L, elasticity E', and the density ρ. When there is a small mass loading on the surface of the sensor the resonant frequency changes according to the equation:

$$\Delta f = -f_0 \frac{\Delta m}{2m_0} \qquad [4.6]$$

Where the magnetoelastic sensor has a mass m_0 with an initial resonant frequency f_0, when subjected to a mass loading of Δm. A relationship between the change in resonant frequency to that of viscosity and density of the medium surrounding a sensor is seen in Equation 4.7.[27]

$$\Delta f = \frac{\sqrt{\pi f_0}}{2\pi\rho_s d_{ME}}\sqrt{\eta\rho_l} \qquad [4.7]$$

Where η is viscosity, ρ_l is the density of the surrounding medium, d_{ME} is the thickness of the magnetoelastic sensor, and ρ_s is the density of the sensor. The three main

equations above describe the resonance changes in a magnetoelastic sensor due to the changes in the surrounding medium, which provide the basis of the sensing mechanism of previous sensor applications using amorphous ribbon (Foil). The principle detection method in ChIMES is based on the stress-induced changes in the magnetic permeability of the wire, which is explained in more detail in Chapter 7. The sensing method used in Chapter 7 is the first use of measuring the change in the magnetic permeability due to an applied stress of an amorphous wire.

4.6 Amorphous Ferromagnetic Foil Sensor Applications

Unlike amorphous ferromagnetic wires, the foils have been used for a wide variety of applications due to the ability of the magnetoelastic sensor to respond to changes at ambient conditions. Magnetoelastic foil sensors have been used in applications involving detection and measurement of physical parameters such as pressure[28-30], temperature[31-33], liquid density and viscosity[26, 34-36], fluid flow velocity[29, 35], and elastic modulus of thin films[37-38]. Chemical sensing through magnetoelastic foils has been explored in which a thin, chemically sensitive over-layer is applied onto the foil. The mass of the over-layer changes upon interaction with a chemically active ambient that causes a shift in sensor resonance properties. Some examples of chemical sensing with foils includes gas-phase sensing of humidity[29, 31, 39], carbon dioxide[40], and ammonia[41]. Liquid-phase sensing of magnetoelastic sensors has been used to measure solution pH[32, 42], and sometimes involve chemical-biological agents such as glucose, avidin, ricin, endotoxin B, and E. coli 0157:H7[43-47]. Wireless capabilities of magnetoelastic sensors allows for a large variety of applications. Amorphous ferromagnetic wires have not been as widely studied in the field of chemical sensors.

4.7 Relation to Dissertation

In Chapter 7, a chemical sensor using amorphous ferromagnetic microwires is described. The mechanism and properties of the wire briefly discussed in this chapter apply to the ChIMES sensor. The microwire is mated coaxially with a target response material (TRM) that is chemically composed of a polymer or a polymer-molecular additive. A gas phase, volatile organic compound (VOC), is introduced to a flow cell that

contains one sensor or an array of sensors with different TRMs. Each sensor (same microwire different TRM) responds differentially to the VOC introduced. The degree to which each coated TRM swells is different with each gas passing through the flow cell. When a TRM swells it applies a stress on the wire, which can be magnetically monitored by the coil set described in Chapter 7. Four different TRMs are studied along with eight different VOCs. Optimization studies and calibration studies were the focus of my work associated with the project.

4.7 References

1. Stefanita, C.-G., 1 ed.; Springer-Verlag Berlin Heidelberg: Berlin Heidelberg, 2012.
2. Spaldin, N. A., Cambridge University Press: Cambridge, GBR, 2010.
3. Zhukova, V.; Ipatov, M.; Zhukov, A., *Sensors* **2009,** *9*, 9216-9240.
4. Vazquez, M.; Hernando, A., *J. Phys. D: Appl. Phys.* **1996,** *29*, 939-949.
5. Jiles, D. C., *Acta. Mater.* **2003,** *51*, 5907-5939.
6. Zhukov, A.; González, J.; Vázquez, M.; Larin, V.; Torcunov, A., Nanocrystalline and amorphous magnetic microwires. In *Encyclopedia of Nanoscience and Nanotechnology*, American Scientific Publishers: Valencia, CA, USA, 2004; Vol. 6, pp 365-387.
7. Zhukov, A.; Ipatov, M.; Zhukova, V.; García, C.; Gonzalez, J.; Blanco, J. M., *Phys. Stat. Sol. A* **2008,** *205*, 1367-1372.
8. Garcia Prieto, M. J.; Pina, E.; Zhukov, A. P.; Larin, V.; Marin, P.; Vázquez, M.; Hernando, A., *Sens. Actuators, A* **2000,** *81*, 227-231.
9. Varga, R.; Zhukov, A.; Zhukova, V.; Blanco, J. M.; Gonzalez, J., *Phys. Rev. B* **2007,** *76*, 132406:1–132406:3.
10. Chiriac, H.; Ovari, T. A., *Progr. Mater. Sci.* **1996,** *40*, 333-407.
11. Miroshnichenko, I. S.; Salli, I. V., *Ind. Lab.* **1959,** *25*, 1463-1466.
12. Duwez, P.; Williams, R. J.; Klement, K., *J. Appl. Phys.* **1966,** *31*, 1136-1142.
13. Duwez, P., Pergamon: New York, NY, USA, 1966; Vol. 3.
14. Luborsky, F. E., Butterworth and Co. : London, UK, 1983.
15. Yoshizawa, Y.; Oguma, S.; Yamauchi, K., *J. Appl. Phys.* **1988,** *64*, 6044-6046.
16. Herzer, G., *IEEE Trans. Magn.* **1990,** *26*, 1397-1402.
17. Hernando, A.; Vázquez, M., CRC: Boca Raton, FL, USA, 1993.
18. Humphrey, F. B.; Mohri, K.; Yamasaki, J.; Kawamura, H.; Malmhäll, R.; Ogasawara, I., Elsevier Science: Amsterdam, the Netherlands, 1987.
19. Mohri, K.; Humphrey, F. B.; Kawashima, K.; Kimura, K.; Muzutani, M., *IEEE Trans. Magn.* **1990,** *26*, 1789-1791.
20. Aharoni, A., Oxford University Press, USA: 1996.
21. Barkhausen Jump. In *McGraw-Hill Concise Encyclopedia of Physics*, The McGraw-Hill Companies, Inc: 2002.
22. Donald, I. W., *Journal of Material Science* **1987,** *22*, 2661-2679.
23. Ohnaka, I.; Fukusako, T.; Ohmichi, J., *J. Jpn. Inst. Met.* **1981,** *45* (7).
24. Grimes, C. A.; Roy, S. C.; Rani, S.; Cai, Q., *Sensors* **2011,** *11*, 2809-2844.
25. du Tremolet de Lacheisserie, E., *J. Magn. Magn. Mater.* **1982,** *25*, 251-270.
26. Landau, L. D.; Lifshitz, E. M., 3rd ed ed.; Pergamon Press: New York, NY, USA, 1986.
27. Stoyanov, P. G.; Grimes, C. A., *Sens. Actuat. B Chem.* **2000,** *80*, 8-14.
28. Grimes, C. A.; Stoyanov, P. G.; Kouzoudis, D.; Ong, K. G., *Rev. Sci. Instrum.* **1999,** *70*, 4711-4714.
29. Grimes, C. A.; Kouzoudis, D., *Sens. Actuat. A Phys.* **2000,** *84*, 205-212.
30. Kouzoudis, D.; Grimes, C. A., *Smart Mater. Struct.* **2000,** *9*, 885-889.
31. Jain, M. K.; Schmidt, S.; Ong, K. G.; Mungle, C.; Grimes, C. A., *Smart Mater. Struct.* **2000,** *2000* (502-510).
32. Jain, M. K.; Cai, Q. Y.; Grimes, C. A., *Smart Mater. Struct.* **2001,** *10*, 347-353.
33. Jain, M. K.; Grimes, C. A., *IEEE Trans. Magn.* **2001,** *37*, 2022-2024.
34. Loiselle, K. T.; Grimes, C. A., *Rev. Sci. Instrum.* **2000,** *71*, 1441-1446.

35. Jain, M. K.; Schmidt, S.; Mungle, C.; Loiselle, K.; Grimes, C. A., *IEEE Trans. Magn.* **2001,** *37*, 2767-2769.
36. Grimes, C. A.; Kouzoudis, D.; Mungle, C., *Rev. Sci. Instrum.* **2000,** *71*, 3822-3824.
37. Schmidt, S.; Grimes, C. A., *Sens. Actuat. A Phys.* **2001,** *94*, 189-196.
38. Schmidt, S.; Grimes, C. A., *IEEE Trans. Magn.* **2001,** *37*, 2731-2733.
39. Grimes, C. A.; Kouzoudis, D.; Dickey, E. C.; Qian, D.; Anderson, M. A.; Shahidain, R.; Lindsey, M.; Green, L., *J. Appl. Phys.* **2000,** *87*, 5341-5343.
40. Cai, Q. Y.; Cammers-Goodwin, A.; Grimes, C. A., *J. Environ. Monit.* **2000,** *2*, 556-560.
41. Cai, Q. Y.; Jain, M. K.; Grimes, C. A., *Sens. Actuat. B Chem.* **2001,** *77*.
42. Cai, Q. Y.; Grimes, C. A., *Sens. Actuat. B Chem.* **2000,** *71*, 112-117.
43. Cai, Q. Y.; Zeng, K. F.; Ruan, C. M.; T.A., D.; Grimes, C. A., *Anal. Chem.* **2004,** *76*, 4038-4043.
44. Ruan, C. M.; Zeng, K. F.; Varghese, O. K.; Grimes, C. A., *Biosens. Bioelect.* **2004,** *19*, 1695-1701.
45. Ruan, C. M.; Varghese, O. K.; Grimes, C. A.; Zeng, K. F.; Yang, X. P.; Mukherjee, N.; Ong, K. G., *Sens. Lett.* **2004,** *2*, 138-144.
46. Ruan, C. M.; Zeng, K. F.; Varghese, O. K.; Grimes, C. A., *Biosens. Bioelect.* **2004,** *2*, 138-144.
47. Ruan, C. M.; Zeng, K. F.; Varghese, O. K.; Grimes, C. A., *Anal. Chem.* **2003,** *75*, 6494-6498.

Chapter 5

Surface Enhanced Raman Scattering (SERS) Imaging of Developed Thin-Layer Chromatography (TLC) Plates

Chapter 5 is an adaption of a research article in Analytical Chemistry, 2013, 85(8), 3991-3998. The article describes a separation of a three component mixture on a TLC plate where the separation is transferred onto a Ag-PDMS substrate and the substrate is then subjected to surface enhanced Raman spectroscopy.

5.1 Abstract

A method for hyphenating surface enhanced Raman scattering (SERS) and thin-layer chromatography (TLC) is presented that employs silver-polymer nanocomposites as an interface. Through the process of conformal blotting, analytes are transferred from TLC plates to nanocomposite films before being imaged via SERS. A procedure leading to maximum blotting efficiency was established by investigating various parameters such as time, pressure, and type and amount of blotting solvent. Additionally, limits of detection were established for test analytes malachite green isothiocyanate, 4-aminothiophenol, and Rhodamine 6G (Rh6G) ranging from 10^{-7} to 10^{-6} M. Band broadening due to blotting was minimal (~ 10%) as examined by comparing the spatial extent of TLC-spotted Rh6G via fluorescence and then the SERS-based spot size on the nanocomposite after the blotting process. Finally, a separation of the test analytes was carried out on a TLC plate followed by blotting and the acquisition of distance x wavenumber x intensity 3-D TLC-SERS plots.

5.2 Introduction

Thin-layer chromatography (TLC) is a well-established separation technique with a rich history. Poole and others have written informative reviews on the technique and its evolution.[1-5] In its simplest form, a sample is spotted via a syringe onto a planar-oriented thin layer of stationary phase (typically silica gel) and allowed to dry. The plate is then developed by allowing the mobile phase to travel along the TLC plate via capillary action. Components of the mixture will move at different rates along the TLC plate based on their differential affinity for the stationary and mobile phases leading to a spatial distribution of the individual component spots. Despite the desirability of simplicity, many modernizing advances in TLC have occurred including reduction in

particle size (high performance versions, i.e., HPTLC), over-pressure and electrokinetically-driven development, and ultra-thin stationary phase layers to mention a few.[1-5] Among the advantages of TLC is its 2-dimensional nature, which allows for sample multiplexing or true 2-D development with orthogonal separation modes in each dimension to increase the peak capacity (which is otherwise limited by the modest plate heights of the technique).

Detection is often based on absorbance or fluorescence; native of the separated components or enhanced via post separation reaction with visualizing agents. In some cases plates are covered with inorganic fluorophors to facilitate detection by spot related fluorescence attenuation.[3-5] The developed TLC plate effectively stores the separation profile with the detection process benefiting from its static nature. Although some qualitative information resides in retardation factors (R_f) of the detected spots, component identification based on R_f is not reliable. However, TLC can be coupled with spectrometric methods such as infrared, Raman, and mass spectrometry for compound specific information. Imaging detection using information rich techniques is a burgeoning area of research in planar chromatography.[6-12] In some instances, including the work described herein, separated spots are moved from the TLC plate to a detection-compatible planar medium using a blotting process. In particular, blotting has been used effectively with mass spectrometry and GC-MS.[12-14]

Surface enhanced Raman spectroscopy (SERS) is a highly sensitive means of detection for both chemical and biological species.[15] Enhancement of the Raman signal occurs when analytes are adsorbed or in very close vicinity to nanostructured, morphologically-optimized, noble metal surfaces.[16] The principle mechanism responsible for the enhancement of the Raman signal is based on an electromagnetic effect in which the field at or near the laser irradiated metal nanoparticle surface is enhanced through the development of localized surface plasmons.[17.18] Additionally, other signal enhancement can be brought about by chemical and resonance effects.[19] Under ideal conditions, these composite mechanisms can result in enhancements large enough for single molecule detection.[20-23]

Over the years, many different techniques have been developed to create a variety of SERS substrates which can be divided into two general classes, random and engineered.[24] Random substrates include metal colloidal films,[25,26] metal-island films on glass,[27-29] electrochemically roughened silver electrodes,[30,31] or polymer nanoparticles surfaces (i.e. nanocomposites).[32,33] Besides the aforementioned substrates that have random morphology, recent interest has been directed at engineered substrates with deterministic morphology. Specifically using lithographic techniques, nanofabricated arrays have been produced and implemented as SERS substrates.[34-39] Previously, our group has studied the SERS applications of random morphology polymer nanocomposites prepared by physical deposition of silver metal onto a pliable polydimethylsiloxane (PDMS) polymer.[40,41] As stated in chapter 3, these nanocomposites offer unique characteristics relative to other SERS substrates, including partial protection of the noble metal from oxidation (the metal is slightly submerged in the PDMS) and utilization of the PDMS material as an efficient solid phase extractor of analyte.[41] Moreover, the composites can be molded, manipulated and, relevant herein, conformally sealed to surfaces. The drawbacks to this substrate include inhomogeneity in enhancement sites across the substrate and a limited effective surface area. In order to overcome any inhomogeneous features on the substrate; an averaging technique was used by translating the substrate back and forth a distance of 500 µm while acquiring the signal.[42]

5.3 Coupling of TLC-SERS

The coupling of thin layer chromatography and surface enhanced Raman spectroscopy (TLC-SERS) is a relatively unexplored area of separation and detection. In the late 1980's, the first report of TLC-SERS emerged.[43] After separation of the analytes on a TLC plate, silver colloid was applied through an atomized spray providing a platform for SERS imaging. This approach has also been implemented on different chemical species such as amino acids,[8] pharmaceuticals,[10] and for analysis of historical artifacts.[11] Although the atomized colloid approach provides a means of detection for TLC, there are inherent drawbacks to this system. Although the silica does not provide

significant background to the SERS signal, an interaction between the TLC plate's Si-OH groups and the chemical can result in hydrogen bonding leading to a shift in the obtained spectrum.[44] Moreover, the sensitivity achieved was only average and the plate cannot be re-used. Another innovative method for TLC-SERS was through the creation of silver nanorod array substrates which are then used directly for both on-chip separation and detection.[9] Silver nanorods are a proven SERS medium but their value in chemical separations is essentially unexplored. In addition, the importance of realizing independent control of separation versus detection conditions cannot be over-estimated.

In this chapter, it is reported that the coupling of TLC-SERS can be accomplished by using conformal blotting as a novel technique to transfer analytes from a TLC plate onto a silver-polymer nanocomposite substrate. SERS imaging by rastering over the substrate provides a means to acquire information rich spectra on separated components. While SERS offers the selectivity to deal with very simple mixtures, spectral features overlap with mixtures of even modest complexity and, thus, the hyphenation of SERS with TLC, without significant detection time constraints, could prove analytically very useful. To the best of our knowledge this is the first illustration of the use of conformal blotting of TLC components onto compliant SERS substrates. Inhomogeneity in the substrates is overcome using a translation device which also serves to reduce photo-degradation of the analyte and substrate. Optimization of blotting conditions and evaluation of analytical performance of the approach are the focus of this chapter.

5.4 Materials and Reagents

Rhodamine 6G (Rh6G) was purchased from Fisher Scientific, 4-aminothiolphenol (ATP) was purchased from Sigma-Aldrich, and malachite green isothiocyanate (MGITC) was purchased from GenoLite Biotek. All stock solutions and subsequent dilutions were prepared with ethanol (95%) from Decon Labs, Inc. and methanol (HPLC Grade) and acetonitrile (HPLC Grade) from Fisher Scientific. Distilled water was obtained using a

Barnstead 1800 (18 MΩ-cm resistivity) filter. Sigma-Aldrich was the source of TLC C-18 silica gel matrix plates.

5.5 Preparation of SERS Substrates

Sylgard® 184 PDMS elastomer kits were purchased from Dow Corning and prepared as directed by manufacturer literature. The prepolymer and the curing agent were prepared in a 10:1 mass ratio, mixed thoroughly, degassed, and poured into a shallow (~ 2 mm) mold. The mold was then placed in a Precision® mechanical convection oven at 100° C for 45 minutes. Using a physical vapor deposition system (Cooke Vacuum Products, Inc. instrument) a nominal thickness of 20 nm of silver metal (99.999% purity from Alfa Aeser) was deposited at a rate of 1.0 Å/s onto the cured PDMS films.

5.6 Blotting and Detection

Initial experiments were performed by simply submerging TLC plates in test analyte solutions for five minutes before being removed and allowed to dry at room temperature for ten minutes. This allowed the analyte to uniformly coat the TLC plate and simplified evaluation of blotting parameters. After drying, the plates were sprayed with ethanol, methanol, or acetonitrile using a Preval Spray Gun (Home Depot). Performed manually, the solvent was sprayed left to right over the TLC plates, with one pass equaling one left to right motion of the Preval Spray Gun. It was determined that 3 passes provided the best blotting signals. The amount of solvent transferred onto the TLC plate for each trial (n=4) yielded a RSD ≈ 9%, demonstrating the amount of solvent sprayed on the plate was relatively consistent despite the manual operation. The rate of dispensing and subsequent evaporation of these common reversed phase organic modifiers was evaluated gravimetrically (see Table 5.1).

When conformal blotting, the freshly sprayed TLC plates were placed in the pressure applicator as seen in Figure 5.1 along with the Ag-PDMS nanocomposite. The TLC plate and nanocomposite film were separated after a specified contact time. Prior

Table 5.1: Comparison of Solvent Evaporation Rates and Physical Properties

Solvent	$T_{1/2}$ (sec)	Dispense Rate (mg/sec)	η (mPa·s)	Vapor Pressure (torr)	ρ (g/mL)	Surface Tension (mN/m)	Polarity Index
Ethanol	121	8.56	1.07	44.6	0.789	22.39	4.3
Methanol	50.2	16	0.544	97.7	0.792	22.5	5.1
Acetonitrile	42.5	6.27	0.343	72.8	0.787	29.1	5.8
Water	--	--	1	20.1	0.998	72.86	10

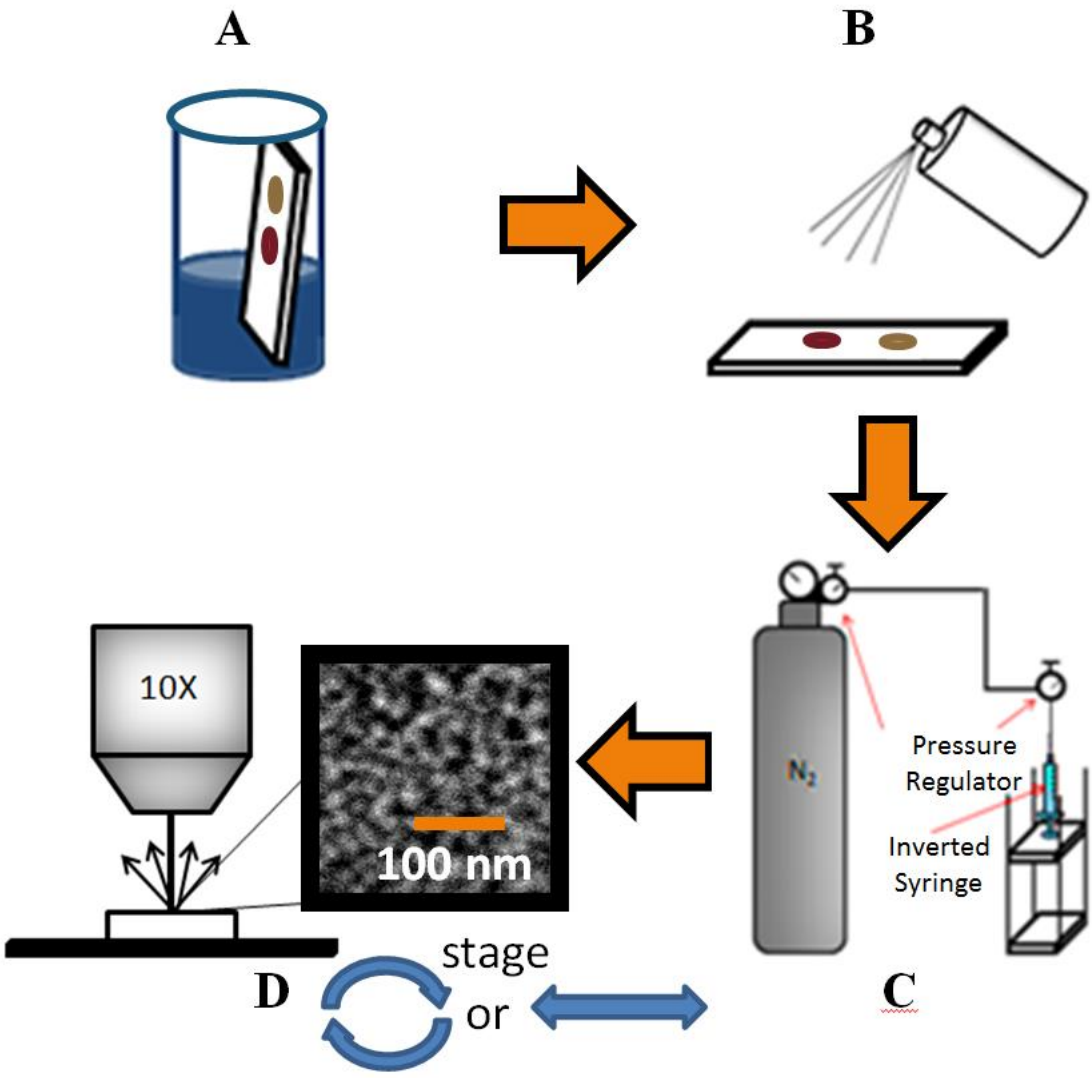

Figure 5.1: Schematic representation for coupling of TLC with SERS: **A** separation of analytes, **B** TLC plate sprayed with selected solvent, **C** wetted TLC plate and silver nanocomposite are conformally blotted using pressure applicator, **D** analysis by SERS (SEM of nanocomposite shown).

research demonstrated the effectiveness of a sample translation technique (STT) at reducing or eliminating sample and SERS substrate photo degradation.[42] That work and some studies reported herein were performed using circular (i.e., rotating)-STT by placing the substrate on a mechanical chopper (Stanford Research System, Inc., Model SR540 Chopper Controller) and operating at speeds of roughly 1000 RPM. The circular-STT is not amenable to interrogating actual TLC spots (initial or post development). In those cases a linear translation was performed. The substrate was placed on a motorized stage (Thor Labs, Model Z612B) and moved 500 μm back and forth at a rate of roughly 500 μm/s to create a linear-STT equivalent of circular-STT.

The nanocomposites were analyzed using a JY Horiba LabRam Raman spectrometer equipped with a Wright Instruments CCD and an ETRI helium-neon laser (633 nm). The confocal hole and slit hole of the instrument were set to 500 μm and 200 μm, respectively. Raman spectra were obtained using a 10X objective (0.25 NA, ∞) using 180° geometry with a 3000 cm^{-1} window centered at 1757 cm^{-1}. The scattered radiation was dispersed with 600 grooves/mm grating and processed for broad background scattering using the LabSpec 4.12 software of our Raman system. The LabRam spectrometer employs an x-y-z programmable translation stage (Marzhauser Wetzlar GmbH; Wetzlar-Steindorff, Germany) for sample manipulation. Imaging was performed by a raster technique with typical stage movements in the x-y dimensions of 100 μm. In an evaluation of blotting related band dispersion, analysis of undeveloped Rh6G spots on TLC plates was performed using an Ar+ laser (488 nm, 10 mW, Cyonics model 2201-20SL) for fluorescence excitation. The unfocused Ar+ laser excitation was reflected onto the TLC plate at an angle of 45^{o} and the LabRam spectrometer (adjusted to monitor the Rh6G emission) was used to monitor the fluorescence while the x-y-z stage of the spectrometer provided a means to measure spot size on the plate.

5.7 TLC Experiments

A separation of the three test analytes was accomplished by first spotting $5*10^{-3}$ M ATP, 10^{-4} M Rh6G, and 10^{-6} M MGITC solutions (1 μL) onto a TLC plate using a HPLC syringe. The separation took place in a traditional development chamber using pure

ethanol as the mobile phase solvent. The solvent front traveled roughly two centimeters beyond the original sample spot before the TLC plate was removed and allowed to dry before being conformally blotted using the optimized conditions. Using fluorescence and visual inspection, R_f values for band center of 0.75, 0.43, and 0.28 were determined for ATP, Rh6G, and MGTIC, respectively. Contrary to blotting and detection conditions, efforts to optimize separation conditions was minimal as it was deemed that overlapping spots permits an illustration of the selectivity advantage of SERS. Using the optimized conformal blotting procedures, the three analytes were transferred onto a silver nanocomposite and evaluated via SERS imaging with linear STT using an acquisition time of 4 seconds and laser power of 1.0 mW.

5.8 Instrumental Considerations

5.8.1 Blotting Apparatus

Evolution of the conformal blotting system (see Figure 5.1) led to a reproducible method for precisely and conveniently blotting onto nanocomposite substrates. Implementation of a stage which only moves in the z-direction created a level surface upon which pressure is applied to mate the nanocomposite and TLC plate. Uneven pressure can lead to destruction of the SERS substrate as well as non-uniform blotting. Furthermore, this stage allowed for smooth separation of the nanocomposite from the TLC plate reducing physical degradation. Employing a pressurized system allowed the nanocomposite and TLC plate to be subjected to precise, controllable contact pressure further reducing variations in blotting trials. After the TLC plates were sprayed with solvent, the TLC plate and nanocomposite were mated and after the specified blotting time, the TLC plate and nanocomposite were manually separated.

5.8.2 Imaging with STT

Prior research has shown the effectiveness of sample translation in significantly reducing photodegradation of analyte and SERS substrate.[42] Unlike engineered substrates which exhibit good morphological reproducibility,[34-39] random morphology

substrates exhibit inhomogeneity and even hot spots that can rise to single molecule sensitivity, but can represent an unwanted complication as well. In the case of Ag-polymer nanocomposites, rastering point by point over the substrate can result in an order of magnitude variation of SERS signal for uniformly analyte-coated substrate; with that variability effectively averaged out with circular-STT.[42] In this work we aim to image TLC plates that inherently have heterogeneity (the separated sample spots) which must be preserved without introducing substrate related artifacts. So a linear translational device that is compatible with this situation was employed. The linear-STT was effective at reducing photodegradation and improving reproducibility of the SERS signals brought about by substrate inhomogeneity. For example, a nanocomposite was exposed to ATP to create a monolayer and then thoroughly rinsed before being interrogated via SERS imaging with a RSD value of 23% across the nanocomposite. This same area was interrogated again using the linear-STT resulting in a RSD of 7.55%, indicating more than a three-fold reduction in RSD in intensity across the nanocomposite. In TLC-SERS experiments, the blotted nanocomposite is imaged with the back-and-forth motion of the linear-STT occurring perpendicular to the development direction. This artificially distorts the spot slightly in the non-development direction but leaves the chromatographically significant dimension unaffected.

5.9 System Optimization

5.9.1 Blotting Solvent Selection

Four conventional reverse phase solvents, water, and the organic modifiers ethanol, methanol, and acetonitrile, were investigated to determine their applicability for conformal blotting. These four solvents exhibit very little SERS background and thus are appropriate for this application. The organic modifiers have varying physical properties significant to conformal blotting such as evaporation rate and strength of solvent. The organic modifiers are all known to be compatible with chromatographic reversed phases. The polarity index (*p*') values for ethanol, methanol, and acetonitrile are 4.3, 5.1, 5.8,[45] respectively (see Table 5.1) and the visually estimated contact angles with

cured PDMS for water and the organic solvents were roughly 90° and 40°, respectively, indicating a compatibility with the nanocomposite films.

The evaporation rate (see $T_{1/2}$ values in Table 5.1) roughly determines the length of time that the conformal blotting can occur because the solvent provides a medium for the analyte to transfer from the TLC plate to the nanocomposite. The expected steps are (i) solubilize the analyte (desirable small solvent-TLC phase capacity factor, k'), (ii) diffusional transfer within solvent to the PDMS surface, (iii) partitioning with the PDMS (desirable large solvent-PDMS k'), (iv) affinity for and adsorption onto the metal surface (very analyte dependent). It is important to note that the metal is slightly submerged in the phase separated surface layer of the PDMS (see Ref. 40 for details). In addition, a potentially important factor in this process of transferring analyte to the nanocomposite is swelling of PDMS by common solvents as has been reported by Whitesides and coworkers.[46] As seen in the table, vapor pressure alone does not determine evaporation rate. The dispersion of the solvent within the porous TLC phase is likely an important factor in determining the length of time the solvent is available to assist transfer analyte to the nanocomposite.

For most analytes the lower the polarity index of the solvent, the higher the degree of solvation. Ethanol was chosen because of its low *p'* and low evaporation rate. Other solvents, such as methanol or acetonitrile, could have been chosen to match the specific analytes. While the best solvent is analyte dependent, it also involves a compromise since an ability to very efficiently solubilize from the TLC phase may reduce the partitioning into the PDMS. Selection of a specific solvent to match a correlating analyte is expected to influence the analytical performance metrics (see below); nevertheless we have focused on ethanol over the other possible solvents in this initial report.

5.9.2 Optimization of Conformal Blotting

The optimum conditions for blotting were determined using ATP as the analyte. Once again, the TLC plates were exposed to analyte to create a uniform monolayer.

Pressure applied to the TLC/nanocomposite system for conformal blotting was tested first because excessive pressure damaged the nanocomposite as clearly observed visually, resulting less Raman enhancement or no enhancement at all. The optimum pressure for conformal blotting was established at six psi using a blotting time of five minutes. Not only did this lead to the maximum SERS intensity, but it also exhibited the lowest RSD in acquired signals (see Table 5.2). Using the optimum pressure, the amount of time the TLC plate and nanocomposite were contacted was investigated. Intensity as a function of time exhibited a non-linear trend and began to plateau around fifteen minutes (see Table 5.3). If needed, conformal blotting could be performed for increased durations of time for trace analysis. Finally, the amount of solvent applied to the TLC plate (see Blotting and Detection Section) was examined. Varying the amount of solvent had very little effect on conformal blotting leading to similar recorded intensities as long as the TLC was wetted enough. This probably occurs because the solvent provides a medium for the analyte to transfer from the TLC plate onto the nanocomposite, but the amount of solvent does not affect that equilibrium. While evaporation rate was studied from the TLC plate as seen in Figure 5.2, it is expected that the evaporation rate decreases significantly after the TLC plate and nanocomposite make contact.

5.10 Analytical Detection Metrics

Using these optimized blotting conditions and circular-STT the RSD for an ATP band was better than 10% (ATP, 1128cm^{-1} band) as seen in Figure 5.3. Signal acquisition parameters were studied toward the goal of establishing the best calibration and limits of detection for the test analytes. Using Rh6G, laser power and acquisition time was investigated. In SERS imaging, increasing laser power or increasing exposure time of the detector can lead to improved spectra but overexposure may result in degradation of both the substrate and analyte. The former can be visually observed with nanocomposite substrates and the latter often is evidenced by broad carbonaceous bands and poor reproducibility.[42] Analysis of Rh6G at a concentration of $3*10^{-6}$ M using different laser powers is shown in Table 5.4 at signal acquisition times of one second.

Table 5.2: Pressure Applied between TLC Plate and Nanocomposite				
	6 Psi	9 Psi	12 Psi	15 Psi
Average	0.70	0.50	0.35	0.50
%RSD (n=3)	4.1	29	66	90

Table 5.3: Time (min) the TLC Plate and Nanocomposite are in Contact							
	3	5	7	9	11	13	15
Average	0.034	0.11	0.28	0.59	0.76	0.79	0.8
% RSD (n=3)	30	7.9	15	3.1	5.5	3.3	7.7

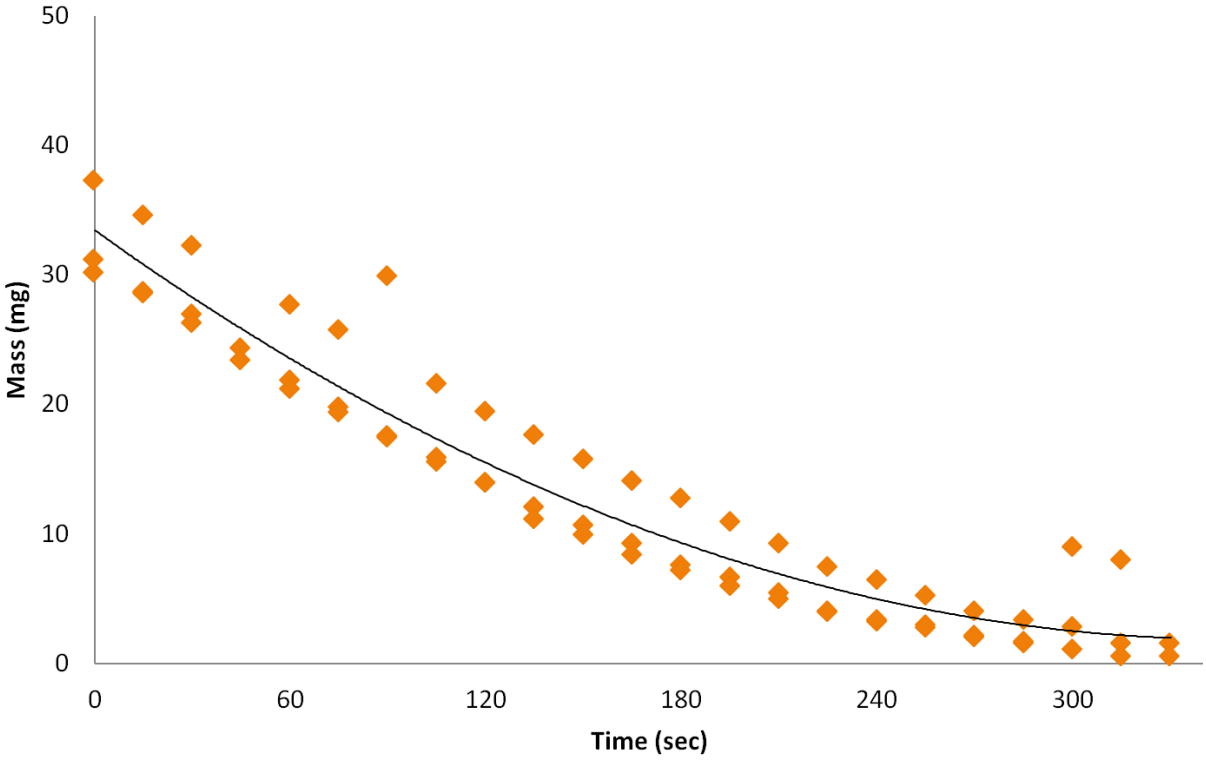

Figure 5.2: Evaporation rate plot for ethanol and data/properties for solvents used in conformal blotting.

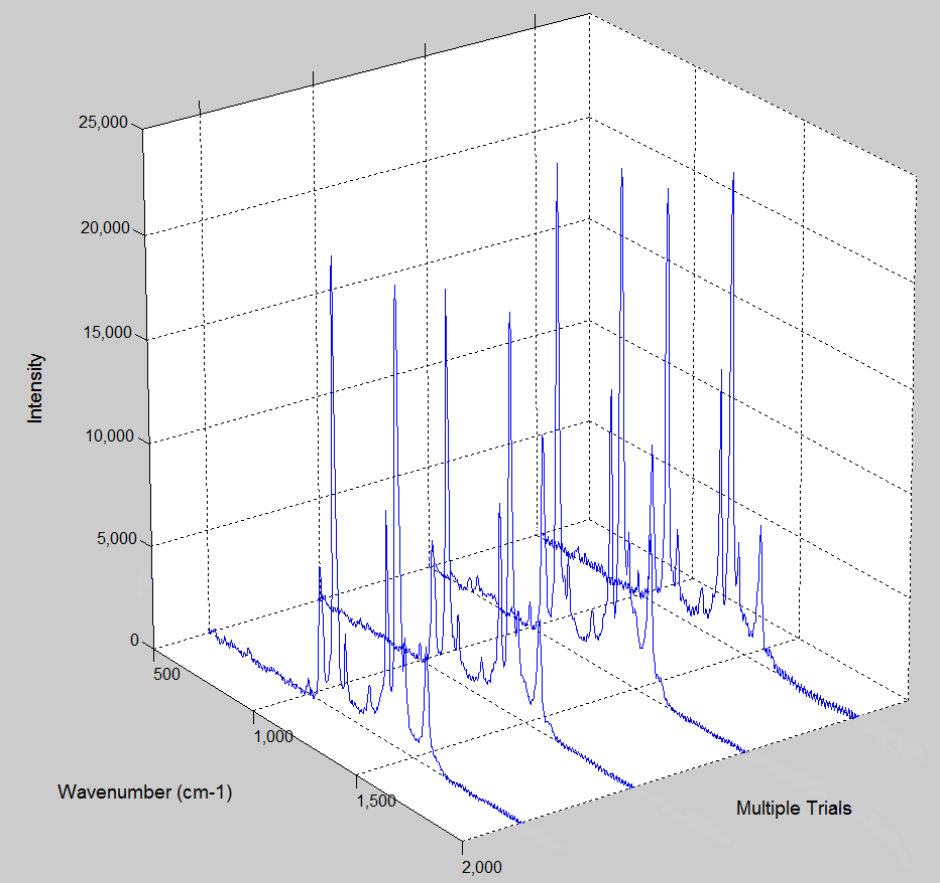

Figure 5.3: Reproducibility study yielding a % RSD of 9.1 (ATP band area 1128 cm^{-1}.

Table 5.4: Factors influencing Rhodamine 6G intensity						Limits of Detection	
Time (sec)	Peak Area (Norm.)	Laser Power (mW)	Peak Area (Norm.)	Conc. (mM)	Blot/Dip Ratio	Sample	LOD (μM)
1	0.12	0.0011	0.005	1	0.03	Rh6G	2.74
2	0.23	0.0094	0.059	0.3	0.03	MGITC	0.147
5	0.53	1.14	0.49	0.1	0.17	ATP	0.220
10	1.0	2.89	1.0	0.03	1.3		
		5.66	0.86	0.01	3.5		

The circular-STT technique is used here to determine the average peak signal. The Rh6G 595 cm^{-1} peak area is the band analyzed for all of Table 5.4. At higher laser powers, there was noticeable degradation of the overall spectra resulting in broader peaks, smaller intensities, and disappearance of certain spectral features. At lower laser powers, the spectra were characteristic of customary Rh6G spectra but were low in intensity. The band area trend in terms of signal acquisition time is predictable (see Table 5.4). The more laser exposure to the sample, the more sample degradation. The table contains peak areas that were normalized and directly correlate to the peak intensity. Combining these optimized parameters, laser power and acquisition time, optimal limits of detection were established.

The limits of detection were established at $1.47*10^{-7}$ M for MGITC, $2.20*10^{-7}$ M for ATP, and $2.74*10^{-6}$ M for Rh6G. These values were determined using a laser power of 2.5 mW and an acquisition time of 10 seconds. A short calibration plot was created using lower concentrations samples of the specific analyte. Using a linear trend fit, the data was extrapolated to a concentration with a S/N of two marking the limit of detection for each analyte. Acquisition time could be increased substantially, however when raster imaging over large areas the analysis time could be prohibitively long. The limit of detection may be improved for these compounds and others by selecting a specific solvent for conformal blotting that best matches the physical properties of the compound. Prior studies by the Sepaniak group have shown that sorption of aromatic compounds, analogs for environmental pollutants, can be influenced by pH and available counterions (e.g., nitrate, sulfate, carbonate, phosphate).[47] The counter-anion of the MGITC is perchlorate (ClO_4^-) which is a strong oxidizer that may lead to oxidation of the silver and a higher limit of detection. In Figure 5.4, a full calibration plot for the Rh6G is demonstrated using an acquisition time of 1 second and laser power of 10 mW. Characteristic of SERS, a plateau is approached at high concentrations as a result of saturation of the SERS active metal surface.[48]

Conformal blotting was compared to directly dipping the nanocomposites in the analyte to investigate the efficiency of conformal blotting. In Table 5.4, the blotting to

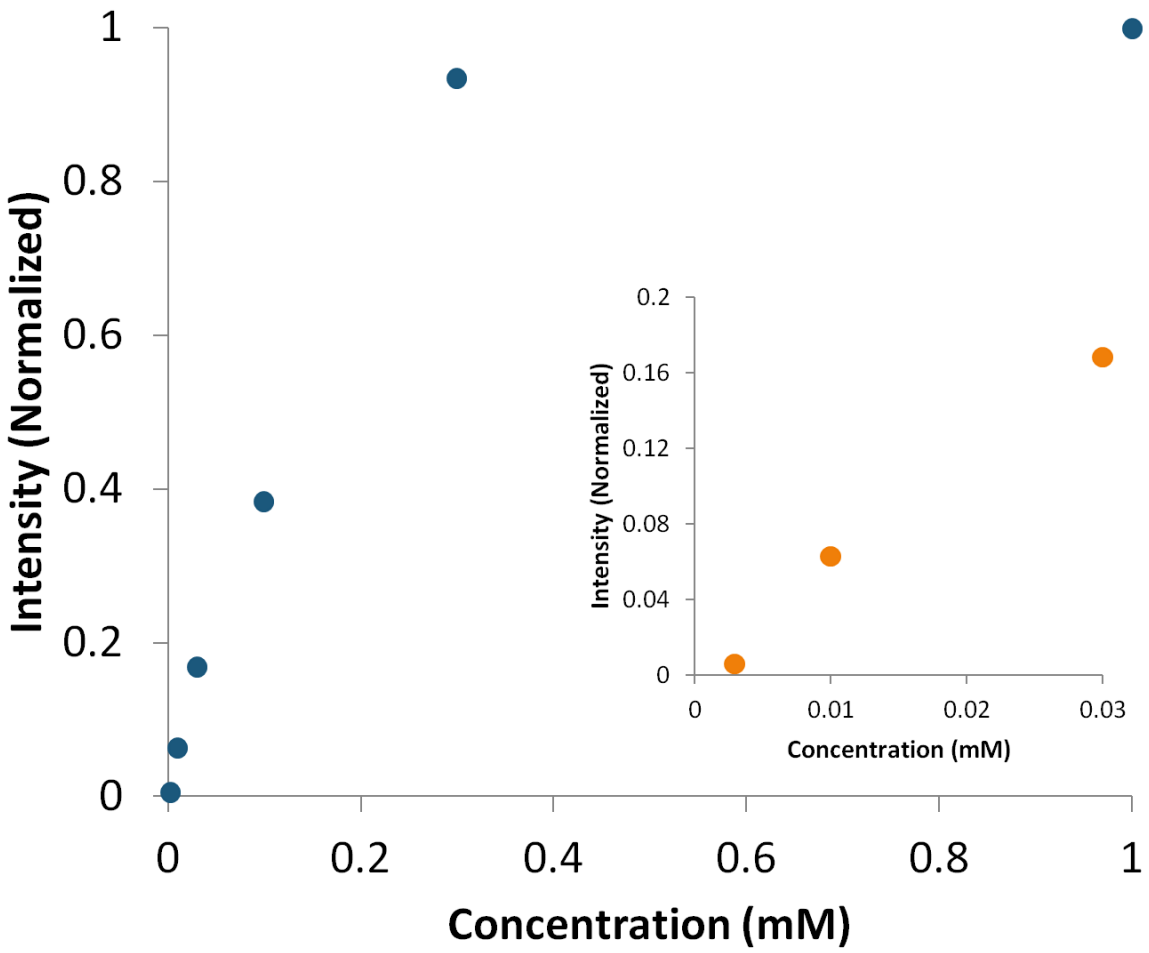

Figure 5.4: Calibration plot for blotting of R6G (insert is blow up of low concentrations). The LOD data were obtained under optimized conditions.

dipping signal ratio can be seen. At low concentrations, conformal blotting is very efficient and produced a signal equivalent to that obtained when the nanocomposite was dipped directly in the same concentration. Conversely the blotting process appears to be very inefficient at high concentrations. We believe this is misleading because the TLC plate becomes saturated more easily than the nanocomposite film which is largely composed of PDMS, a high capacity solid phase extractor.[41, 42] Thus, at high concentrations the available Rh6G on the TLC plate for blotting is considerably less than expected whereas direct dipping of the nanocomposite material into the same Rh6G solution is very efficient.

5.11 Analyte TLC Spot Experiments

5.11.1 Blotting related dispersion

An important aspect of all chromatographic processes is band (or spot) dispersion which leads to larger plate height (H), diminished resolution, and dilution-related loss in detection sensitivity. While factors that contribute to H are extremely complex in TLC, the treatment by Guiochon [49] is generally regarded as comprehensive and is based on the validity of the Knox equation that is common to HPLC theory. Thus eddy diffusion, axial diffusion, and resistance to mass transfer are expected to be relevant. Similarly, non-separation effects must be considered as sources of dispersion. Typically, the sample spotting process can be thought to be one such factor. However, relative to the work report herein, we must consider the blotting process and its effect on the size of the TLC spot when transferred to the nanocomposite. Blotting related spot dispersion was examined by comparing undeveloped Rhodamine 6G spots; fluorescence on the TLC plate and SERS on the nanocomposite film. Linear-STT was employed to ensure uniformity throughout the nanocomposite while not distorting the spot in the direction that would be used in development. Rhodamine 6G at a concentration of 10^{-4} M was spotted onto a TLC plate and allowed to dry at room temperature. Using an Argon laser (488 nm), fluorescence of the undeveloped spot was measured as seen in Figure 5.5. The slightly elliptical appearance of the spot is due to the linear-STT movement of 500 µm. The spot was then conformally blotted onto the nanocomposite using the optimized

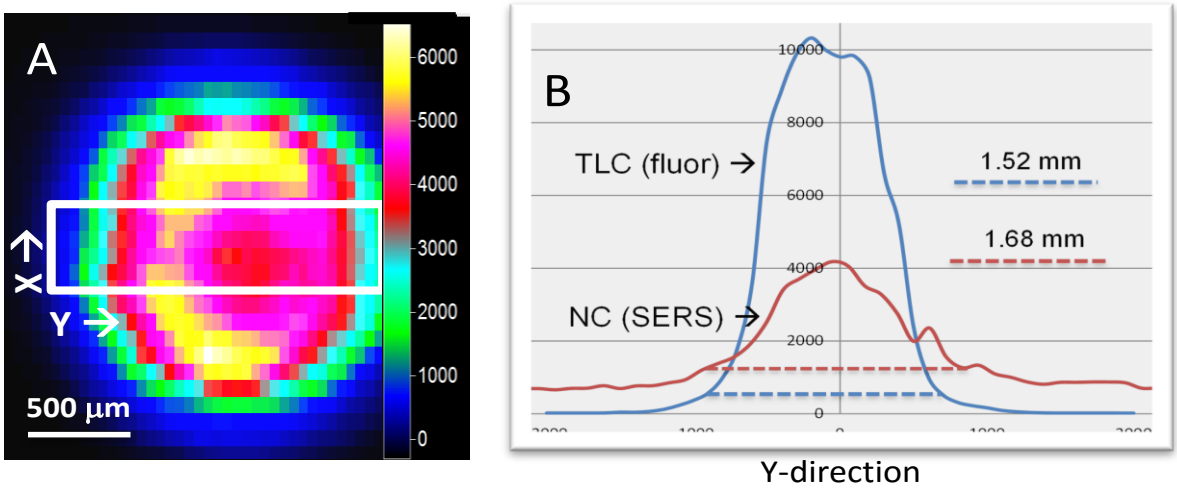

Figure 5.5: **A** Complete raster plot for typical undeveloped spot of Rh6G on a TLC plate (Fluorescence). The incremental jumps were 100 mm in each direction. In addition, the LSTT was applied in the X-direction hence creating the elliptical appearance of the spot. **B** Compares the fluorescence width of a spot (undistorted Y-direction) of a spot on a TLC and the SERS response after blotting that spot onto a nanocomposite substrate (the rectangle in A highlights the region of the raster used for B). The increase in baseline width of the spot was only about 10%.

procedure and the SERS image obtained. The dried spot on the TLC plate is expected to be stable. However, while in ethanol during the blotting one can expect some diffusional and perhaps slight convection-related broadening upon plate-nanocomposite contact. As seen in Figure 5.4, the increase of the width of the spot was approximately 10% indicating that diffusion through conformal blotting is present but not in significant amounts. Rh6G is known to adsorb strongly to the metal. Analytes without such strong adhesion may diffuse while in the PDMS phase, but if the detection is performed within a relatively short period of time this should be minimal. A similar situation was demonstrated in prior work when the nanocomposite material was molded into a μ-fluidic platform and used for electrophoretic separations.[48]

5.11.2 Separation with 3-D detection

A separation of the three test analytes, MGITC, Rh6G, and ATP at concentrations of 10^{-6} M, 10^{-4} M, and 10^{-3} M, respectively, was carried out on a TLC plate using pure ethanol as the mobile phase. The mixture of analytes was spotted onto the TLC plate using an HPLC syringe. After the solvent traveled roughly two centimeters beyond the original sample spot, the TLC plate was removed and allowed to dry at room temperature before being conformally blotted using the optimized conditions. Fluorescence and visual identification of analytes on the TLC plate indicate R_f values of 0.75, 0.43, and 0.28 for ATP, Rh6G, and MGTIC, respectively. This was confirmed using SERS imaging, as seen in Figure 5.6, by focusing on a specific excitation band for each analyte, 778 cm^{-1} for MGITC, 1128 cm^{-1} for ATP, and 595 cm^{-1} for Rh6G, respectively. In both the 3-D plot and spectrally specific chromatogram, it is apparent that the ATP thoroughly separated from the Rh6G and MGITC. However, the Rh6G and MGITC did not exhibit thorough separation resulting in overlapping chromatographic bands due to poor resolution. R_f values are not always a viable option of qualitative analysis thus SERS can be employed to identify components. Moreover, quantitative analysis is possible even for overlapping components based on their specific, individual spectral features offsetting a lack of spatial resolution. The efficiency for this conventional TLC separation (developed ATP spot) is only roughly 400 plates

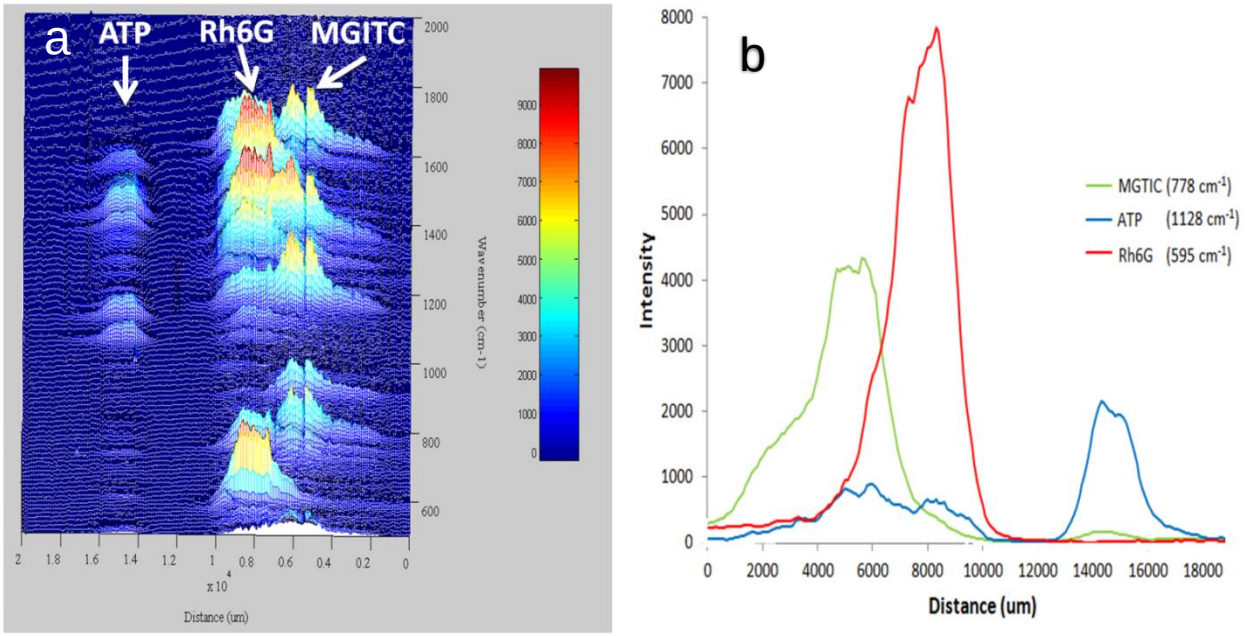

Figure 5.6: (a) 3-D Chromatogram showing the separation of MGITC, Rh6G, and ATP with associated spectra. (b) Chromatogram of the three test compounds based on an spectral peak specific to each compound.

underscoring the importance of using an information rich technique to analyze unresolved spots on the developed plate. Previous research by the Sepaniak group has shown underscoring the importance of using an information rich technique to analyze unresolved spots on the developed plate. Other research by the Sepaniak group has shown that is it possible to distinguish analytes from each other in an aqueous mixture.[50] The system discussed has many different applications to TLC because the separations can take place on any 2-D planar separation medium. Though we used reverse phase TLC, one could employ many different forms of TLC such as normal phase, special phases (i.e. modification of SiO_2 gel, ion-pairing, molecular imprinted polymers, electrospun polymers), or highly-ordered lithographically prepared pillar arrays.[51, 52, 53]

5.12 Conclusion

In this chapter, the demonstration of the possibility of coupling thin layer chromatography with SERS through conformal blotting is presented. The unique attributes of Ag-PDMS nanocomposites as pliable and highly SERS-active substrates are exploited. Optimization of blotting led to the efficient transfer of the analyte from the TLC plate onto the nanocomposite substrate with little spot dispersion and good sensitivity and reproducibility. Limited spatial separation can be overcome by SERS imaging, an information rich technique, which enhances both quantitative and qualitative information, potentially expanding applications to samples that are more complex than normally possible in TLC. Note that while the test analytes used herein are Raman active that are often used in the development of many SERS approaches, other Raman active analytes should be applicable. Additionally, conformal blotting effectively isolates separation conditions from that required for detection. Thus, this versatile approach is expected to be applicable to many different types of 2-D planar separation platforms and separation media.

5.13 Acknowledgements

This material is based on work supported in part by the National Science Foundation under Grant CHE-1144947 with the University of Tennessee. Additional support was provided by the University of Tennessee, Knoxville, Chancellor's Honors Program.

5.14 References

1. Poole, S. K.; Poole, C. F. *J. of Chromatogr. A*. **2010**, *19,* 2648-2660
2. Poole, C. F *J. of Chromatogr. A.* **2003**, *1000*, 963-984
3. Sherma, J. *Anal. Chem.* **2004**, *76*, 3251-3262
4. Sherma, J.; Fried, B. *Handbook of Thin-Layer Chromatography*, 3rd ed.; Marcel Dekker: New York, 2003
5. Poole, C. F.; Poole, S. K. *Chromatography Today*; Elsevier: Amsterdam, 1991; pp 649-728
6. Cserhati, T. *Biomed. Chromatogr.* **2002**, *16*, 303-310
7. Orinak, A.; Arlinghaus, H. F.; Vering, G.; Justinova, M.; Orinakova, R.; Turcaniova, L.; Halama, M. *J. Planar Chromatogr.-Mod. TLC* **2003**, *16*, 23-27
8. Istvan, K.; Keresztury, G.; Szep, A. *Spectrochim. Acta, A.* **2003**, *59*, 1709-1723
9. Jing C.; Abell, J.; Huang, Y.; Zhao, Y. *Lab Chip* **2012**, *12*, 3096-3102
10. Wang, Y.; Zhang, J. Z.; Ma, X. Y. *Spectrosc. Spectral Anal.* **2004**, *24*, 1373
11. Brosseau, C. L.; Gambardella, A.; Casadio, F.; Grzywacz, C. M.; Wouters, J.; Duyne, R. P. *Anal Chem.* **2009**, *81*, 3056-3062.
12. Walworth, M.; Stankovich, J.; Van Berkel, G.; Schultz, M.; Minarik, S. *Rapid Commun. Mass Spect.* **2012**, *26*, 37-42
13. Minami, Y.; Yokoi, S.; Setoyama, M.; Bando, N.; Takeda, S.; Kawai, Y.; Terao, J. *Lipids* **2007**, *42*, *1055-1063*
14. Y. Kawai, M. Miyoshi, J. Moon, J. Terao *Anal. Biochem.* **2006**, *360*, 130-137
15. Dieringer, J. A.; McFarland, A. D.; Shah, N. C.; Stuart, D. A.; Whitney, A. V.; Yonzon, C. R.; Young, M. A.; Zhang, X.; Van Duyne, R. P. *Faraday Discuss.* **2006**, *132*, 9–26.
16. Kneipp, K.; Kneipp, H. *Appl. Spectrosc.* **2006**, *60*, 322A.
17. Moskovits, M. *J. Chem. Phys*. **1978**, *69*, 4159
18. Moskovits, M. *Rev. Mod Phys*. **1985**, *57*, 783
19. Kneipp, K.; Kneipp, H. *Isr. J. Chem.* **2006**, *46*, 299–305.
20. Kneipp, K.; Wang, Y.; Kneipp, H, et al. *Phys. Rev. Lett.* **1997**, *78*, 1667
21. Kneipp, K.; Kneipp, H; Deinum, G., et al. *Appl. Scpectrosc.* **1998**, *52*, 175
22. Kneipp, K.; Kneipp, H; Kartha, V. B., et al. *Phys. Rev. E.* **1998**, *57*, R6281
23. Zou, S.L.; Schatz, G. C. *Chem. Phys. Lett.* **2005**, *403*, 62
24. Gopinath ,A.; Boriskina, S.V.; Reinhard, B. M.; Dal Nergro, L. *Opt. Express*, **2009**, *17*, 3741-3753
25. Musick, M. D.; Keating, C. D.; Lyon, L. A.; Botsko, S. L.; Pena, D. J.; Hollay, W. D.; McEvoy, T. M.; Richardson, J. N.; Natan, M. J. *Chem. Mater.* **2000**, *12*, 2869–2881.
26. Park, S.-H.; Im, J.-H.; Im, J.-W.; Chun, B.-H.; Kim, J.-H. *Microchem. J.* **1999**, *63*, 71–91.
27. Lacy, W. B.; Olson, L. G.; Harris, J. M. *Anal. Chem.* **1999**, *71*, 2564–2570.
28. Mulvaney, S. P.; He, L.; Natan, M. J.; Keating, C. D. *J. Raman Spectrosc.* **2003**, *34*, 163–171.
29. Reilly, T. H., III; Corbman, J. D.; Rowlen, K. L. *Anal. Chem.* **2007**, *79*, 5078–5081.
30. Li, J.; Fang, Y. *Spectrochim. Acta, Part A* **2007**, *66A*, 994–1000.
31. Murgida, D.; Hildebrandt, P. *Top. Appl. Phys.* **2006**, *103*, 313–334.
32 Pristinski, D.; Tan, S.; Erol, M.; Du, H.; Sukhishvili, S. *J. Raman Spectrosc.* **2006**, *37*, 762–770.

33. Qian, X. M.; Ansari, D.; Nie, S. *Proc. SPIE-Int. Soc. Opt. Eng.* **2007**, *6448*, 1–12.
34. Oran, J. M.; Hinde, R. J.; Abu Hatab, N.; Sepaniak, M. J. *J. of Raman Spectrosc.* **2008**, *39*, 1811-1820
35. Wells, S. M.; Polemi, A.; Lavrik, N. V.; Shuford, K. L.; Sepaniak, M. J. *Chem. Comm.* **2011**, *47*, 3814-3816
36. Bhandari, D.; Kravchenko, I. I.; Lavrik, N. V.; Sepaniak, M. J. *J. Am. Chem. Soc*. **2011**, *133*, 7722-7724
37. Green, M.; Liu, F. M *J. Phys. Chem. B* **2003,** *107*, 13015-13021
38. Yan, B; Thubagere, A.; Premasiri, W. R.; Ziegler, L. D.; Dal Negro, L.; Reinhard, B.M. *ACS Nano*. **2009**, *3*, 1190-1202
[39] Haynes, L. C.; Van Duyne, R. P. *J. Phys. Chem. B,* **2003**, *107*, 7426-7433
40. De Jesus, M. A.; Giesfeldt, K. S.; Sepaniak, M. J. *J. Raman Spectrosc.* **2004**, *35* (10), 895–90.
41. Giesfeldt, K. S.; Connatser, R.M.; De Jesús, M.A.; Lavrik, N.V.; Dutta, P.; Sepaniak, M. J. *Appl. Spectrosc.* **2003**, *57*, 1346
42. De Jesus, M. A.; Giesfeldt, K. S.; Sepaniak, M. J. *Appl. Spectrosc.* **2003**, *57*, 428-438
43. Henzel, U. B. *Journal of Chromatography Library*; Zlatkis, A., Kaiser, R. E., Eds.; Elsevier: Amsterdam, 1977; Vol. 9, Chapter 8.
44. R.L. White, *Anal. Chem.* **1985**, *57*, 1819.
45. L. R. Snyder, in *Techniques of Chemistry*, 2nd ed., Vol. III, Part I, A. Weissberger and E. S. Perry, eds., Wiley-Interscience, New York, 1978, Chap. 2.
46. Lee, J. N.; Park, C.; Whitesides, G. M. *Anal. Chem.* **2003**, *75*, 6544-6554
47. DeJesus, M. A.; Giesfeldt, K. S.; Sepaniak, M. J. *App. Spectrosc.* **2004**, *58*, 1157-1164
48. Connatser, R.M.; Cochran, M.; Harrison, R.J.; Sepaniak, M.J. *Electrophoresis*, **2008**, 29, 1441-1450.
49. Guiochon, G.; Antoine, S. *J. Chromatogr. Sci.* **1978**, 16, 470-481.
50. Bhandari, D.; Walworth, M. J.; Sepaniak, M. J. *Appl. Spectrosc.,* **2009,** *63,* 571-578
51. Lavrik, N.K.; Taylor, L.; Sepaniak, M.J. *Lab-on-a-Chip*, **2010**, *10,* 1086-1094
52. DeMalsche, W.; Eghbali, H.; Clicq, D.; Vangelooven, J.; Gardeniers, H.; Desmet, G. *Anal. Chem*. **2007**, *79*, 5915.
53. Clark, J.E.; Olesik, S.V. *Anal. Chem*. **2009**, 81, 4121-4129.

Chapter 6

Manipulating Inter Pillar Gap in Pillar Array Ultra-Thin Layer Planar Chromatography Platforms

Chapter 6 is an adaption of a research article in The Analyst, 2016, 141, 1239-245. The article describes nano-fabricated photolithographically prepared pillar array platforms where the inter-pillar gap was manipulated via PECVD and ALD to study effect on efficiency of decreased dimensions and increased surface area.

6.1 Abstract

An advantage of separation platforms based on deterministic micro- and nano-fabrication, relative to traditional systems based on packed beds of particles, is exquisite control of all morphological parameters. For example, with planar platforms based on lithographically-prepared pillar arrays the size, shape, height, geometric arrangement, and inter pillar gap can be independently adjusted. Since inter pillar gap is expected to be important in determining both resistance to mass transfer in the mobile phase as well as flow rate, which influences the mass transfer effect and axial diffusion, we study herein the effect of reducing inter pillar gaps on capillary action-based flow and band dispersion. Atomic layer deposition is used to narrow the gap between the pillars for photo-lithographically defined pillar arrays. The plate height of gap-adjusted arrays is modeled based on predicted and observed flow rates. A reduction in flow rate with smaller gaps hinders efficiency in the modeled case and is correlated with actual separations. A conclusion is drawn that simultaneously reducing both the gap and the pillar diameter is the best approach in terms of improving chromatographic efficiency.

6.2 Introduction

Reduction of the dimensions of liquid phase separation systems has been pursued for decades,[1] both in the overall dimensions of the systems (e.g., packed capillaries and open channel systems) [2-5] and in the size of the packing materials (e.g., core shell packing with < 3 um diameters).[6-9] Desmet and coworkers have pioneered a reduced separation approach involving pillar arrays in narrow channels.[10] The Sepaniak group has pursued the pillar arrays for chemical separations (PACS) approach as well and shown advantages of reducing the dimensions of the pillars and inter pillar gaps, both in enclosed pressure driven chips and open planar systems driven by capillary action.[11-12] The latter open systems with pillar diameters typically of 2 µm diameter and 4 µm pitch

provided surprisingly fast capillary action based flow and plate heights of <2 um. Herein we describe the outcome of further reducing the inter pillar gap to determine if the scaling trends in flow and dispersion (plate height) continue.

Advantages of enclosed systems have been documented by Desmet et al. and, similarly, for open systems have been discussed by Kirchner et al.[1, 12,13] In summary, nearly perfect ordered pillar arrays exhibit less flow resistance than traditional packed and monolithic columns.[11, 14] Studies show that pillar arrays wick faster than traditional TLC, reducing molecular diffusion, and have better mass transfer due to the pillar dimensions being substantially smaller than TLC bed particles. Plate heights were significantly smaller than for TLC.[12] Typically, the open planar format chips range from 3 cm x 3 cm to < 0.5 cm x 3 cm allowing the separation media to be portable to on site testing. The separation systems are reusable to help offset production costs and require small sample volumes. According to the van Deemter equation, perfectly ordered arrays are expected to reduce plate height significantly and even reduce the eddy-dispersion term to near zero. Due to these advantages, fabrication of these ultra-thin layer separation platforms is a realistic approach for manufacture even with the moderate expense. Recently, a metal dewetting procedure for the fabrication of pillar arrays has further reduce costs.[15-16]

However, disadvantages do exist for PACS as they inherently exhibit several shortfalls. PACS when formed via photolithography [12] contain a non-retentive surface. In order to correct for this surface, researchers have employed depositing silicon oxide layers via plasma enhanced chemical vapor deposition (PECVD).[17-18] Other attempts at creating more surface area for PACS have been with electrochemical anodization to create a mesoporous silicon layer.[19] Recently, our group has deposited porous silicon oxide (PSO) on pillar array surfaces using a room temperature PECVD protocol.[13, 20] The PSO layer allows for faster wicking capabilities, super hydrophobicity (contact angle > 150^{o}), enhanced fluorescence brightness, and chemically selective transport.[21]

An area of interest with PACS is the ability to obtain smaller inter pillar gaps (smaller than 2.0 μm). Many research facilities including universities only have access to mid-UV

lithography which allows for the replication of the mask with larger features.[22-23] Using atomic layer deposition (ALD), silicon oxide is conformally deposited onto silicon pillars which cause the pillars to increase in diameter and decrease the inter pillar gap. This in turn can reduce plate height according to the C_M term in the Van Deemter equation (see below). This research is devoted to examining the performance of inter pillar gaps with decreasing dimensions of 1.1 μm, 0.8 μm, and 0.5 μm, along with a more retentive separation media created to increase the surface area. Capillary action is used within the studies described due to the simplicity for planar chromatography solvent development.

In order to determine the best inter pillar gaps to fabricate a solvent wicking model reported by Mai et al. was employed.[24] Mai et al. concludes that wicking ability can be controlled by simply changing the geometry of a textured surface. Since performance of capillary action driven systems is very dependent on flow rate, the model provides predictive insights. However, the predictive model does not include surface roughness (addition of PSO) or any evaporation effects, causing the model to not fully depict the outcome of the experimental results.

6.3 Fabrication of 2D-Pillar Arrays with Reduced Dimensions

6.3.1 Lithographically Fabricated Pillar Arrays

The pillar arrays used in this study were initially fabricated using a procedure previously reported by Kirchner et al.[12] A CAD program is used to define the pillar pattern, and a Heidelberg LW, Model DWL66 laser writer (Center for Nanophase Materials Science, Oak Ridge National Laboratory, Oak Ridge, TN), is used to create an initial chrome mask. Following, a double layer of positive photoresist (lift-off resist LOR-1A overcoated by positive tone phototresist 955CM-2.1, MicroChem Corp.) was added to the top of a silicon wafer. The pattern for the arrays was made using a Quintel Inc. contact aligner designed to mask off the non-pillared areas which are then etched. Using UV light, holes were formed in the positive photoresist where the pillars are created. Approximately 15 to 20 nm of chromium was deposited onto the wafer to act as the etchant mask, after which the remaining photoresist is removed leaving areas of

non-etched chromium (i.e., the pillar tops). A Bosch™ process was performed to generate pillars with a height of ~20 μm (system 100 Plasma Etcher, Oxford Instruments). The wafers were then scribed and cleaved into individual 0.5 cm by 3 cm pillar array chips prior to differing deposition amounts of silicon oxide via ALD and PECVD. All pillar arrays were functionalized with n-Butyldimethyl-chlorosilane (≥97%, Acros Organics) to enhance hydrophobicity of the substrate.[25] Figure 6.1 provides images of the stages of the processing.

6.3.2 Pre-Treatment of Pillar Arrays

Before any depositions are conducted the pillar arrays have excess fluoropolymer and chrome from the fabrication process. Fabrication of pillar arrays relies on anisotropic etching of silicon using well established reactive ion etching in a fluorine-based plasma (System 100 Plasma Etcher, Oxford Instruments). This Bosch™ processing step involves plasma polymerization of C_4F_8 precursor gas and is associated with condensation of Teflon-like fluoropolymer on sidewalls and tops of the resulting pillars. Such fluoropolymer deposits consist of predominantly linear $(CF_2)_n$ chains characterized by a low cross-linking degree.[26] In order to remove the fluoropolymer we expose samples to high intensity oxygen plasma on the plasma etcher instrument for 10 min using a recipe that combines 2000 W of inductively coupled plasma and 20 W of capacitively coupled plasma.

This oxygen plasma cleaning procedure is followed by wet etching of the residual chromium masking layer (present on top of the pillars) for 30 s using CR-14S (Cyantek Corp.) The CR14S etchant is based on a mixture of ceric ammonium nitrate and acetic acid with thickening and stabilizing additives. Thorough rinsing with DI water and blow drying of samples with filtered nitrogen concludes the cleaning/etching step (see Figure 6.1). This cleaning step does not ensure that all of the fluoropolymer and chrome are removed, nor is it entirely necessary to remove all due to large depositions performed on the pillar arrays with ALD and PECVD.

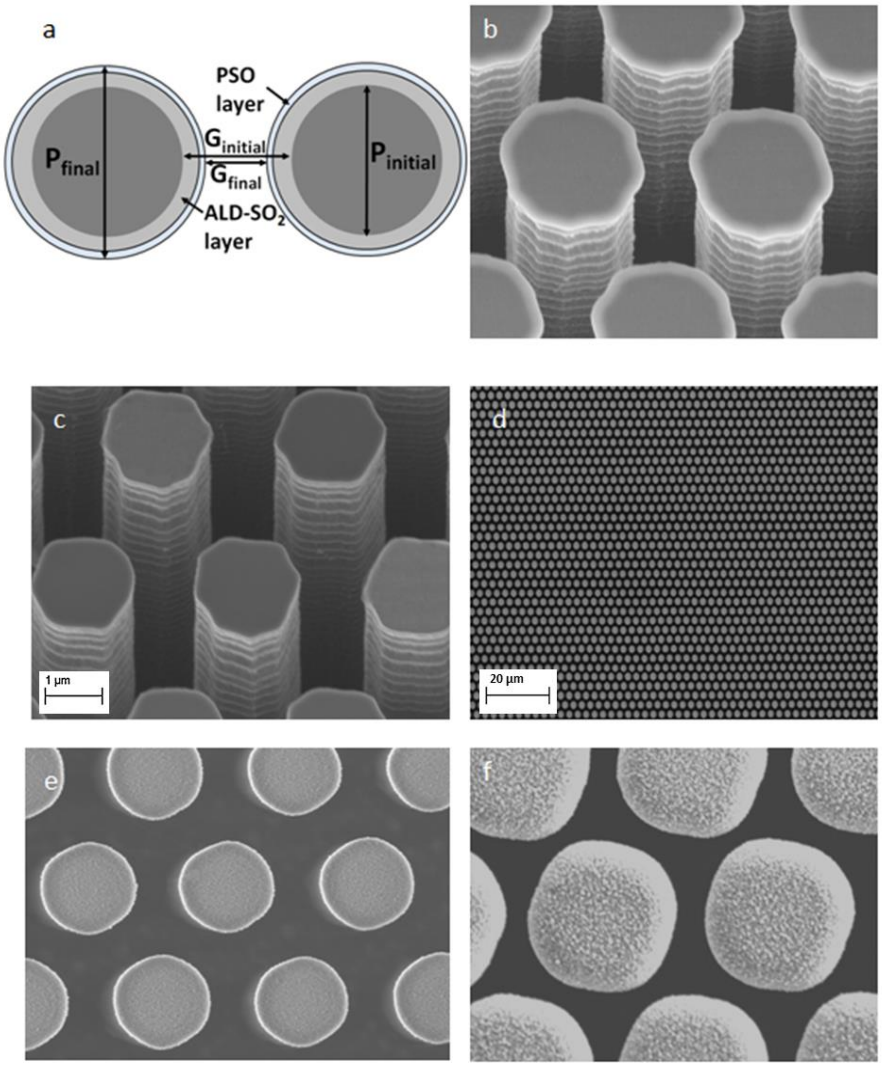

Figure 6.1: Stages of depositions on pillar arrays; (a) schematic diagram of the depositions of silicon dioxide performed with ALD and PECVD where depositions ranged from 50 nm PSO to 300 nm ALD with 50 nm PSO; (b) SEM of original pillar arrays without a chrome etch (c) SEM of original pillar arrays with a chrome etch; (d) low resolution SEM image of 1.9D1.1Ggapped chips; (e) magnified SEM image of 1.9D1.1G gapped chips; (f) magnified SEM images of 2.5D0.5G gapped chips.

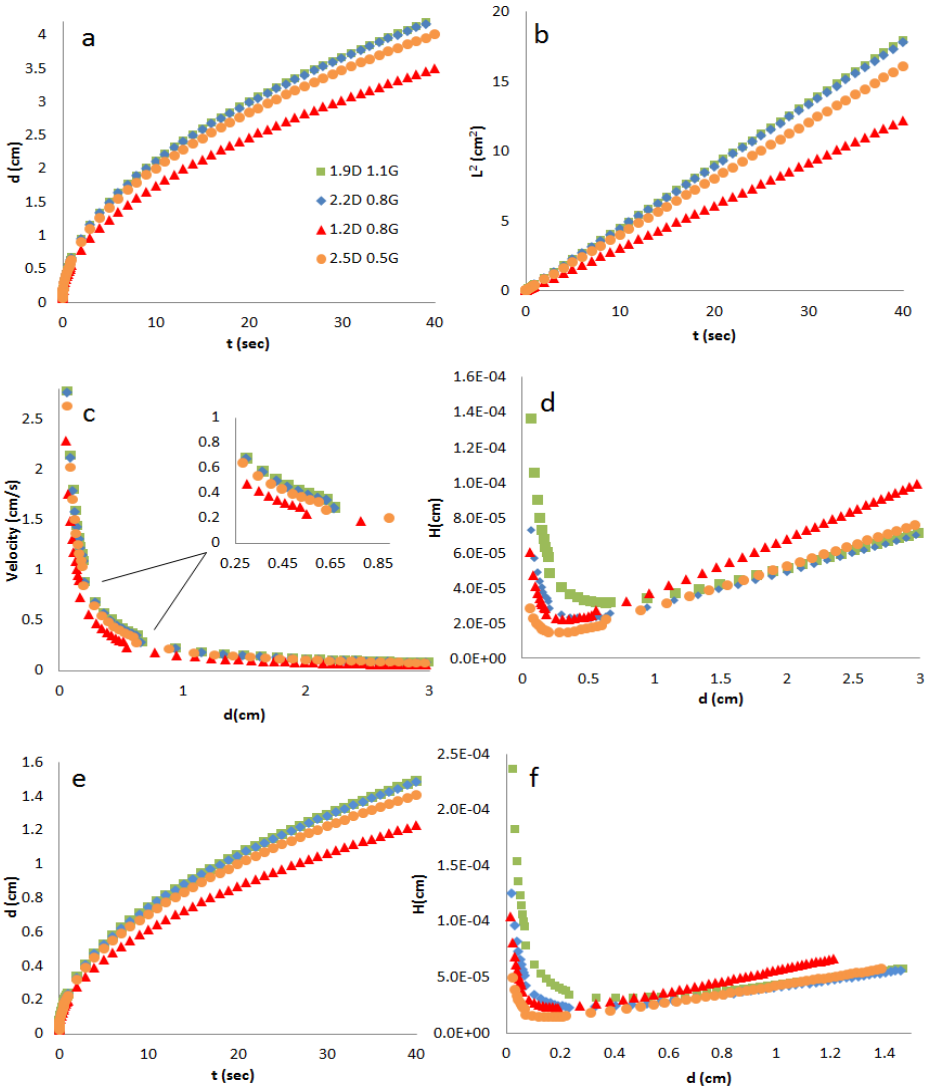

Figure 6.2: Predictive solvent flow of acetonitrile (a)-(d) and 2-propanol (e)-(f); (a) distance versus time of four different morphologies; (b) position squared versus time to illustrate linearity; (c) distance versus velocity; (d) efficiency plot to determine optimum gapped scenario; (e) distance versus time and (f) efficiency plot for 2-propanol.

6.3.3 Controlling Inter-Gap Dimension

In order to create different gap distances, differing amounts of silicon dioxide was deposited using ALD in order to receive an extremely uniform deposition on all pillar tops and sidewalls. The original 0.5 cm by 3 cm chips had pillar heights of ~20 μm, diameters of 1.8 μm, and gaps of 1.2 μm. One additional case was tested where the original pillar diameter started out smaller (~0.8μm). Four different gap cases were fabricated. In order to increase surface area of the chips to achieve an optimum separation platform, the PECVD was used at room temperature to deposit a PSO layer. Desmet et al. has shown that the porous silicon layer adequately increases surface area in ordered arrays and therefore allows more surface silanols for bonding with the with the n-Butyldimethylchlorosilane reverse phase stationary phase used herein.[19, 27]

For cases I-III, the 1.8 μm diameter chip was used and case IV the 0.8 μm diameter chip was used. Cases II-IV were put in the ALD instrument for a 150 nm deposition of uniform silicon dioxide. After the first deposition, Case II and IV chips were removed from the instrument and Case III chips remained for another 150 nm deposition. Depositing 150 nm of silicon oxide on the sidewalls of pillars causes the gap to close by 300 nm. At the end of the atomic layer depositions, all chips were placed in the PECVD chamber to deposit 50 nm of PSO. This low temperature PECVD protocol produces PSO that has been shown to be suitable for chromatography.[13] This caused another 100 nm closing of the gap. The goal was to create a 1.9 μm diameter/1.1 μm gap chip (1.9D 1.1G), a 2.2 μm diameter/0.8 μm gap chip (2.2D 0.8G), a 2.5 μm diameter/0.5 μm gap chip (2.5D 0.5G), and a 1.2 μm diameter/0.8 μm gap chip (1.2D 0.8G).

6.4 Measuring Flow and Band Dispersion

To measure flow each 3 cm x 0.5 cm pillar array chip was sealed in a 20 mL vial with ~ 7 mL of the respective solvent (acetonitrile or 2-propanol) for a period of 5 minutes to allow the chamber to reach equilibrium. The vial is fitted with a plunger in order to introduce the chip to solvent once the chamber/vial reaches equilibrium. The pillar array chip is adhered to the plunger via double-sided tape. A video is recorded of the solvent

flow for each gap size and analyzed with imageJ software to ensure precise distance measurements with time.

For band dispersion experiments an analyte spot of ~200 um diameter was administered to the pillar array via an HPLC syringe. The analyte spotted was a mixture of 10^{-6} M sulfur rhodamine, 10^{-5} M coumarin 540A, and 10^{-5} M coumarin 120 in 60:40 methanol:water. The spot was typically administered 3 mm from the bottom of the array to avoid dipping the analyte directly into the mobile phase. Band dispersion measurements and a separation could be performed simultaneously. The analyte spot was measured before and after a separation was performed using 50:50 methanol:water as the mobile phase. Separations were performed using the 20 mL vial as described above. Separations were analyzed at 2 and 4 minute development times.

To measure band dispersion, separated bands are imaged with a fluorescence microscope and once saved are opened with ImageJ software. On the fluorescence microscope the field of view at the 10x microscope objective is 1400 µm. In the ImageJ software the image is manually set to a field of view of 1400 µm. For exact band measurements an area of the band is highlighted and an intensity graph is created. Tangential lines from a best-fit Gaussian are used to determine separated band width. Where the tangential lines hit the x-axis estimates the width of the band (4σ). As is common for planar chromatography, spot-based bands are only roughly Gaussian giving some error with the determination of band variance. The average of multiple runs and measurements were made to minimize this effect.

6.5 Modeling of 2D-Pillar Arrays with Reduced Dimensions

While factors that contribute to plate height, H, are extremely complex in planar chromatography, the treatment by Guiochon is generally regarded as comprehensive and is based on the validity of the van Deemter equation (Equation 6.1) that is common to HPLC theory.[28]

$$H = A + \frac{B}{v} + (C_s + C_m)v \qquad [6.1]$$

Generally plate height is dependent on eddy diffusion, A, longitudinal diffusion, B, which is influenced by the mobile phase velocity (v) and the resistance to mass transfer in both the stationary and mobile phases, C_s and C_m, respectively. Expansion of the van Deemter equation to include the parameters that influence plate height is shown in Equation 6.2.

$$H = 2\lambda d_p + \frac{2\gamma D_M}{v} + \frac{qk' d_f^2 v}{(1+k')^2 D_s} + \frac{\omega {d_p}^2 v}{D_M} \qquad [6.2]$$

In this equation the critical particle diameter is represented by d_p, the chromatographic capacity factor is k', the average film thickness of the stationary phase is d_f, the diffusion coefficients for the solute in the stationary and mobile phases are D_s and D_m, and independent factors that are specific to the quality of the column packing include q, λ, γ, ω.[12-13]

6.5.1 Modified Van Deemter Equation

The Eddy diffusion term, also known as the multipath effect, is disregarded in our theory because the pillar arrays have uniform morphology.[12] Mass transfer in and out of the porous layer (C_s) is layer thickness dependent.[19] Since our 50 nm thickness is at least an order of magnitude less than porous layer packings that have become popular in HPLC,[29] and the porous pillar arrays of De Malsche and coworkers prepared by an electrochemical anodization process,[19] we expect that our C_s contribution is relatively minor. Moreover, it should be relatively constant as we change morphological parameters while keeping a constant porous layer thickness. Therefore, we estimate plate height based on only the B and Cm terms in the Van Deemter equation as shown below (Equation [6.3]) with typical literature values for γ and ω inserted.[17, 30-31] In traditional packed bed chromatography with laminar flow, the gaps between particles is linked to d_p; smaller values produce smaller gaps and those gaps govern resistance to mass transfer in the mobile phase. In contrast, the deterministically-fabricated pillar arrays used herein have independent control over pillar diameter and inter pillar gaps (G) and thus we replace d_p with G in the equation.

$$H = \frac{2(0.5)D_M}{v} + \frac{0.02G^2v}{D_M} \quad [6.3]$$

In HPLC the first (B) term above is simply compensated by increasing the flow rate (with concomitant higher pressure). This of course increases the second (C_m) term and necessitates a decrease in particle size.

6.5.2 Mobile Phase Flow Profile

Rapid flow is essential for high efficiency in planar (e.g., TLC) separations. Equation 6.4 describes the effects of parameters on flow in traditional planar chromatography.

$$\mu_f^2 = K_0 t d_p \left(\frac{\gamma'}{\eta}\right) \cos\theta \quad [6.4]$$

In this equation, μ_f is the displacement of the solvent front, d_p is the diameter of the stationary phase particles, γ' represents the surface tension, η the dynamic viscosity and θ, is the contact angle of the mobile phase. A dilemma arises in that small particles needed to improve Cm will exacerbate the B term as flow rate decreases. However, for pillar array platforms the permeability constant (K_0) is considerably larger than for traditional flat beds of packing materials and hence flow is greater.[11,12] Moreover, Equation 6.4 may not be adequate to describe flow in deterministically-fabricated pillar arrays wherein independent and precise control of morphology is possible.

6.5.3 Discussion of Modeled Flow Profiles

To predict the effects of pillar array geometry on flow, hence efficiency, we use the semi-empirical model developed by Mai et al. for ordered arrays of silicon pillars.[24] This predictive flow model is based on the geometrical parameters of the fabricated substrate, experimentally measured solvent-substrate contact angles, and literature values for solvent viscosity and surface tension.[21, 24] The H term is then estimated (Equation 6.3) for these nano-scale arrays using a typical diffusion coefficient of 5.0E-6 cm^2/s in acetonitrile and 1.0E-6 cm^2/s for the more viscous 2-propanol (Figure 6.2).

Equation 6.4 points to a greater flow for larger particles, but it should be noted that this is a consequence of larger inter particle gaps and less flow resistance. The

equation does not reflect the total situation in our pillar arrays or as it pertains to Figure 6.2a where both pillar diameter and gap are controlled independently. The three pillar arrays that started with 1.8 μm pillar diameters and used ALD/PECVD to close the gap follow the order of 1.9D1.1G>2.2D0.8G>2.5D,0.5G with respect to flow rate but predicted to flow fairly similarly (see figure) despite the significant reduction in gap size through the series. It appears that the increase in both surface area and diameter (1.9D1.1G (18.4cm^2), 2.2D0.8G (21.3cm^2), 2.5D0.5G (2.42cm^2), and 1.2D0.8G (26.1cm^2), see Table 6.1), enhances contact wetting, and continuous-nature (smaller gaps to traverse, more open tube-like) as the inter-pillar gaps decrease through the series compensates for the increase in flow resistance. The pillar array that started with ~1 μm diameter, i.e., 1.2D0.8G, is predicted to move significantly slower. This system has a higher surface area than the larger diameter 0.8G counterpart, but is less continuous in nature. It is worth contrasting the arrays with isolated pillars to a packed bed through which flow involves particles with many points of contact. In previous work the arrays were shown to flow significantly faster (higher K_0) than packed beds.[12]

It is the conversion of the predicted flow to a relationship between position of the front on the array and the flow velocity (Figure 6.2c) which is critical in predicting the effects of array morphology and solvent properties on chromatographic efficiency via Equation 6.3. Figure 6.2c demonstrates a predicted rapidly diminishing flow over the first 1 cm of the array which continues at positions greater than 1 cm but at a lower, nearly linear, rate of decrease. These flows are plotted for acetonitrile which has a favorable γ'/η ratio for rapid flow.

6.5.4 Discussion of Band Dispersion with Modeled Systems

The question arises what type of band dispersion dominates the determination of plate height as the solvent front proceeds along the array based on these predications. The situation is grafted in Figure 6.2d. At larger solvent front positions, where axial diffusion is most problematic, the slower 1.2D0.8G system exhibits larger plate heights with the three larger pillar diameter series performing nearly equally (note the linear slopes past 1 cm). Nearer the origin where flow is rapid and resistance to mass transfer

Table 6.1: Calculated surface areas and volumes for the different pillar arrays in μm.

Chip Description		$(V_P) * N_P$	$V=\pi r^2 h$	$V=l*w*h$	$V_C - TV_P$	$(VV/V_C)*100$	$SA=2\pi r*h$	$SA_T=SA*N_p$
Pillar	Gap	Total Pillar Volume (TV_P)	Individual Pillar Volume (V_P) (microns)	Total Chip Volume (V_C)	Void Volume (V_V)	Void Volume (%)	Surface Area/pillar	Surface Area/Chip
1.9	1.1	8.7E+08	45	2.4E+09	1.5E+09	64	96	1.8E+09
2.2	0.8	1.2E+09	61	2.4E+09	1.2E+09	51	110	2.1E+09
2.5	0.5	1.5E+09	79	2.4E+09	8.9E+08	37	130	2.4E+09
1.2	0.8	7.8E+08	18	2.4E+09	1.6E+09	67	60	2.6E+09

may be significant the smallest gap (2.5D0.5G) system produces the lowest plate heights and optima nearest the origin; although there is a significant upturn in all the plots near the origin. Optimum velocities and development distances (point at which B and C_m terms are equal) for each morphology are presented in Table 6.2. In the predicted scenario, decreasing inter pillar gap causes the optimum velocity to increase. The corresponding distance at each optimum velocity then decreases. The main observation with these predictions is that closing the gap is important in reducing plate height because it reduces the C_m term but does not reduce wicking velocities as much as conventional TLC when d_p is decreased. The 2-propanol system (Figure 6.2e,f) moves slower but also has a smaller expected D_M. Section 6.8 provides a treatment for determining the resolution for test cases at positions along the array.

6.6 Performance of 2D-pillar Arrays with Reduced Dimensions

The predictions discussed above fall short of mimicking our experimental arrays in that we have a 50 nm thick PSO layer on the pillar sidewalls, which are fabricated in a triangular arrangement not square as assumed by the predictive flow model. The predictive flow profile also does not consider evaporation. Thus the model is a guide and permits discussion of the effects of morphology on 2-D planar platform separation performance but cannot be expected to exactly represent experimental data. Figure 6.3 is the experimental analog of the modeling shown in Figure 6.2. As expected the largest inter pillar gap scenario shows the most rapid flow of the pillar arrays that began with the same 1.8 μm diameter (1.9D1.1G). The 2.2D0.8G and 2.5D0.5G scenarios have slower flow profiles in that order, which is consistent with the predictive data. However, the experimental data shows a greater difference in flow velocity over this series than that of the predictive flow studies, presumably due to the increased surface area of the PSO layer which is not considered in the model. In addition the flow rates are approximately a factor of two slower than that of the modeled data. The result is that that the up-turn of the H versus position d plots is not observed (Figure 6.3d). The 1.2D 0.8G case, where the pillar diameters started smaller than the other pillar array cases displays behavior that contrast of what the model predicts. The predictions are relevant for all pillar arrays that begin with the same pillar diameter. Again, this may

Table 6.2: Calculated optimum velocities and corresponding development distances for the different pillar arrays.

	Optimum Velocity (cm/s)		Modeled Distance (cm)		Experimental Distance (cm)	
Morphology	ACN	IPA	ACN	IPA	ACN	IPA
1.9D1.1G	0.32	0.064	0.64	0.41	0.35	0.18
2.2D0.8G	0.44	0.088	0.47	0.33	0.19	0.045
2.5D0.5G	0.71	0.14	0.28	0.17	0.047	0.031
1.2D0.8G	0.44	0.088	0.30	0.19	0.35	0.21

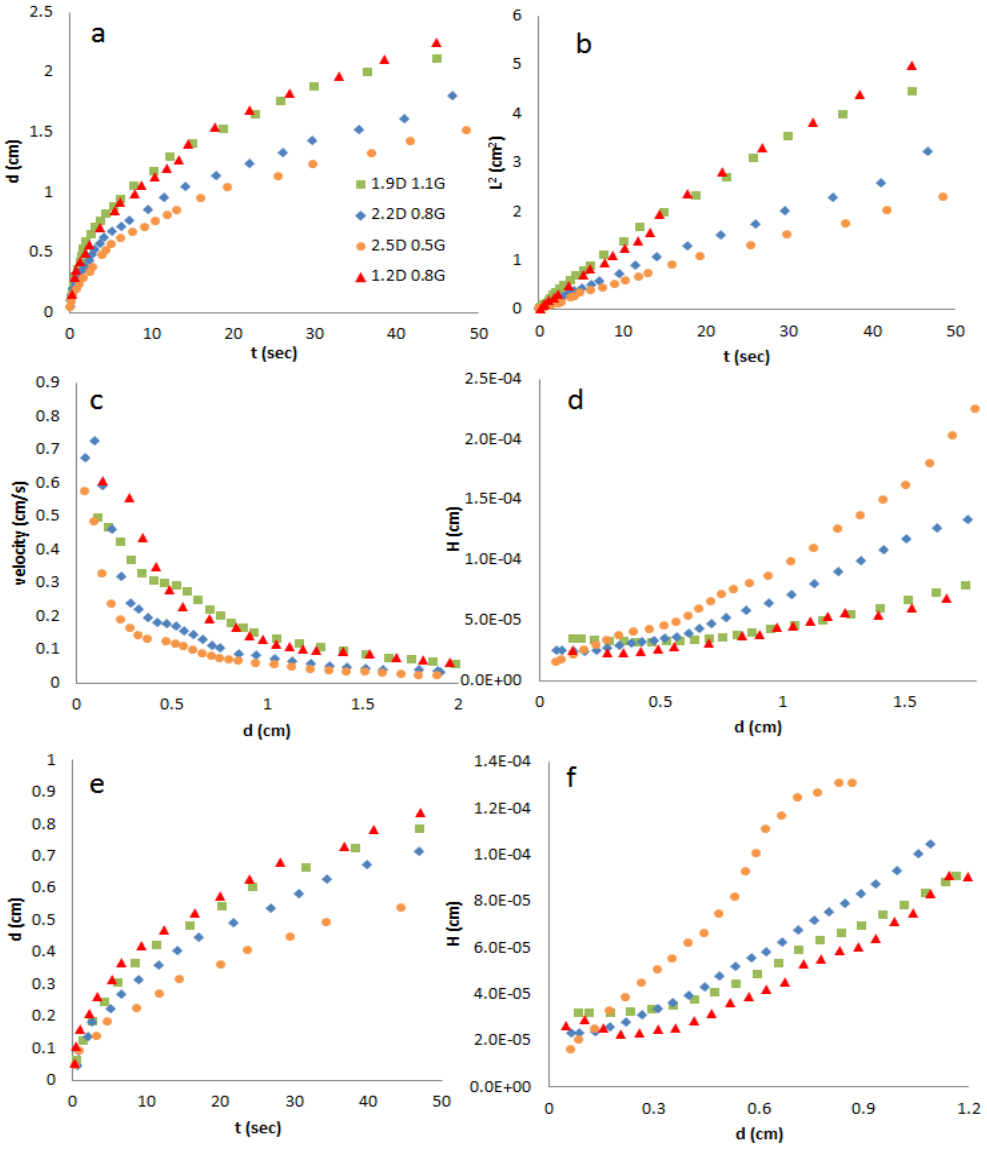

Figure 6.3: Experimental solvent flow of acetonitrile (a)-(d) and 2-propanol (e)-(f); (a) distance versus time of four different inter pillar gap distances; (b) position squared versus time to illustrate linearity; (c) distance versus velocity; (d) efficiency plot to determine optimum gapped scenario; (e) distance versus time and (f) efficiency plot for 2-propanol.

reflect the effect of the PSO layer.

6.7 Separations of 2D-pillar Arrays with Reduced Dimensions

The efficiency treatment in the previous section considers experimental flows coupled with assumptions regarding the parameters in Equation 6.3. We now present actual experimental separations with analytical metrics.

As can be seen in Figure 6.4, the separations that occur at a 2 minute development typically see more inconsistent results likely due to the fast velocity solvent flow being abruptly stopped and the non-automated separation process. The 4 minute development separations experienced less bandwidth variability and exhibited comparable plate height results as the solvent flow rate-based plate height plots shown in Figure 6.3. Plate height values in Figure 6.3d,f show that the 2.5D 0.5G performs the worst, which is consistent with the experimental values seen in Figure 6.4. This large plate height is not a matter of large bandwidth but rather due to the small distance traveled of the mobile phase (see Table 6.3). It is encouraging that the trends in separations-based plate heights seen in Figure 6.4a and especially b (4 minutes) mimics the trends seen in Figure 6.3d,f. However, it should be noted that the plate heights in Figure 6.3 are based on experimental flow rates and Equation 6.3. Conversely, non-van Deemter factors that can influence efficiency and reproducibility such as spot size, spot solvation kinetics, and band drying post separation are operative in the experimental separations-based efficiencies expressed in Figure 6.4.

6.8 Hypothetical Resolution & Calculations

A consequence of reducing velocity as the solvent front moves can be that there are diminishing improvements in resolution as the development proceeds. Resolution calculations are performed using traditional chromatography equations. First considering the van Deemter equation used for these pillar systems and relating it to the variance per unit length (Equation 6.5).

$$H = \frac{B}{v} + C_m \cdot v = \frac{\sigma^2}{L} \qquad [6.5]$$

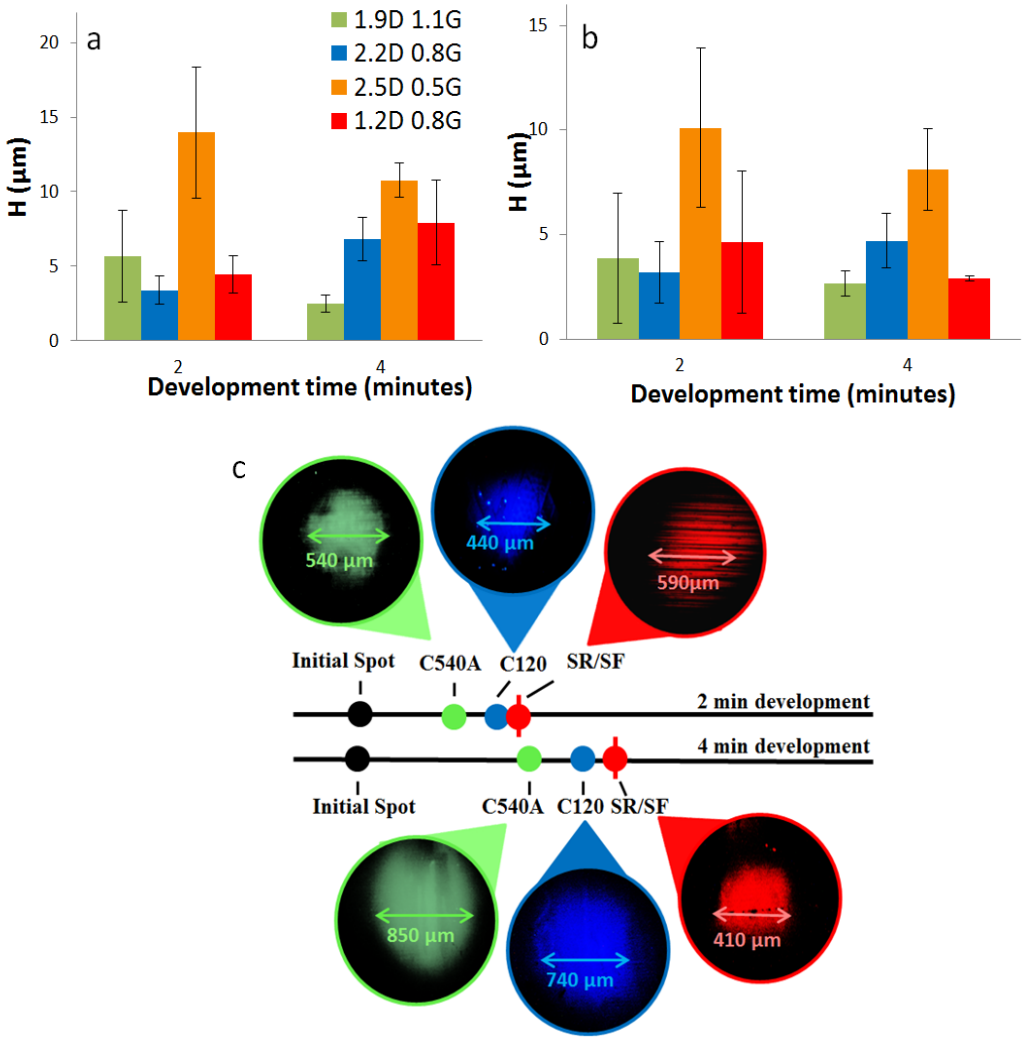

Figure 6.4: Average plate height values for (a) C540A separated bands and (b) C120 separated bands. (c) Example of a 2 minute development verses a 4 minute development on a 2.2D 0.8G chip.

Table 6.3: Average separation values (n=3) at 4 minute development corresponding to Figure 6.4 of manuscript.

Gap Dimensions	Analyte	Band Width (µm)	Plate Height (µm)	Retardation Factor	Solvent Front (mm)
1.9D 1.1G	C540A	580 ± 59	2.5 ± 0.6	0.73 ± 0.04	14 ± 0.4
	C120	700 ± 90	2.7 ± 0.6	0.97 ± 0.001	
2.2D 0.8G	C540A	790 ± 110	6.8 ± 1.5	0.64 ± 0.05	11 ± 0.3
	C120	750 ± 88	4.7 ± 1.3	0.86 ± 0.05	
2.5D 0.5G	C540A	560 ± 17	11 ± 1.2	0.57 ± 0.1	6.2 ± 0.1
	C120	610 ± 56	8.1 ± 2.0	0.85 ± 0.07	
1.2D 0.8G	C540A	940 ± 170	7.9 ± 2.8	0.76 ± 0.08	12 ± 1.1
	C120	650 ± 22	2.9 ± 0.1	0.98 ± 0.006	

Using the modeled velocities (Figure 6.2) and experimental velocities (Figure 6.3) and the treatment in the text for computing plate height, the instantaneous variance (σ^2) over incremental small displacement of the solvent, Δd, can be determined via Eq 6.6. The modeled data corresponds to time increments of 0.01 to 1 second and this translates into distance increments of 0.003 to 0.200 cm depending on the point in the development.

$$\sigma_{inst} = ((\Delta d) \times H)^{1/2} \quad [6.6]$$

In order to determine resolution the sum of instantaneous variances was performed (Equation [6.7]):

$$\sigma_{sum} = (\sigma_{inst1}^2 + \sigma_{inst2}^2 + \cdots)^{1/2} \quad [6.7]$$

Once the σ_{sum} value was found, a couple assumptions are made to compare each individual gapped scenario. We assumed typical retardation factors of 0.9 (R_{f1}) and 0.8 (R_{f2}) for the separation pair. In most of our studies the spot size of analytes are approximately 300 μm. Therefore, the value for σ_{spot} in the resolution equation is 0.0075 cm. The final equation for resolution becomes:

$$Rs = \frac{(R_{f1} - R_{f2}) \times S_f}{4({\sigma_{sum}}^2 + {\sigma_{spot}}^2)^{1/2}} \quad [6.8]$$

The S_f in this equation corresponds to the distance the solvent front traveled. Figure 6.5 provides the calculated Rs with position on the array during the development.

For our modeled systems in the figure, it appears that all the gapped scenarios reach an ideal Rs of 1.5 around 0.50 cm and 0.75 cm of development distance for acetonitrile and 2-propanol, respectively. The poorer performance in terms of Rs for 2-propanol is due to its lower γ'/η ratio, overall slower flow, and hence lower plate height. For each solvent the flows are similar with changing gap size and therefore produce similar Rs versus distance plots.

The most telling observation from the modeled plots is the smaller increases in Rs

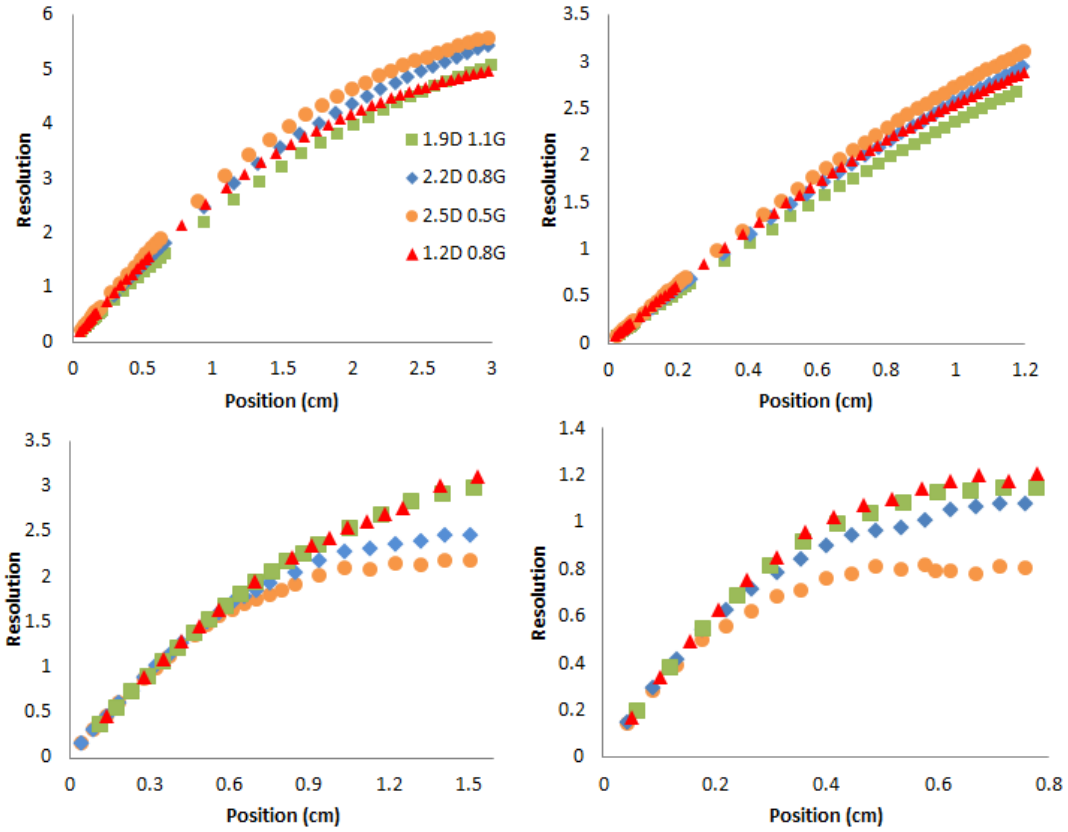

Figure 6.5: Computed Resolution with development distance for modeled (a, acetonitrile & b, 2-propanol) and experimental (c, acetonitrile & d, 2-propanol) flow velocities.

as the solvent front slows later in the development. For example, if the 2.2D 0.8G acetonitrile case is considered the increase in resolution between positions 0.5 cm to 1.0 cm is 104% but from 2.0 to 2.5 it is only 10.2%. In most cases there is little motivation to develop beyond S_f = 2.0 cm. The situation for the experimental data demonstrates the 2.2D 0.8G acetonitrile case as a resolution increase of 62.6% from 0.1 cm to 0.2 cm and an 8.60% increase from 0.6 cm to 0.7 cm. The experimental data concludes that a high vapor pressure mobile phase solvent only needs a development distance of less than 1 cm.

6.9 Conclusion

In summary, predicted flow profiles (Figure 6.2) showed similar results to that of the experimental flow profiles (Figure 6.3) except in the case of the smaller diameter pillars studied herein. The small diameter pillar case was predicted to flow with the slowest velocity but experimentally had a similar flow profile to the largest gap scenario. This variation in results may be attributed to the predicted flow data not correcting for the increased surface area of the porous shell-core pillars or the evaporation rate of the solvents used. Since it is the inter pillar gap that is expected to influence resistance to mass transfer in the mobile phase there was motivation to reduce that gap. Such a change to smaller gaps is also expected to increase viscous drag that we hoped would be compensated by a greater surface area that drives the wicking process. However, the increase in surface area did not adequately compensate, flow rates decreased, and efficiency suffer due to molecular diffusion band dispersion (see both Figures 6.3 and 6.4). The smaller pillar diameter studied had the greatest surface area and performed well in terms of wicking flow rates and efficiency, thereby providing motivation for using fabrication methods that can scale both the pillars and gaps into the nanometer range.[6]

6.10 Acknowledgements

This material is based upon work supported by the National Science Foundation under Grant No. 1144947 with the University of Tennessee, Knoxville. A portion of this

research was conducted at the Center for Nanophase Materials Sciences, which is sponsored at Oak Ridge National Laboratory by the Scientific User Facilities Division, Office of Basic Energy Sciences, U.S. Department of Energy.

6.11 References

1. Desmet, G.; Eeltink, S., *Analytical Chemistry* **2012,** *85* (2), 543-556.
2. Chervet, J. P.; Ursem, M.; Salzmann, J. P., *Analytical Chemistry* **1996,** *68* (9), 1507-1512.
3. Gritti, F.; Guiochon, G., *Journal of Chromatography A* **2012,** *1244* (0), 184.
4. Eeltink, S.; Dolman, S.; Swart, R.; Ursem, M.; Schoenmakers, P. J., *Journal of Chromatography A* **2009,** *1216* (44), 7368-7374.
5. Zhou, F.; Lu, Y.; Ficarro, S. B.; Webber, J. T.; Marto, J. A., *Analytical Chemistry* **2012,** *84* (11), 5133-5139.
6. Fekete, S.; Fekete, J., *Journal of Chromatography A* **2011,** *1218* (31), 5286-5291.
7. Bruns, S.; Grinias, J. P.; Blue, L. E.; Jorgenson, J. W.; Tallarek, U., *Analytical Chemistry* **2012,** *84* (10), 4496-4503.
8. Gritti, F.; Guiochon, G., *LC-GC North America* **2012,** *30*, 586+.
9. DeStefano, J. J.; Langlois, T. J.; Kirkland, J. J., *Journal of Chromatographic Science* **2008,** *46* (3), 254-260.
10. De Malsche, W.; De Bruyne, S.; Op De Beek, J.; Sandra, P.; Gardeniers, H.; Desmet, G.; Lynen, F., *Journal of Chromatography A* **2012,** *1230* (0), 41-47.
11. Taylor, L. C.; Kirchner, T. B.; Lavrik, N. V.; Sepaniak, M. J., *Analyst* **2012,** *137* (4), 1005-1012.
12. Kirchner, T. B.; Hatab, N. A.; Lavrik, N. V.; Sepaniak, M. J., *Analytical Chemistry* **2013,** *85* (24), 11802-11808.
13. Kirchner, T. B.; Strickhouser, R. B.; Hatab, N. A.; Charlton, J. J.; Kravchenko, I. I.; Lavrik, N. V.; Sepaniak, M. J., *Analyst* **2015,** *140* (10), 3347-3351.
14. Gzil, P.; Vervoort, N.; Baron, G. V.; Desmet, G., *Journal of Separation Science* **2004,** *27* (10-11), 887-896.
15. Charlton, J. J.; Jones, N. C.; Wallace, R. A.; Smithwick, R.; Bradshaw, J. A.; Kravchenko, I. I.; Lavrik, N. V.; Sepaniak, M. J., *Analytical Chemistry* **2015,** *87*, 6814-6821.
16. Charlton, J. J.; Lavrik, N. V.; Bradshaw, J. A.; Sepaniak, M. J., *Journal of Applied Materials and Interfaces* **Submitted**.
17. Lavrik, N. V.; Taylor, L. C.; Sepaniak, M. J., *Lab on a Chip* **2010,** *10* (8), 1086-1094.
18. Gustafsson, O.; Mogensen, K. B.; Kutter, J. P., *ELECTROPHORESIS* **2008,** *29* (15), 3145-3152.
19. De Malsche, W.; Clicq, D.; Verdoold, V.; Gzil, P.; Desmet, G.; Gardeniers, H., *Lab on a Chip* **2007,** *7* (12), 1705-1711.
20. Fekete, S.; Fekete, J., *Journal of Chromatography A* **2011,** *1218* (31), 5286-5291.
21. Charlton, J. J.; Lavrik, N.; Bradshaw, J. A.; Sepaniak, M. J., *ACS Applied Materials & Interfaces* **2014,** *6* (20), 17894-17901.
22. Callewaert, M.; De Beeck, J. O.; Maeno, K.; Sukas, S.; Thienpont, H.; Ottevaere, H.; Gardeniers, H.; Desmet, G.; De Malsche, W., *Analyst* **2014,** *139* (3), 618-625.
23. De Malsche, W.; Op De Beeck, J.; De Bruyne, S.; Gardeniers, H.; Desmet, G., *Analytical Chemistry* **2012,** *84* (3), 1214-1219.
24. Mai, T. T.; Lai, C. Q.; Zheng, H.; Balasubramanian, K.; Leong, K. C.; Lee, P. S.; Lee, C.; Choi, W. K., *Langmuir* **2012,** *28* (31), 11465-11471.

25. Wallace, R. A.; Charlton, J. J.; Kirchner, T. B.; Lavrik, N. V.; Datskos, P. G.; Sepaniak, M. J., *Analytical Chemistry* **2014,** *86* (23), 11819-11825.
26. Lindroos, V.; Tilli, M.; Lehto, A.; Motooka, T., Micromachining technologies in MEMS. In *Handbook of Silicon Based MEMS Materials and Technologies*, Second Edition ed.; Elsevier, Ed. 2015.
27. Malsche, W. D.; Gardeniers, H.; Desmet, G., *Analytical Chemistry* **2008,** *80* (14), 5391-5400.
28. Guiochon, G.; Siouffi, A., *Journal of Chromatographic Science* **1978,** *16* (10), 470-481.
29. Tanaka, N.; McCalley, D. V., *Analytical Chemistry* **2015**.
30. Deininger, G., *Chromatographia* **1976,** *9* (6), 251-254.
31. Myers, P., *Chromatographia* **2003,** *57* (11-12), 834-834.

Chapter 7

Chemical Identification by Magneto-Elastic Sensing (ChIMES)

Chapter 7 is an adaption of a research article submitted to Sensors & Actuators B. The article describes the use of a polymer (& polymer composite) coated amorphous ferromagnetic wire that when exposed to gas phase analytes swells the polymer and applies an axial stress on the wire where the magnetic permeability can be monitored.

7.1 Abstract

Described herein is a novel chemical sensing technology, named ChIMES (Chemical Identification through Magneto-Elastic Sensing), that can detect a broad range of targets and that has the rare capability of untethered communication through a metallic or nonmetallic barrier. These features enable many applications in which penetrations into the sampled environment are unwanted or infeasible because of health, safety, or environmental concerns, such as following the decomposition of a dangerous material in a sealed container. The sensing element consists of a target response material hard-coupled to a magneto-elastic wire; when the response material encounters a target, it expands, imposing mechanical stress on the wire and altering its magnetic permeability. The variations in permeability are observed with an excitation-detection coil set that can be removed from the wire by as much as one inch. The sensing element is small and multiple individually-addressable elements can be selectively arrayed to optimize detection for a specific application. The performance of several types of wire and evaluate analytical metrics of single and arrayed ChIMES sensors against a suite of volatile organic compounds is described.

7.2 Introduction

Recent advances in materials science, photonics, and microelectromechanical systems have led to the development of many innovative chemical sensors, with principles of detection based on quartz-crystal microbalances[1], surface acoustic waves[2], microcantilevers[3], flexural plates[4], and various optical absorbance and fluorescence techniques[5]. Nearly all of these sensors, like their predecessors, require a mechanical or an electrical connection between the sensing element and the control and reporting components of the device, making them unsuitable for applications in which penetrations into the sampled environment are unwanted or infeasible because of

health, safety, or environmental concerns. This chapter introduces a new kind of gas sensor that can be queried through both metallic and nonmetallic barriers. The technology, named ChIMES (Chemical Identification by Magneto-Elastic Sensing), relies on detection of stress-induced changes in the magnetic permeability of an amorphous magnetic-elastic wire. The stress is applied by a target response material (TRM) that is hard-coupled to the wire and exhibits an increase in volume in the presence of a target. To our knowledge, this detection mechanism has not previously been reported. Grimes[6,7] et al. have described many variations of a magneto-elastic sensor in which the principle of detection is based on changes in the resonant frequency of an amorphous ferromagnetic foil. Dimogianopoulos[8] has reviewed patents related to the magneto-elastic property, with emphasis on sensors and energy harvesters.

7.3 Amorphous Wire

The amorphous wire is magnetically soft and is composed of one or more ferromagnetic elements, one or more glass-forming elements, and sometimes small amounts of other elements like Cr, Mn, Al, Cu, and Nb for enhancement of mechanical, magnetic, or anticorrosive properties. Vázquez[9] has described the domain structures and magnetic properties of bare and glass-coated magnetic microwires. Most of the experiments reported here were performed with Co-Fe-Si-B “SENCY” wires of various diameters fabricated by Unitika, Ltd., of Japan. (Unitika does not publicize the full compositions of its products.) According to the manufacturer, these wires have high permeability (~10,000 at 10 kHz), very low coercivity (0.06 Oe), and nearly zero magnetostriction. SENCY wire is manufactured through a spinning technique in which a jet of molten alloy is directed into a cold water layer in a rotating drum[10]; as-cast wire is cold-drawn to make products with smaller diameters. Some early experiments were performed with $Co_{80.9}Fe_{4.4}Nb_{4.5}Si_{8.7}B_{1.5}$ wires obtained from Melt Extraction Technology (MXT) of Montreal, Canada. These wires have diameters in the range 30-40 μm and are manufactured using a rapid-cooling technique, in which an alloy rod with a tapered end is inductively heated and a sharpened wheel is used to extract the melt from the tip[11]. In addition, a few sensors were constructed with high-strength 50-μm-diameter

Co-Fe-Cr-Si-B “BOLFUR” wire, also provided by Unitika, but these devices exhibited poor performance and rapidly were abandoned.

7.4 Target Response Material (TRM)

The TRMs can come from many classes of chemical and biochemical compounds. TRMs with strong affinities for specific targets, like aptamers and antibodies, can be used individually, while TRMs with distributed selectivity, such as chemically diverse polymers and polymer composites, can be formed into multi-sensor arrays. Figure 7.1 displays a photograph of four sensors mounted on a stiff GC fiber. The response of a TRM to a specific target may reflect a broad range of structural, physical, and chemical interactions, including the Keesom, Debye, and London forces; donor and acceptor H-bonds; and orientation, steric, coordination, and ion exchange effects. For an array of sensors, the collection of responses provides a unique signature, and a machine-learning tool can be taught to recognize the pattern corresponding to a specific target. While ChIMES signatures are not based on fundamental molecular properties like the harmonic oscillator strengths measured through FTIR, they are target-distinctive when coupled with appropriate data analysis techniques. An example is given below using principal component analysis (PCA). If the TRMs are modular and interchangeable, the selectivity will be tunable, and a single device will be adaptable to many applications. There is a degree of universality about this design, since, at least conceptually; a sensor can be built for any target for which a suitable TRM can be found.

7.5 Instrumentation and Electronics

ChIMES sensors are interrogated by a LabVIEW-controlled electronics package, shown schematically in Figure 7.2 along with the gas sampling system. Exposures to target are done in a cylindrical Pyrex flow tube mounted within a concentric excitation-detection coil set. During an experiment, a drive coil imposes an alternating magnetic field on the wire to switch its ferromagnetic domains, and an adjacent detection coil picks up the Faraday voltage created by the variations in magnetic flux. A “cancellation coil,” reverse-wired in series with the detection coil, nullifies the strong drive field within the detection coil. In addition, if multiple wire-TRM assemblies are present in the flow

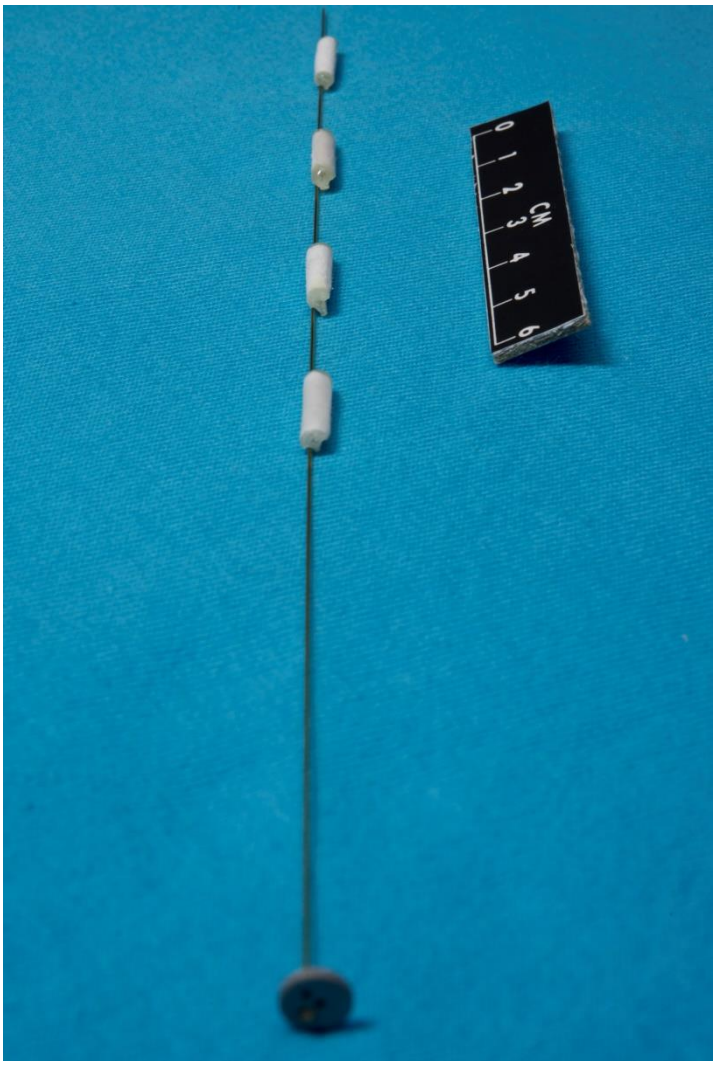

Figure 7.1: Array of four ChIMES sensors mounted on a stiff GC fiber.

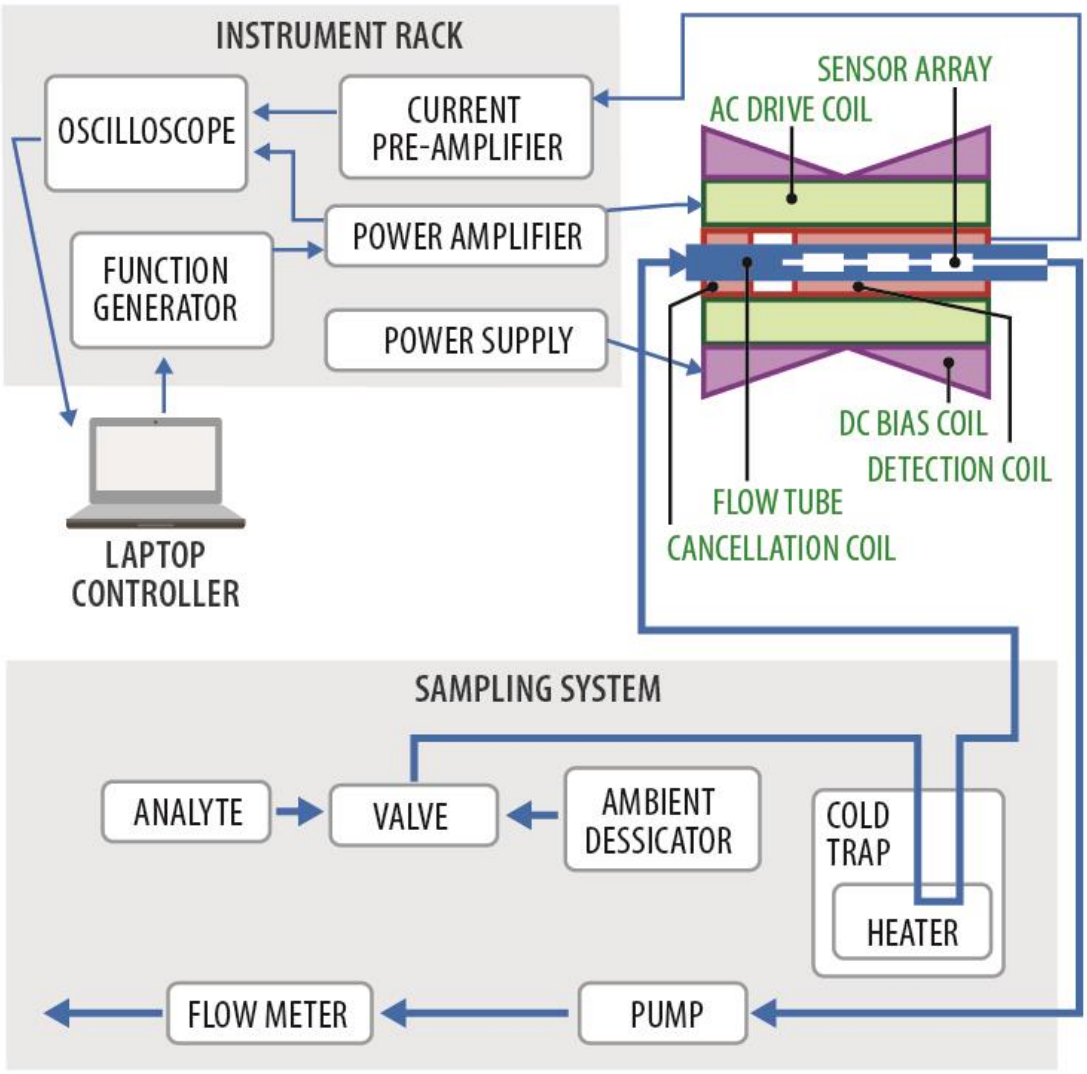

Figure 7.2: ChIMES instrumentation package and gas sampling system.

tube, a direct-current bias coil compensates for the tendency of all wires to switch at the same time and appear as a single sensor. The bias coil provides an additional magnetic field, with magnitude linearly proportional to distance along the flow tube, which causes the switching time of each sensor to depend upon its location in the array. Figure 7.3A shows the magnetic switching signals obtained from a linear array of four sensors. There is one positive and one negative pulse for each wire, corresponding to the oscillations of the magnetic domains as they follow the excitation field. The average of the absolute values of the heights of the positive and negative switching signals of a sensor will be referred to as the response of the device; changes in the response result from stress-induced changes in the magnetic permeability of the sensor's wire. There are no physical or electrical connections to any of the units in an array. The coil set can be removed from the wire by as much as one inch to communicate with a sensor through the wall of a container.

7.6 Fabrication of the Sensor

As the sensor was being developed, several ways to couple the magneto-elastic wire to the TRM were investigated. Of these, the method that gave the best results comprised threading the wire through a channel drilled through the long axis of a TRM cylinder, pre-stressing it to a small amount, and then attaching it at both ends of the cylinder with epoxy. The step-by-step procedure follows:

1. Fabricate a TRM disk using a 12-ton Carver bench-top laboratory press;

2. Using a Dremel® tool, cut a TRM mini-rod measuring slightly larger than 13 mm in length from the disk;

3. Drill a central 0.5 mm channel axially through the mini-rod;

4. With the bit in the hole, grind off excess material with the Dremel® tool to reduce the diameter and length of the mini-rod to 4 and 13 mm, respectively;

5. Laterally drill multiple 0.5-mm-diameter holes into the mini-rod to enhance permeation of analyte;

6. Thread a magneto-elastic wire through the channel and attach one end with epoxy;

7. After the epoxy dries, load the other end of the wire with 1 gram-force for 30-micron wire and 5 gram-force for 100-micron wire;

8. Epoxy the second end of the wire in place and cut off excess wire;

9. Mill a groove along one of the long sides of the mini-rod; and

10. Epoxy a stiff GC fiber into the groove using a minimum amount of adhesive.

7.7 Mechanism of Sensing

When the TRM is exposed to a target, it expands and imposes an axial stress upon the wire. Figure 7.3B illustrates the effect of axial load on the B-H curve of a 16-mm length of 100-µm-diameter SENCY wire, and Figure 7.3C presents conceptual drawings of a TRM in the absence and presence of analyte. The diffusion of analyte into the TRM is influenced by many factors, including the concentration, size, shape, and chemical functionality of the analyte; the morphology and surface energy of the TRM; and the solubility limit of the analyte in the TRM. Similarly, the extent of expansion is governed by a complex set of volumetric, electrostatic, and steric forces.

7.8 Calibration Experimental

In the next section, calibration curves for eight volatile organic compounds (VOCs) are presented. The analytes include methanol (MeOH), ethanol (EtOH), tetrahydrofuran (THF), acetone (ACON), toluene, hexane, trichloroethylene (TCE), and acetonitrile (ACN). For each VOC, the headspace concentration was established by transferring 20 mL of the liquid to a 500 mL HPLC bottle, purging the capped bottle with dried air for 15 minutes, and then allowing equilibrium to develop for 15 minutes. To create a 50% dilution, 300 mL of the headspace gas along with an equal volume of dried air were injected into an SKC gas sampling bag. Three hundred milliliters of this mixture then were used to prepare a 25% dilution in a new bag in the same manner, and so on. The dried air was obtained by forcing compressed room air through an inline desiccator containing Drierite. (For a fielded sensor, several standard drying methods can be used,

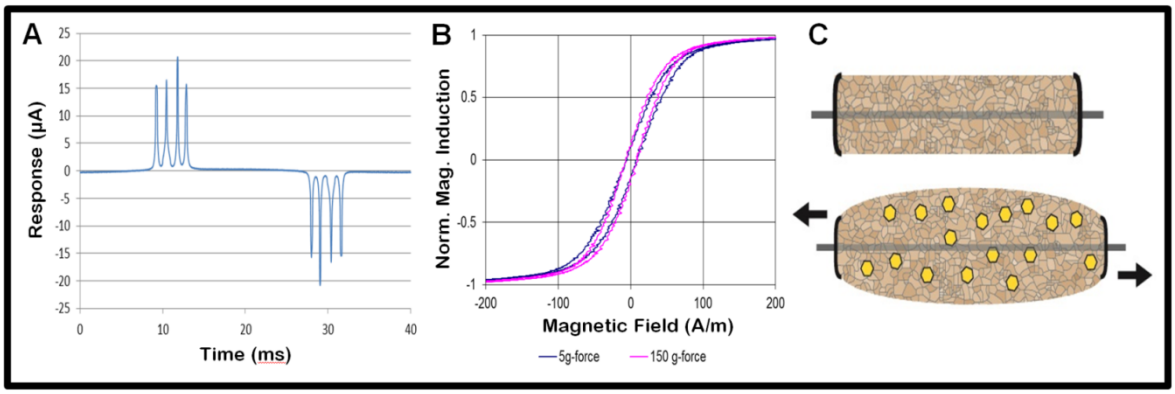

Figure 7.3: (*A*) Magnetic domain switching signals from a 4-sensor array. (*B*) B-H curve for a 100-µm-diameter SENCY wire showing the effect of axial loading on permeability. (*C*) Exposure to analyte causes the TRM in a sensor to swell, imposing axial stress on the amorphous magneto-elastic wire.

but selective removal of water from a sample may be difficult.) Separate syringe needles were used to make the transfers of analyte and dried air.

For the calibration experiments, the gas sampling system of the test bed was reconfigured to accommodate two programmable single-syringe pumps (New Era Pump Systems, Inc.; model NE-1000), one for analyte and the other for dried air. The standard disposable syringes for these pumps are manufactured from laboratory-grade polypropylene and polyethylene, and were suitable for all VOCs except trichloro-ethylene; for TCE, it was necessary to use glass syringes to avoid reaction. The pump controllers were set to equal flow rates of 300 mL h-1. For each concentration, dried air was streamed through the flow cell for fifteen minutes to establish a baseline, and then the analyte and dried air were alternated at fifteen-minute intervals. In most cases, the TRMs required an initial “conditioning” exposure before they would provide reproducible responses. After the experiments at each concentration were concluded, the analyte syringe was rinsed with dried air and the next dilution of analyte.

7.9 Axial Stress Measurements

Figure 7.4 illustrates four aspects of the performance of the sensor. Beginning with the characteristics of the amorphous magneto-elastic wire, Figure 7.4A presents the results of experiments in which the responses of four types of bare wire were measured under known axial stresses (5, 10, 20, 30, 40, 50, and 100 gram-force). The wires were tested as received, except for having lengths of monofilament glued to both ends. During testing, one of the monofilament strands was fixed so as to locate the wire at the proper measurement position inside the (horizontal) flow tube, and the other was attached to a roller and calibrated-mass system that applied the stress along the axis of the wire. Of the four varieties of wire, the 100-µm SENCY brand displays the least noise and the most linear relationship between response and stress, although its sensitivity to small amounts of stress is relatively low. In contrast, the 50-µm BOLFUR wire exhibits the largest responses to small loadings, but its response curve rapidly levels at stresses above 10 gram-force. The 30-µm MXT wire displays a linear response curve for small loadings (≤ 20 gram-force) and relatively low noise; in addition, its responses have the

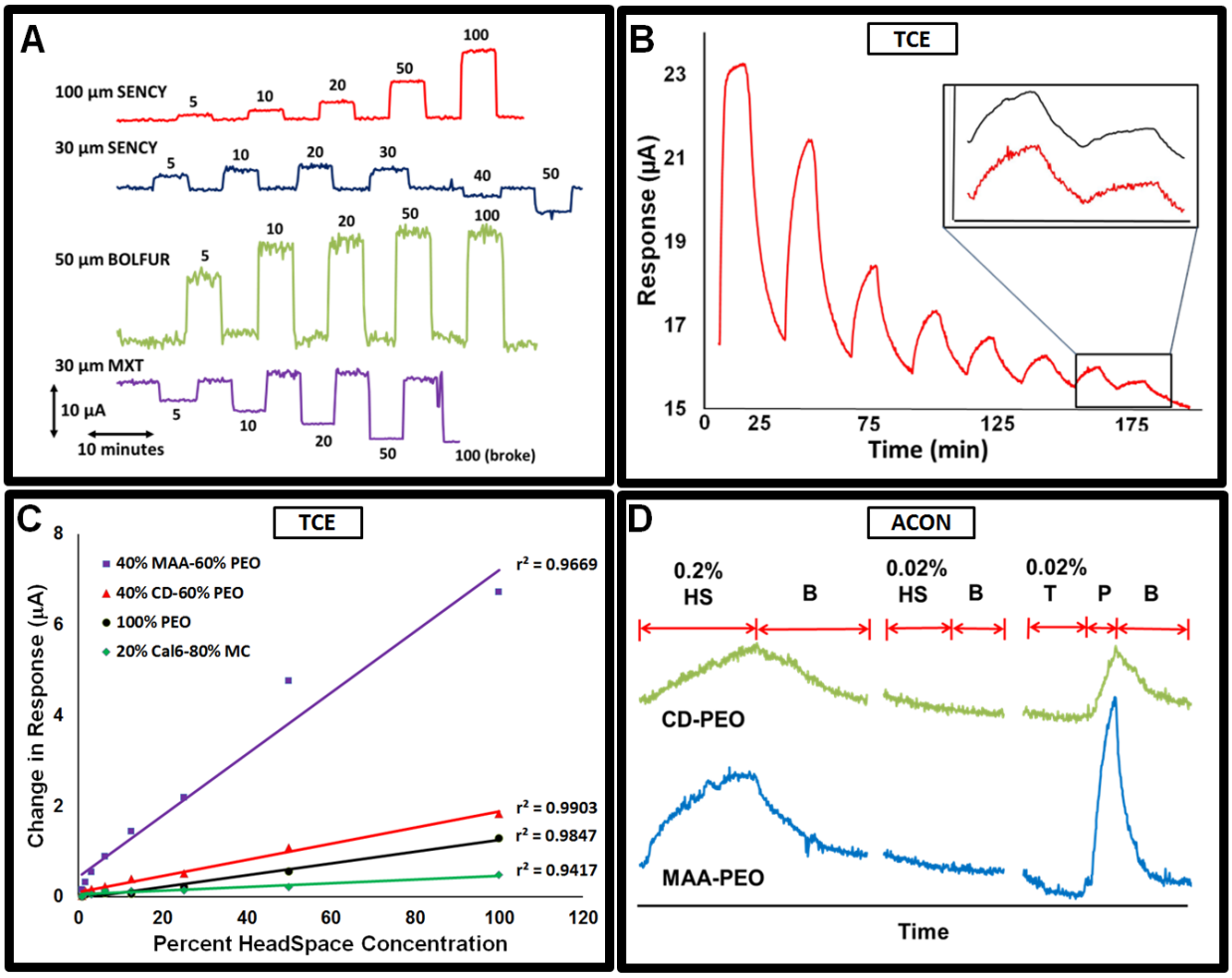

Figure 7.4: (*A*) Responses of four types of magneto-elastic wire to various axial stresses. (*B*) Responses of a single sensor to various concentrations of TCE vapor. The sensor was built from 100-µm SENCY wire and a 40% MAA-60% PEO TRM. Insert: Responses to 0.78 and 0.39% headspace TCE before and after smoothing. (*C*) TCE calibration curves for a four-sensor array. (*D*) Use of the inline cold trap can significantly improve the LOD for acetone (HS = head space, B = blank, T = trap, P = purge).

opposite polarity from those of the 100-µm SENCY and 50-µm BOLFUR wires. The 30-µm SENCY wire is the least usable of the group, since its response curve inverts at axial stresses above 20 gram-force. (Repeated tests with the same wire indicated that the inversion is reversible.)

7.10 Results of Calibration Experiments

The remaining parts of Figure 7.4 present the responses of ChIMES sensors to trichloroethylene and acetone. The sensors were constructed from 100-µm SENCY wire and from TRMs fabricated from the following materials, either neat or as composites: methyl cellulose (MC), 4-tert-butylcalix[6]arene (Cal[6]), poly(ethylene oxide) (PEO), heptakis(6-O-tert-butyldimethylsilyl-2,3-di-O-acetyl)-β-cyclodextrin (CD), and poly(methacrylic acid) (MAA). The composites were needed because some of the response materials could not be pressed into sturdy mini-rods in their pure forms. All materials were obtained from Sigma-Aldrich, with purities of at least 99.5%.

Figure 7.4B displays the responses of a sensor with a 40% MAA–60% PEO TRM to mixtures of TCE and dried air containing from 100 to 0.39% of TCE's room-temperature headspace (HS) concentration. The concentration of analyte was halved from one exposure to the next. The first response, corresponding to the HS concentration, is clipped, which probably reflects off-axis expansion of the TRM, elastic deformation of the epoxy, or nonlinear partitioning of the analyte into the TRM. Additional calibrated-load experiments demonstrated that the clipping did not indicate extension of the wire beyond its elastic limit, and no irreversible changes to the sensor were observed. The shortest response times are less than a minute, while the recovery times are somewhat longer. Recovery could be accelerated by operating at elevated temperatures.

Figure 7.4C displays TCE calibration curves for a four-sensor array containing the following TRMs: 40% MAA–60% PEO, 40% CD–60% PEO, 20% Cal[6]–80% MC, and PEO. The different slopes of the curves represent different sensitivities of the sensors to TCE, with the MAA-PEO sensor exhibiting the greatest sensitivity. Overall, the curves display excellent linearity - the minimum correlation coefficient (r^2) is 0.9417, for the

Cal[6]–MC sensor. By simple extrapolation of the response of the lowest tested concentration to the equivalent of two times the standard deviation of the baseline noise, the apparent limit of detection (LOD) is 0.156 HS concentration or 152 ppm. When evaluated in this manner, ChIMES sensors typically give reproducible results for at least six months.

7.11 Cold Trap Experiment and Results

The schematic of the gas delivery system includes an inline cold trap (Fig. 7.2). Use of the trap is optional (the results presented so far were obtained without it), but it can significantly improve the LOD. Figure 7.4D presents the results of three attempts to detect low concentrations of acetone vapor in dried air with MAA-PEO and CD-PEO sensors. The first two sets of plots in the figure demonstrate that the sensors can detect 0.2% of the headspace concentration of acetone without trapping, but not 0.02%. However, both sensors respond when the more dilute mixture is trapped for 20 minutes at -80.0 ^{o}C and then purged at 40 ^{o}C. The response from the MAA-PEO sensor is more than 2.5 times as strong as the response from the CD-PEO sensor. Using the methodology described above, the LOD of the MAA-PEO sensor for acetone (with trapping) is just under 10 ppm.

7.12 Differentiation of Analytes & Principal Component Analysis

Finally, we address identification of a specific target within a mixed sample. Figure 7.5 displays the responses of the four-sensor array to all eight VOCs. For methanol, ethanol, THF, and acetone, data were obtained at multiple concentrations. The figures across the top signify magnifications of the plots. The rising and falling parts of the curves are different for different VOCs, as well as for different concentrations of the same VOC. It might be assumed that representations of both parts of the response for every TRM in an array would be needed to discriminate between different analytes. However, as demonstrated in the principal component (PC') plot in Figure 7.6 (PC' 3 vs. PC' 2), a single set of descending curves - in this case from the MAA-PEO sensor - is sufficient to distinguish all the analytes and their dilutions. These results suggest that

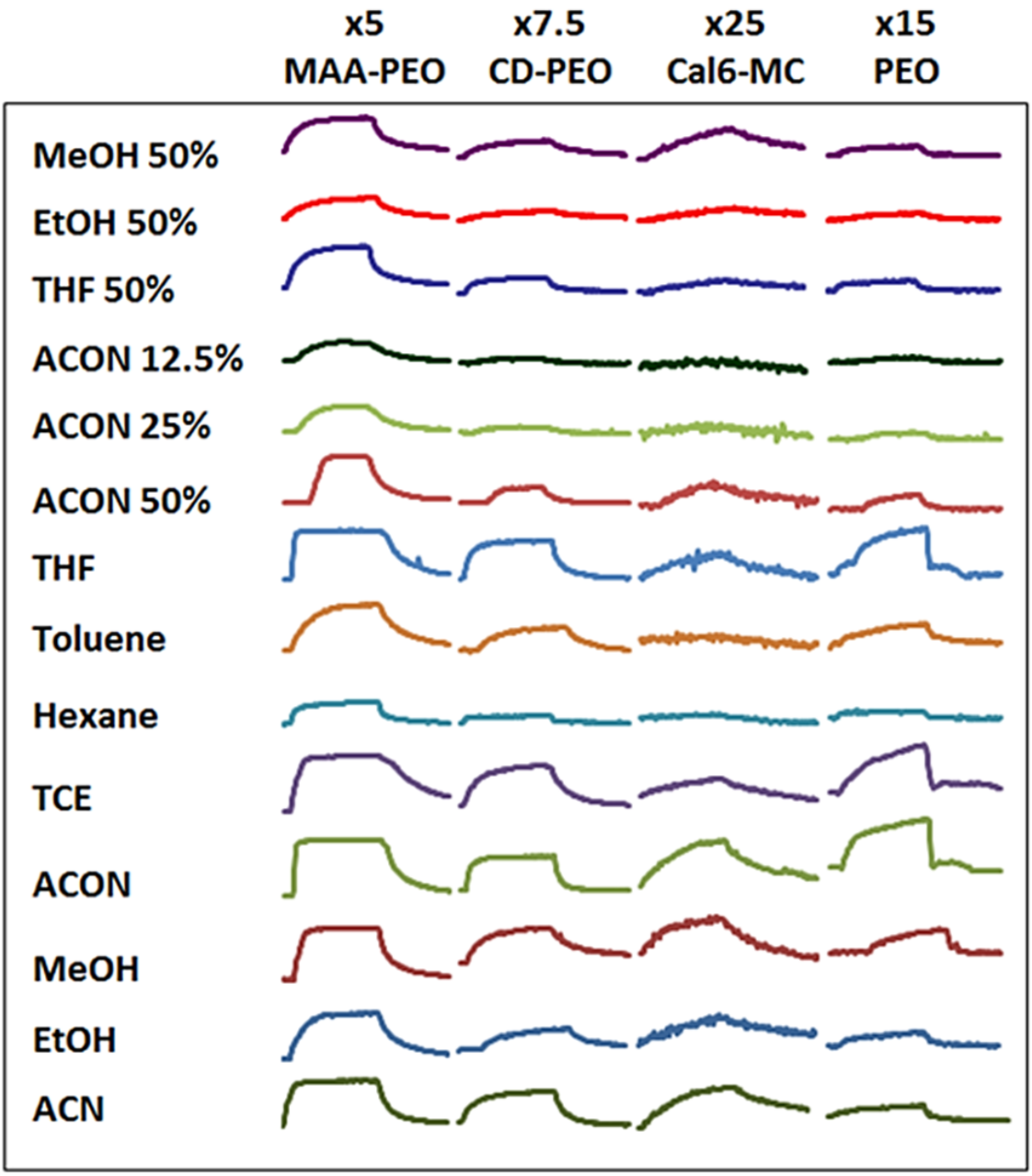

Figure 7.5: Responses of a four-sensor array to a suite of eight VOCs. The sensors were built from 100-µm SENCY wire and TRMs fabricated from 40% MAA-60% PEO, 40% CD-60% PEO, 20% Cal6-80% MC, and 100% PEO.

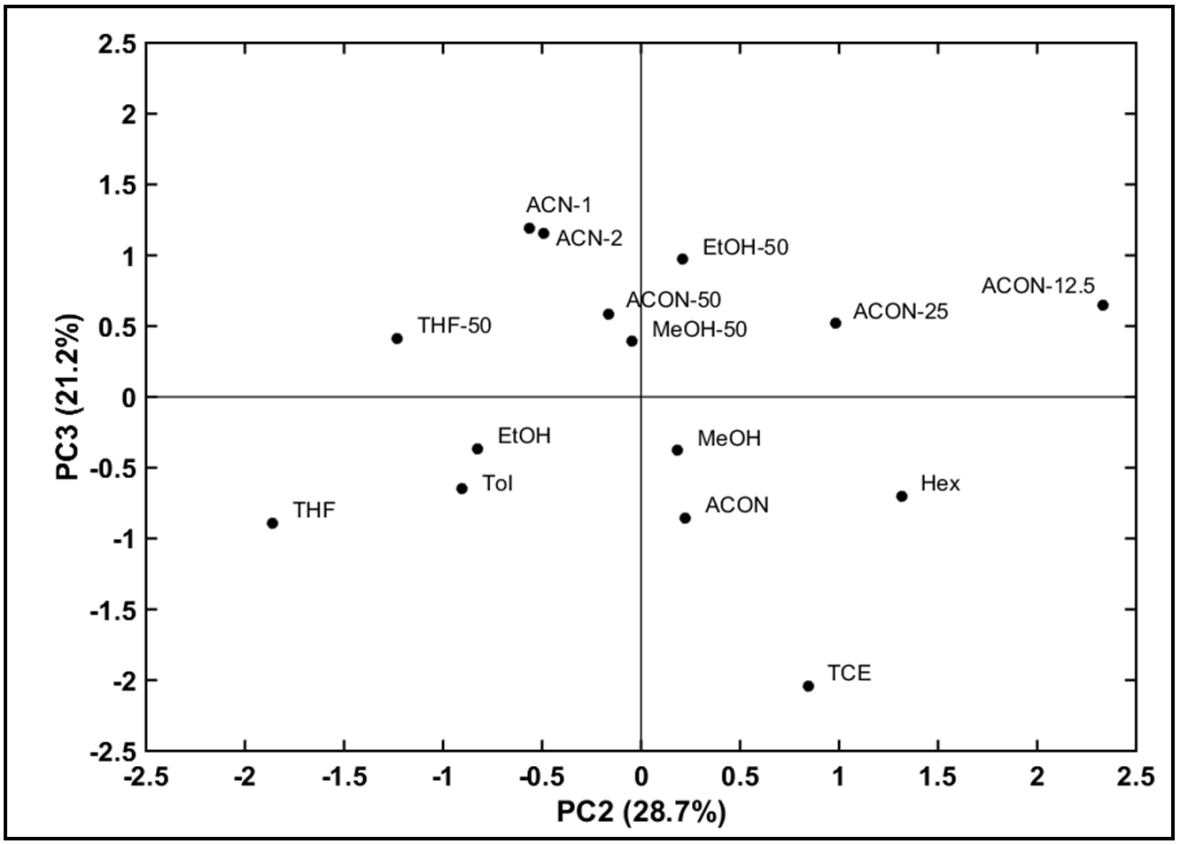

Figure 7.6: Principal component plot for the descending parts of the MAA-PEO responses in Fig. 7.5.

Table 7.1: The principle component values and the % eigenvalue cumulative variance to determine all analytes and their dilutions

Parameter	PC 1	PC 2	PC 3
a_1	-0.5524	0.5091	-0.3197
b_1	-0.7006	0.0923	0.0895
a_2	-0.4190	-0.5671	0.5737
b_2	0.1689	0.6409	0.7488
Eigenvalue	1.8371	1.1469	0.8500
% Cumulative Variance	45.9	28.7	21.2

a ChIMES array has the potential for being highly selective even with a small number of TRMs.

The separation of points in Fig. 7.6 is much more extensive than in plots of PC' 1 vs. PC' 2 or PC' 3 (not shown), indicating that the information permitting discrimination is contained in the minor components. In this analysis, the curves were fit with a sum of two exponential functions: $a_1\exp(b_1t) + a_2\exp(b_2t)$. The PC's are listed in the Table 7.1. The parameter b_1 makes the largest contribution to PC' 1, but very much the smallest contribution to both PC' 2 and PC' 3. In PC' 2, a_2 has the opposite sign from the other parameters, while in PC' 3, a_1 has the opposite sign. PC's 2 and 3 account for 50% of the total variation. Interestingly, the points corresponding to the headspace concentrations of the VOCs differ in both PC' 2 and PC' 3 from those corresponding to their 50% dilutions, while the three points representing the successive dilutions of acetone differ almost entirely in PC' 2. (The plot also includes two nearly-coincident points from a pair of experiments with undiluted ACN.)

7.13 Acknowledgements

This manuscript has been authored by Consolidated Nuclear Security, LLC, (CNS) under Contract No. DE-NA0001942 with the U.S. Department of Energy. The content is solely the responsibility of the authors and does not necessarily represent the official views of the Department of Energy or CNS. Contributors to this manuscript include Nichole A. Crane, Nahla Abu Hatab, Vincent E. Lamberti, David K. Mee, L. Neville Howell, Jr., Larry R. Mooney, Russell L. Hallman, Jr., and Michael J. Sepaniak.

This research was funded by CNS and the University of Tennessee through the Plant- and Joint-Directed Research, Development, and Demonstration programs. The funding sources had no involvement in study design; in the collection, analysis, and interpretation of data; in the writing of the manuscript; and in the decision to submit the article for publication.

The authors are grateful to Unitika, Ltd., for providing several types of amorphous magneto-elastic wire.

7.14 References

(1) X. Li, X. Chen, Y. Yao, N. Li, X. Chen, High-stability quartz crystal microbalance ammonia sensor utilizing graphene oxide isolation layer, Sens. Actuators B 196 (2014) 183-188.

(2) I. Sayago, M.J. Fernández, J.L. Fontecha, M.C. Horrillo, C. Vera, I. Obieta, I. Bustero, New sensitive layers for surface acoustic wave gas sensors based on polymer and carbon nanotube composites, Sens. Actuators B 175 (2012) 67-72.

(3) P.J. Chapman, F. Vogt, P. Dutta, P.G. Datskos, G.L. DeVault, M.J. Sepaniak, Facile hyphenation of gas chromatography and a microcantilever array sensor for enhanced selectivity, Anal. Chem. 79 (2007) 364-370.

(4) B. Cunningham, M. Weinberg, J. Pepper, C. Clapp, R. Bousquet, B. Hugh, R. Kant, C. Daly, E. Hauser, Design, fabrication and vapor characterization of a microfabricated flexural plate resonator sensor and application to integrated sensor arrays, Sens. Actuators B 73 (2001) 112-123.

(5) Z.L. Poole, P. Ohodnicki, R. Chen, Y. Lin, K.P. Chen, Engineering metal oxide nanostructures for the fiber optic sensor platform, Opt. Express 22 (2014) 2665-2673.

(6) C.A. Grimes, S.C. Roy, S. Rani, Q. Cai, Theory, instrumentation and applications of magnetoelastic resonance sensors: A review, Sensors 11 (2011) 2809-2844.

(7) C.A. Grimes, C.S. Mungle, K. Zeng, M.K. Jain, W.R. Dreschel, M. Paulose, K.G. Ong, Wireless magnetoelastic resonance sensors: A critical review, Sensors 2 (2002) 294-313.

(8) D.G. Dimogianopoulos, Sensors and energy harvesters utilizing the magnetoelastic principle: Review of characteristic applications and patents, Recent Pat. Electr. Electron. Eng. 5 **(**2012) 103-119.

(9) M. Vázquez, A. Hernando, A soft magnetic wire for sensor applications, J. Phys. D: Appl. Phys. 29 (1996) 939-949.

(10) Y. Abe, K. Miyazawa, M. Nakamura, T. Ohashi, The behavior of metal jet in the in-rotating-water spinning method, Transactions ISIJ 27 (1987) 929-935.
J. Ström-Olsen, Fine fibres by melt extraction, J. Mater. Sci. Eng. A178 (1994) 239-243.

Chapter 8

Forensic Analyte Detection Capabilities using Novel Analytical Methods

8.1 Current and Novel Forensic Applications

This dissertation provides the advantages and disadvantages of each technique studied as well as describes novel analytical methods in order to aid in the detection of forensic analytes. Each experiment conducted was considered a feasibility study where only compounds with well-defined literature values/spectra were used to determine if the new technique could be deemed analytically useful. Only after the optimization of analytical methods and evaluation of detection metrics were analyzed could further experimentation with forensic analytes be performed. Examples of potential applications with the novel methods described in the preceding chapters are explained below.

Chromatography is an important technique in forensic science since evidence from crime scenes is commonly a mixture of components rather than a pure sample. Currently, the most common form of chromatography used with trace evidence is gas chromatography – mass spectroscopy (GC-MS).[1] GC is a popular method due to its high resolution, low limit of detection, speed, accuracy, and reproducibility. Any compound that is naturally volatile or can be converted to a volatile derivative, thermally stable, and has low molecular weight can be separated using the GC technique. Typically, GC is simpler to use, less expensive instrumentation and is more universal in the analytes it can separate but has some disadvantages when compared to the chromatographic method HPLC. High pressure liquid chromatography is more amendable to polar, non-volatile and thermally labile compounds, such as biochemical, drugs, and metabolites. The power of the mobile phase in HPLC can increase resolution. Some samples in GC require intensive sample preparation in comparison to HPLC.[2]

Current applications using chromatography in forensics are quite vast. Currently, simple thin-layer chromatography has the smallest number of applications within the field. It is an inexpensive method to distinguish between inks, dyes, and drugs. For a specific example, thin-layer chromatography is used in the cases of bank robbers. Typically, when banks bundle paper currency together, they include a security device in some of the packs that when triggered explodes a bright red liquid that is impossible to

wash out. The chemical composition of the red dye used by banks is unique therefore yielding a specific pattern on thin-layer chromatographic platform. HPLC is often utilized in the analysis of materials used to make explosives. When a substance is suspected to have been used in the production of an explosive device, HPLC can be conducted in order to provide qualitative analysis to aid in the identification of the compound. GC and HPLC are more common for drug analysis than any form of planar chromatography. Fire residues (up to 300 different chemicals) and polymers (hairs, fibers, paints, plastics, rubbers) use GC-MS routinely over other forms of chromatography.[1]

The more efficient chromatographic platforms fabricated in Chapter 6 are intended to overcome some inherent pitfalls of the current accepted technology used in forensic analysis. Scaling the pillar diameter and gap of a nano-lithographically fabricated open chromatographic platforms exhibited excellent efficiency and retention with 2-D separation capabilities. The length of the chromatographic platform can be manipulated to create a longer column in order to analyze a more complex mixture of compounds. The advantage that pillar array separation mediums have over GC and HPLC is the portability to onto site testing without expensive equipment. The equipment used for the UTLC pillar arrays is the same as used for simple TLC and only capillary action is required (i.e.no heating or high pressure). Pillar array separations require little to no sample preparation in comparison to GC-MS. Even portable GC-MS instruments run around >$100,000, require re-calibration over time, and contain expensive replacement parts. While the instrumentation to create photolithographic pillar array platforms is expensive, they are also reusable and multiple separation platforms can be created on one wafer to help offset production costs.

After a chromatographic technique is employed to separate components of a forensic mixture, a detection method must be performed to determine the identity of each individual component. As stated before, GC-MS is the most common technique to separate and identify forensic analytes. With mass spectrometry, each analyte is converted into ions in order to be manipulated by extermal electric and magnetic fields. A sample is ionized, ions are sorted and separated according to their mass-to-charge ratio, and the separated ions are then measured and displayed on a plot of m/z ratio

verses relative intensity. In mass spectroscopy, not all analytes are easily ionized, the sample preparation can be tedious (i.e. possible derivatization), and it is a destructive technique. In fact, the most popular techniques in forensic analysis (HPLC-MS, GC-MS, ion mobility spectroscopy, molecularly imprinted polymers, and surface acoustic waves) require the instrument to come into contact with the hazardous sample.[3] On the other hand, this dissertation utilizes Raman spectroscopy as a non-destructive and non-invasive technique to analyze compounds after a chromatographic separation. Recent applications of Raman spectroscopy include the detection of drugs and explosives. For example, RS with near infrared excitation is capable of detecting ecstasy and related phenethylamines in the presence of adulterant and diluents.[4] Spatially offset Raman spectroscopy can be utilized as a non-invasive quantitative technique for the direct determination of active ingredients in pharmaceuticals through plastic bottle packaging.[5] Recently, Raman spectroscopy has been reported for the detection and identification of ultratrace amounts of illicit drug particles and their adulterants on the surface of a human nail.[6] A large number of forensic applications with Raman are available due the spectral libraries becoming more well-defined.

Chapter 5 describes coupling simple TLC with surface enhanced Raman spectroscopy. The hyphenation of TLC-SERS is a simple alternative to GC-MS or other common techniques currently used. Once full optimization occurs of the UTLC pillar array platforms (Chapter 6), testing can be performed on UTLC-SERS to determine applicability to forensic analytes and then compared with GC-MS. Portable Raman instrumentation (~$40,000) is a growing field within the scientific instrumentation industry allowing easy access to on-site testing. Surface enhanced Raman with the blotting technique described herein, is a very simple, low pressure method that can be performed with a portable Raman spectrometer. With SERS, an active metal surface is required in order to yield a large signal enhancement, which can cause an issue with some samples. With the TLC-SERS technique, a separation is transferred onto a SERS active substrate without disturbing the original separation (minimal band broadening). There is potential to create a miniaturized pressure applicator due to the low pressure requirements (6 psi) described in Chapter 5. The Ag-PDMS substrate's size can be tuned and made in bulk before testing is performed on-site. The TLC-SERS technique

developing into the pillar array UTLC-SERS technique could be very useful in forensic trace analysis. Lower concentrations of forensic compounds can be determined with SERS over that of conventional RS.

Individual microelectronic chemical sensors have been explored as a low-cost alternative to laboratory chemical sensing methods since the 1970s. In general, chemical sensors consist of a recognition element that is sensitive to a stimuli produced by various analytes and a transduction element which generates a signal where the magnitude is related to the concentration of the analyte.[7] The chemical sensor used in Chapter 7 was classified as a chemical gas sensor based on the fact that the analytes tested were in the gas phase. Chemical sensors have played a vital role in chemical process, pharmaceutical, food, biomedical, environmental, security, industrial safety, and clinical applications to point out a few. Specifically, chemical gas sensors using nano- and micro-wires have applications including clinical assaying, environmental emission control, explosive detection, agricultural storage and shipping, and workplace hazard monitoring.[8] The end goal of chemical gas sensing is to mimic the sensitivity of a canine's extremely sensitive olfactory system, especially when taking into consideration any forensic application. The current technology continuously faces the obstacle of attempting to make an array of sensors that is both sensitive and chemically selective while maintaining its portability. Nano- and micro-wires are excellent candidates for chemical gas sensing because of the enhanced sensitivity that derives from their very high surface-to-volume ratios.

In Chapter 7, a new sensing mechanism is described. A polymers or polymer composite coats as a target responsive material (TRM) an individual micro-wire where the polymer swells when introduced to a gas analyte. In our experiments, the magnetic permeability of the wire is monitored even with a minute axial stress applied (low concentrations). The potential applications in forensics include explosives, chemical warfare agents, food monitoring, decomposing bodies, air quality, and glucose sensing. The array of sensors used for ChIMES successfully detected down to 10 ppm of TCE with initial studies. Each TRM tested had a unique response to different volatile organic compounds exhibiting the analytical usefulness of the technique. Creating an array of

sensors allows for enhanced selectivity of the technique. More optimization studies using a multitude of polymers should be conducted to target a specific analyte of interest and limit the amount of false positive results. There is potential to detect lower concentrations by tuning the polymer that coats the wire. The studies conducted in this dissertation were the first examples of monitoring using magnetic permeability of a micro-wire. All three methods (Chapters 5-7) developed have excellent potential to be applied to forensic analysis but require more optimization studies to be conducted with specific forensic analytes in mind, as well as, translating these methods into portable instrumentation.

8.2 References

1. Houck, M. M.; Siegel, J. A., *Fundamentals of Forensic Science*. Academic Press: 2006.
2. Miller, J. M., *Chromatography: Concepts and Contrasts*. John Wiley & Sons, Inc.: Hoboken, NJ, 2005.
3. Izake, E. L., *Forensic Science International* **2010,** *202* (1–3), 1-8.
4. Bell, S. E. J.; Burns, D. T.; Dennis, A. C.; Speers, J. S., *Analyst* **2000,** *123* (3), 541-544.
5. Olds, W. J.; Jaatinen, E.; Fredericks, P.; Cletus, B.; Panayiotou, H.; Izake, E. L., *Forensic Science International* **2011,** *212* (1–3), 69-77.
6. Bumbrah, G. S.; Sharma, R. M., *Egyptian Journal of Forensic Sciences*.
7. Korotcenkov, G., *Handbook of Gas Sensor Materials*. Springer: New York, 2013; Vol. 1.
8. Dan, Y.; Evoy, S.; Johnson, C. A. T. Chemical gas sensors based on nanowires. University of Pennsylvania, Philadelphia, PA, 2008.

Chapter 9

Concluding Remarks

All three analytical methods described can be utilized in forensic analysis. Low limits of detection were reached, sensitive techniques were utilized, re-usability was proved, and optimization of all methods was obtained. The ChIMES gas sensor was calibrated for 8 different volatile organic compounds. The target response materials used for the array of sensors were 40% MAA–60% PEO, 40% CD–60% PEO, 20% Cal[6]–80% MC, and PEO. The each sensor responded differentially to the selected volatile organic compound. The slopes of the responses represent different sensitivities of each sensor. TCE had an LOD of 152 ppm and when used with the cold trap experiment the LOD was just under 10 ppm. The coupling of SERS with TLC through conformal blotting allowed for sensitive detection with a chromatographic platform. The Ag-PDMS nanocomposite is a highly efficient SERS substrate for transferring a separation at an optimized 6 PSI and 15 minutes. The limits of detection established for the separation were $1.47*10^{-7}$ M for MGITC, $2.20*10^{-7}$ M for ATP, and $2.74*10^{-6}$ M for Rh6G. Reproducibility of the ATP band for four trials exhibited an RSD of 9.1%. Efficient pillar array chromatographic platforms have proved successful in previous Sepaniak group work. The work described in Chapter 6 decreases the inter-pillar gap and adds an additional porous layer in attempt to create an optimized platform. Plate heights were ≤ 8 μm and bandwidths ranged from 500 to 900 μm. The largest gapped scenario and the smallest diameter scenario behaved similarly giving the optimized (lowest plate height) situation. All techniques described were novel techniques developed to aid not only in forensic analysis, but in any analysis requiring low detection limits and efficient separations.

Vita

Nichole Crane was born in Orlando, FL in November of 1988. At the age of 5 years old she began to train professionally as a ballerina which continued through high school. While in high school she was introduced to chemistry through a teacher Dr. Mehmet Aydeniz, which further fueled her interest in science. Dr. Aydeniz encouraged Nichole to pursue a career in chemistry after working with her for a year at Seminole High School in Sanford, FL. Nichole graduated high school with a 4.3 GPA and pursued a bachelor degree at Florida State University. She graduated Florida State University in August of 2011 with a bachelor of science in Chemical Science and in Criminology. Her goal was to work in the forensic science field. While at FSU she worked on undergraduate research for Dr. William Cooper. The project was named “Bio-Fuel Analysis.” This project required Nichole to analyze algae samples from around the world and from waste water to evaluate the lipid content using techniques such as extraction and UV/VIS spectrophotometry to determine if the samples would be a sufficient alternative fuel. Other undergraduate research included working with a polarized light microscope to study the properties of minerals and crystals under Professor Leroy Odom at the National High Magnetic Field Laboratory in Tallahassee, FL. She then went on to the University of Tennessee to receive her Ph.D. in Analytical Chemistry. She worked under Dr. Michael Sepaniak. With the goal of either working for a forensic or government laboratory Nichole was placed on a variety of projects to allow her an understanding of many analytical techniques. The aim of her studies was to development new methods to detect forensic analytes. Her first project involved surface enhanced Raman spectroscopy being coupled to TLC to yield a chemically specific separation. Her second project involved creating an optimized ultra-thin layer chromatographic platform for higher efficiency separations. The fabricated pillar array project was in collaboration with Oak Ridge National Laboratories at the Center for Nanophase Material Sciences. The last project (in collaboration with Y-12 National Security Complex) involved the fabrication and calibration of a gas sensor using an amorphous ferromagnetic micro-wire. This technology (ChIMES) was awarded two patents and a R&D Magazine Top 100 award for the year 2015. She will graduate in May of 2016 with hopes of gaining a job in the forensics field or a government laboratory in Research & Development.